5-5-2017

On the Cardiac Elastic - 3D Geometrical, Topological, and Micromechanical Properties

Xiaodan Shi

Recommended Citation

Shi, Xiaodan, "On the Cardiac Elastic - 3D Geometrical, Topological, and Micromechanical Properties" (2017). *Theses and Dissertations*. 3365.
https://scholarsjunction.msstate.edu/td/3365

On the cardiac elastin—3D geometrical, topological, and micromechanical properties

By

Xiaodan Shi

A Dissertation
Submitted to the Faculty of
Mississippi State University
in Partial Fulfillment of the Requirements
for the Degree of Doctor of Philosophy
in Biomedical Engineering
in the Department of Agricultural and Biological Engineering

Mississippi State, Mississippi

May 2017

On the cardiac elastin—3D geometrical, topological, and micromechanical properties

By

Xiaodan Shi

Approved:

Jun Liao
(Major Professor)

Song Zhang
(Committee Member)

S. D. Filip To
(Committee Member)

James Ryan Butler
(Committee Member)

Steven H. Elder
(Committee Member/Graduate Coordinator)

Jason M. Keith
Dean
Bagley College of Engineering

Name: Xiaodan Shi

Date of Degree: May 5, 2017

Institution: Mississippi State University

Major Field: Biomedical Engineering

Major Professor: Jun Liao

Title of Study: On the cardiac elastin—3D geometrical, topological, and micromechanical properties

Pages in Study 121

Candidate for Degree of Doctor of Philosophy

In cardiac biomechanics, there is an apparent knowledge gap in 3D cardiac elastin structure and its biomechanical roles. In this study, we fill this knowledge gap via novel biomedical imaging and bioengineering means. In Aim 1, we created an overall mapping of 3D microstructures of the epicardial elastin fibers on porcine left ventricles (LV) using a laser scanning confocal microscope. We demonstrated the location- and depth-dependencies of the epicardial elastin network. Histological staining was also applied to reveal the patterns of endocardial and interstitial elastin fibers, as well as elastin fibers associated with the Purkinje fibers. In Aim 2, a novel algorithm was developed to better reconstruct the elastin fiber network and extract topological fiber metrics. We created a "fiberness" mask via fiber segmentation and fiber skeletonization to obtain the one-voxel-thick centerline skeleton and remove spurious fiber branches, thus generating topological and geometrical descriptors and bringing the study of cardiac elastin to a new level. In Aim 3, we successfully developed a semi-quantitative approach to characterize the residual stress in the epicardial layer by calculating the total angular change due to curling. Our novel curling angle characterization clearly reveals the existence of residual

stress as well as the direction (circumferential vs. longitudinal) and location-dependency of the residual stress. In Aim 4, for the first time we estimated the regional residual stress of the epicardial layer on the intact LV via a four-step methodology: (i) quantify regional residual strains by comparing *in situ* and stress-free marker dimensions; (ii) obtain regional tension-stretch/stress-stretch curves along the circumferential and longitudinal directions; (iii) adjust the biaxial curves to the 0g load reference; (iv) estimate the circumferential and longitudinal residual stresses via residual strains. This method accurately estimates the residual stress in the epicardial layer in various LV anatomical locations. We found that the location-dependency of circumferential and longitudinal residual stresses correlates with the curvature of heart surfaces. Our studies show that the epicardial layer, with its rich elastin content, might function as a balloon that wraps around the heart, and the residual stress sets up a boundary condition that assists with LV contraction.

DEDICATION

This dissertation is dedicated to my beloved family, friends and everyone who has ever supported, encouraged, and advised me during this long journey.

I specifically would like to dedicate this dissertation to my parents, Shengling Xiao and Hong Shi for their never-ending love, support and encouragement. You have always been on my side. Without you, I could never go this far.

ACKNOWLEDGEMENTS

I would like to express my great appreciation to a lot of people for their support, assistance, encouragement towards the success of this dissertation research. I have my deepest appreciation to my major advisor, Dr. Jun Liao. Without his professional guidance, support and encouragement, it would never be possible to accomplish the work and discover my potential. I would like to thank Dr. Song Zhang for his generous help for providing the crucial computational support to the studies in Chapter III. I would like to thank Dr. Steven Elder for his always kind assistance in every question I have faced. I would like to thank Dr. Ryan Butler and Dr. Philip To for their valuable insights for the study and serving on the committee.

I would like to thank all my laboratory members, especially Dr. Bryn Brazile for mentoring me from the beginning of this dissertation research. I would also like to thank Dr. Sourav Patnaik, Katherine Copeland, Sammira Rais-Rohani, Sarah Fitzgerald, Sallie Lin, and Abigail Chandler for their research assistance. I would like to thank all my fellow graduate and undergraduate students for their help during my graduate research and study.

Finally, I would also like to express my appreciation to Dr. Jim Cooley for his very kind support on histological study in Chapter II, and Ms. Amanda Lawrence and Ms. I-Wei Chu for their professional assistances in teaching me laser and electron microscopies.

TABLE OF CONTENTS

CHAPTER

LIST OF TABLES

LIST OF FIGURES

CHAPTER I

INTRODUCTION

1.1 Heart Function and Anatomy

The heart is one of the most important organs in the body. The heart mainly functions as a pump to provide adequate pressure for blood circulation. In healthy hearts, heart valves ensure unidirectional blood flow. By providing oxygen and nutrition to organs and tissues through the body, the heart also assists with metabolite excretion to maintain normal cellular metabolism.

Anatomically, the human heart is a hollow organ consisting of four chambers: the left and right atria (LA and RA) on the top, and the left and right ventricles (LV and RV) on the bottom. Because the left ventricle is responsible for body circulation, it requires more power for pumping than the right ventricle, which is responsible for pulmonary circulation. The difference in pumping power reflects in the thickness of heart walls. Under normal conditions, the wall of left ventricle (9 – 12 mm) is approximately three times thicker than the right ventricle.

The heart wall is consisted of three adjacent layers including the epicardium, myocardium, and endocardium (Figure 1.1 ("Layers of the walls of the heart," 2014)). The epicardium (also known as visceral pericardium) is the outermost thin layer that is largely made of connective tissue with extracellular matrix (ECM). Lying between the epicardium and the myocardium, the subepicardial layer also contains fat tissue, which was reported to accumulate with aging (Kuk, Saunders, Davidson, & Ross, 2009). The richness of collagen and elastic fibers in the epicardium is believed to protect the heart during contraction. The myocardium is the thick middle layer that fuses immediately with the epicardium and forms the main body of the heart wall. Among all three layers, the myocardium contains the relatively less amount of ECM between heart muscle fibers and muscle bundles. The innermost layer of the heart wall is the endocardium that lines the chambers and controls the heart contraction through electrical signals conducted by the Purkinje fibers.

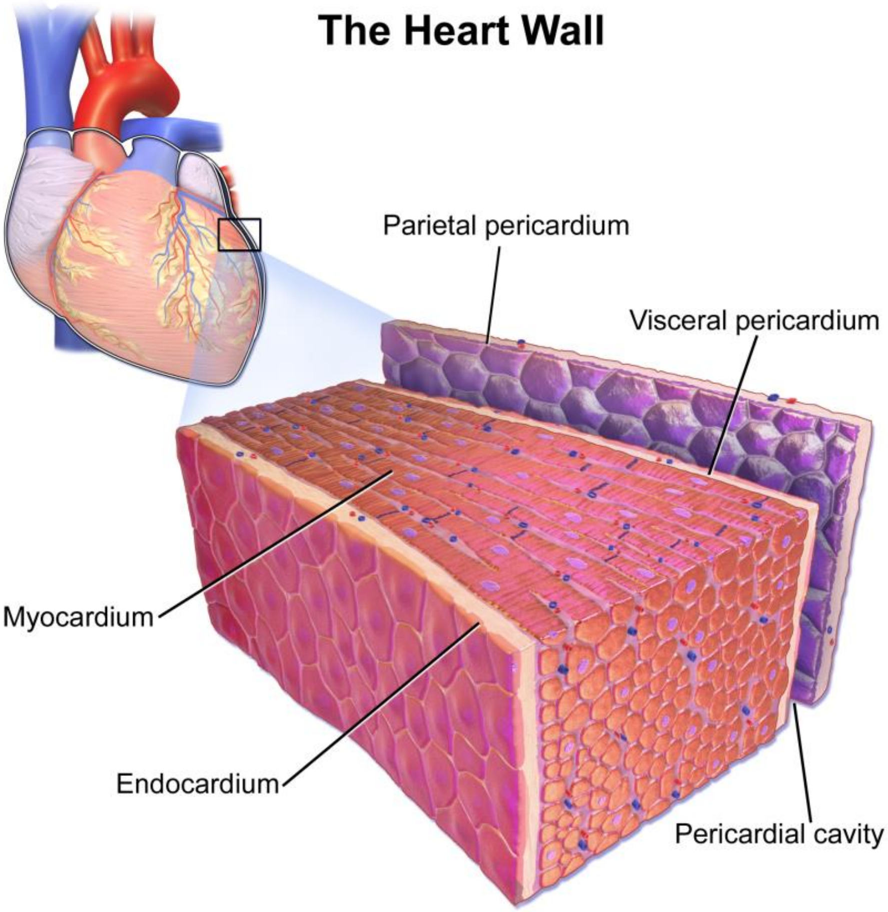

Figure 1.1 Anatomy of layers of ventricular wall showing the epicardium (visceral pericardium), myocardium, and endocardium.

1.2 Global Cardiovascular Disease (CVD) and Treatment

Cardiovascular disease (CVD) has been identified as the leading cause of death globally. In 2012, approximately 17.5 million people died from heart dysfunctions, representing one third of total deaths ("Cardiovascular diseases (CVDs)," 2015). After coronary artery blockage, the downstream cardiomyocytes die and lead to myocardial infarction (MI), commonly known as heart attack (Baroldi, 1965, 1973; Raab, 1963) (Figure 1.2) ("Myocardial Infarction or Heart Attack," 2013). This subsequently results in the expansion of infarcted region, formation of scar tissues, left ventricular wall thinning and dilatation, loss of cardiac function, and eventually fatal heart failure (J. P. Cleutjens, Blankesteijn, Daemen, & Smits, 1999; De Celle et al., 2004; Erhardt, Unge, & Boman, 1976; Gaby; Narula et al., 1996; Reichenbach & Moss, 1975; Robin, 1977; M. D. Silver, Anderson, Vand Dreumel, & Hutson, 1973). During MI, ischemia of the myocardium can extend to the epicardium and endocardium, disrupting the inner lining of the heart. When MI happens, it requires immediate medical treatment to avoid either acute or chronic complications, which may lead to heart failure. The goal of traditional treatments is to save as more heart muscles as possible. To prevent the adverse remodeling of the ventricular wall, current treatments seek fibrinolytic therapies and surgical interventions, such as coronary artery bypass grafting and angioplasty, for a timely revascularization (Gaby; Venugopal et al., 2012); however, those treatments could not effectively replace the necrotic or scarred cardiac tissues (Dowell, Field, & Pasumarthi, 2003; McMahon & Ratliff, 1990; Pasumarthi & Field, 2002).

New MI therapeutic efforts include stem cell injection and grafting of tissue engineered cardiac constructs. However, these new approaches still experience challenges, such as difficulties in achieving cell retention, proper differentiation, mismatched mechanical properties, and efficient vascularization (Grauss et al., 2007; Kannan, Salacinski, Sales, Butler, & Seifalian, 2005; Sharma & Raghubir, 2007; Strauer & Kornowski, 2003). Recently, a novel approach to promote endogenous myocardial repair was performed in a porcine model by applying a bioinductive ECM material to the epicardium. The vasculogenesis in regional infarcted tissue was achieved (Mewhort et al., 2016).

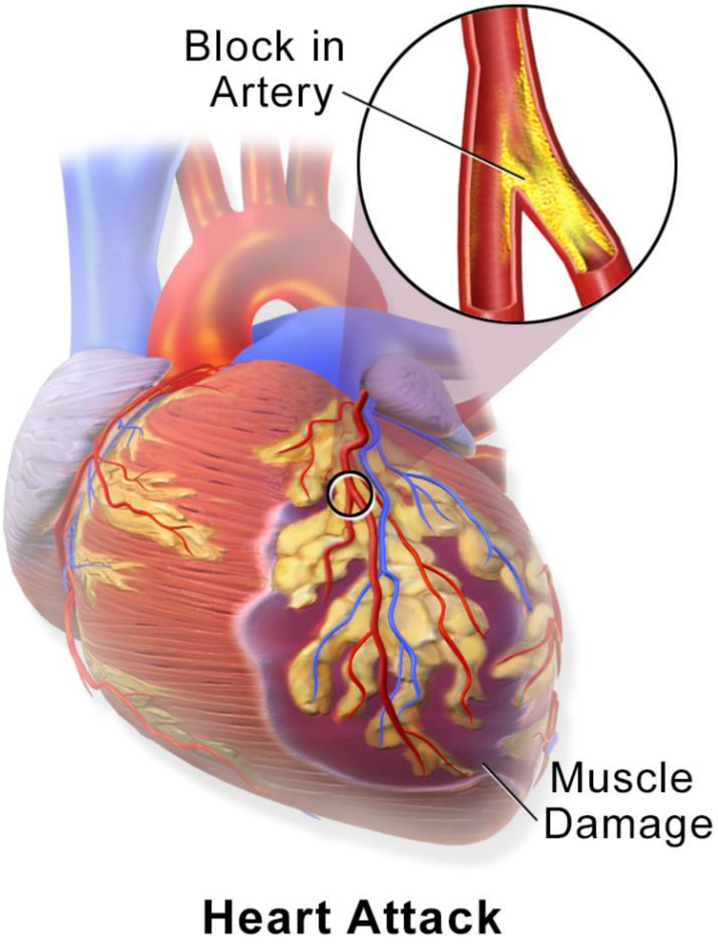

Figure 1.2 Diagram of the blockage in artery and muscle damage during myocardial infarction (MI).

1.3 Structural and Functional Roles of Cardiac Extracellular Matrix (ECM)

To better facilitate the success of new therapeutic efforts which target cardiac tissue regeneration, we need to understand not only the cellular behaviors in cardiac tissues, but also the properties of the cardiac ECM, in both healthy hearts and abnormal conditions after MI. For many years, we have known that cardiac ECM is not an inert structure. From biomechanical perspectives, cardiac ECM is essential in mediating cardiac tissue structures and functions, including structural support for cardiac cells, tethering and force transfer among cardiomyocytes, as well as preventing muscle fiber from excessive stretch (Williams & Black III, 2015). Cardiac ECM also involves in cellular activities, for example to serve as a cellular pathway for signal transmission, migration, differentiation, etc. (Jeffrey W Holmes, Thomas K Borg, & James W Covell, 2005).

Under normal conditions, cardiac ECM provides sufficient mechanical support and intercellular interaction in ventricular walls. When MI occurs, the left ventricular wall undergoes remodeling from the early inflammatory response to the repair phase. This ECM remodeling process involves changes in size, shape, component contents, structure, and function. During the inflammatory response, necrosis of myocytes leads to up-regulation of cytokines and growth factors to recruit cells (platelets, neutrophils, and mononuclear cells) for scar formation (Deten, Volz, Briest, & Zimmer, 2002; Irwin et al., 1999). Moreover, cytokines and growth factors have been reported to interact with cardiac ECM during remodeling (Schönherr & Hausser, 2000). At this early stage, the diseased heart undergoes collagen degradation within the first three hours after infarction (Jack PM Cleutjens, Kandala, Guarda, Guntaka, & Weber, 1995), which leads to ventricular wall thinning and dilatation that causes the increase of diastolic and systolic wall stress (Sutton & Sharpe, 2000).

At the end of necrosis, the formation of new ECM components prepares a scaffold for new collagen deposition. In the following so called fibrotic phase, highly active fibroblasts deposit a large amount of collagen, which results in an increase in stiffness and a distinctive anisotropy in the infarcted tissue. In a pig model, 3 weeks after an MI is produced, the scar is found to be predominantly type I collagen fibers, which are highly aligned in each transmural layer with a pattern similar to that of native myocardium (Holmes, Yamashita, Waldman, & Covell, 1994). During the healing process, the stiffness is found to decrease and be unrelated to collagen content. This period of time is defined as the remodeling phase. The remodeling phase begins at 3 – 4 weeks. In the remodeling phase, the increase in collagen content slows but crosslinks increases, and the infarct is observed to shrink topographically (J. W. Holmes, T. K. Borg, & J. W. Covell, 2005; Jugdutt & Amy, 1986).

Collagen is one of the major ECM structural components of most connective tissues in the human body, i.e., approximately one-third of the entire mass of protein in the human body. Collagen plays an important role in the formation of cardiac tissues and ventricular wall configuration (Fomovsky, Thomopoulos, & Holmes, 2010). Among all three components, collagen has the most abundant amount in the human body with 28 identified types (Sherman, Yang, & Meyers, 2015). Collagen I and III molecules are the most broadly studied types. Type I collagen is a self-assembly rode-like structure with three amino acid chains (α-chains) forming a right-hand helix (Carver, Terracio, & Borg, 1993; Shoulders & Raines, 2009; Theocharis, Skandalis, Gialeli, & Karamanos, 2016)

(Figure 1.3) ("Type I Collagen Molecular Structure," 2016). Rod-like collagen molecules self-assemble covalently into very long rope-like fibrils with 64 – 68 nm D-period via the quarter-stagger model (Chapman & Hulmes, 1984; Y. C. Fung, 1993; Hodge & Petruska, 1963; F. H. Silver, Freeman, & Seehra, 2003). Collagen fibrils are then bridged together by small proteoglycan links to form the collagen fibers, which then build the tissue-specific collagenous ECM environment (Scott, 1991; Weber, Harrison, & Iozzo, 1996).

Collagen I and III make up over 90% of the total collagen content in a human heart. Post MI, more type I collagen is deposited as scar ECM and type III content decreases in the infarcted area (Espira & Czubryt, 2009; Lindsey et al., 2003).

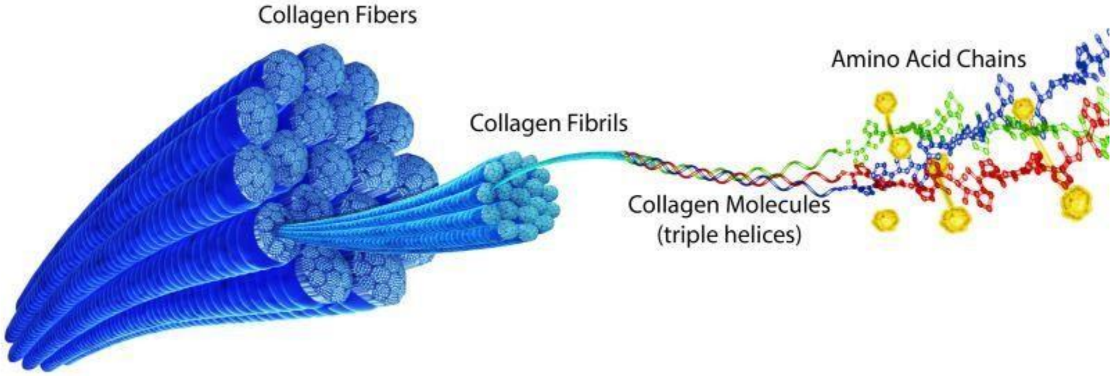

Figure 1.3 Illustration of type I collagen fiber self-assembly.

Hierarchical structure from three amino acid chains (α-chains) to collagen molecules, to collagen fibrils, to collagen fibers.

1.4 Knowledge of Cardiac Collagen and Knowledge Gap on Cardiac Elastin

Previous research has focused on collagen (types I and III) in heart due to its crucial roles in organizing the multilayered helical heart muscle fibers, facilitating force transmission among muscle fibers and across the ventricular walls, and remodeling in response to physiological and pathophysiological alterations (Borg & Caulfield, 1981; Fomovsky et al., 2010; Sussman, McCulloch, & Borg, 2002). Despite a few studies hint that elastin may have an important role in cardiac mechanics and function (Fomovsky et al., 2010; Jöbsis et al., 2007), the biological and mechanical functionality of elastin in the heart are poorly understood when compared to the knowledge of elastin in other soft tissues, such as blood vessels, skin, and ligaments (Fomovsky et al., 2010).

To date, the studies of cardiac elastin have been mainly focused on pathological and physiological aspects (Chowdhury & Reardon, 1999; O'connor et al., 1985; Perou, 1961). For example, the mutation of the elastin gene has been found to cause disorganized and deficient elastic fibers and eventually result in supravalvular aortic stenosis (SVAS) and Williams syndrome (WS) (Chowdhury & Reardon, 1999; O'connor et al., 1985; Perou, 1961). However, recent reports have shed light on the possible biomechanical roles of cardiac elastin on heart functionality (Fomovsky et al., 2010; Li et al., 2012; Mizuno, Mickle, Kiani, & Li, 2005; Mizuno, Yau, Weisel, Kiani, & Li, 2005; Mujumdar & Tyagi, 1999).

It was noted that the overexpression of elastin in an infarcted heart could efficiently help prevent scar expansion, stabilize tissue structure, and delay the ventricular dysfunction (Li et al., 2012; Mizuno, Mickle, et al., 2005; Mizuno, Yau, et al., 2005). Furthermore, a change in the collagen-to-elastin ratio, and not collagen alone, was believed to be correlated with the stiffening of myocardial tissues due to either aging or certain pathological conditions (Fomovsky et al., 2010; Mujumdar & Tyagi, 1999). More research showed that the loss of contractile function in native or diseased myocardium might partially result from the reduction in elastin content of the cardiac tissue (Cheng et al., 2006; Fomovsky et al., 2010; Gupta, Ratcliffe, Fallert, Edmunds, & Bogen, 1994; Henderson et al., 2007; Mizuno, Yau, et al., 2005; Raya et al., 1988; Sato, Ashraf, Millard, Fujiwara, & Schwartz, 1983). The structure-function relationship of cardiac elastin is hence in need of better understanding of its biomechanical roles.

Up to now, the knowledge of the distribution and microstructural arrangement of elastin fibers in the heart tissue remains limited. There are few studies that detail the microstructure and contribution of elastin to the heart and its exact role in overall cardiac mechanics. Among what have been revealed regarding the structural properties of elastin in the heart, vascular elastin in large arteries and arterioles are the regions that have been most thoroughly studied. Vascular elastin was found to contribute significantly to the overall composition and stiffness of vessels in response to blood pressure (G. Baumbach, Walmsley, & Hart, 1988; G. L. Baumbach & Hajdu, 1993). The 3D structure of vascular elastin has been studied using confocal microscopy to show its adventitial population and longitudinally-arranged spatial distribution to exert mechanical stress (Clifford et al., 2011). More recently, the microstructure of fiber-like elastin in pericardial resistance arteries was observed with no prominent external elastic lamina (Bloksgaard et al., 2015).

In previous research of cardiac elastin in the heart (to be specific, we exclude vascular elastin in the heart when we say cardiac elastin), cardiac elastin has been found to be prevalent around the epicardial layer and endocardial layer of both ventricles and atria, and were believed to have no apparent difference in the histological staining patterns of the four chambers (Farquharson & Robins, 1989). A 3D study showed the microstructure of elastin parallel to collagen in the epicardium and a diffused elastin pattern in the endocardium (Jöbsis et al., 2007). In the myocardium, little has been identified without the appearance of vascular system (Farquharson & Robins, 1989). In rat heart studies, individual myocyte was indicated to be surrounded by the elastin network using TEM images as an observation mean (Robinson, Cohen-Gould, & Factor, 1983). A few studies also pointed out that myocytes were grouped into bundles and separated by cleavage layers of perimysium collagen in the LV and other ECM (Pope, Sands, Smaill, & LeGrice, 2008).

All the above mentioned observations point towards a significant role of cardiac elastin in heart function. However, as we just mentioned, the detailed contribution of cardiac elastin in cardiac tissue mechanics is still unclear (Fomovsky et al., 2010). There is an apparent knowledge gap in 3D cardiac elastin structures and its biomechanical roles in mediating cardiac tissue behavior, which hinders a comprehensive understanding of the delicate 3D structure and performance of the cardiac ECM. Hence, we are motivated to fill this knowledge gap with biomedical imaging and bioengineering means.

Aim 1 – Develop an "elastin map" of 3D microstructure of the elastin fiber network on the left ventricle surface in native porcine hearts by using laser scanning confocal microscope (LSCM).

Aim 2 – Reconstruct the 3D network of cardiac elastin fibers and examine both the topology and geometry of this network to obtain the topological metrics such as 3D fiber network, 3D orientation distribution, and numbers of branching points and cliques in the network.

Aim 3 – Demonstrate the existence of residual stress of the epicardial layer in the porcine LV surface via a novel surface curling angle phenomenon and quantification method.

Aim 4 – Quantify the regional residual strain and residual stress of the epicardial layer in the intact porcine left ventricle surface by using marker-tracking technique and a biaxial mechanical testing system.

CHAPTER II

DEVELOP AN “ELASTIN MAP” OF 3D MICROSTRUCTURE OF THE ELASTIN FIBER NETWORK ON THE LEFT VENTRICLE SURFACE IN NATIVE PORCINE HEARTS

2.1 Introduction

Cardiac ECM, as one of the most important components in the heart, has received wide attention for cardiovascular disease (CVD) studies due to its unique structure and function. Among all three major components in the cardiac ECM, the most extensive research has focused on collagen and has left limited focus on elastin. It is roughly known that elastin functions to protect the heart by providing tensile stress through its biomechanical properties and morphology; however, the detailed microstructure in the overall LV is still unknown.

Jöbsis et al. (2007) pioneered the technique using a two-photon excitation microscope to study the microstructure of cardiac elastin in different locations of the epicardium. A possible association in the structure of elastin and collagen was also revealed. In this chapter, we aim to narrow down the knowledge gap by thoroughly delineating and quantifying the elastin fiber network in the LV using porcine heart as a model. We hypothesize that elastin fibers alter its microstructure that span throughout both epicardial and endocardial layers depending on location and depth variations. To characterize the microstructure of the elastin fiber network, laser scanning confocal microscope (LSCM) and image analysis software were used to generate 3D images and deliver the distribution and orientation in the porcine LV. Histological staining was also applied to show a supporting 2D study of how the elastin fiber network associates with collagen and myocyte bundles in the cardiac ECM.

2.2 Materials and Methods

2.2.1 Sample Preparation

Fresh porcine hearts were obtained from a local abattoir and transported to the laboratory. Sample squares (~ 10 mm × 10 mm × 1 mm) that cover the base, middle, and apex regions were dissected from the left ventricle of each heart. For the base region, five locations were examined, with two covering the anterior area, one covering the lateral area, and two covering the posterior area. For the middle region, four locations were examined, with two covering the anterior area, one covering the lateral area, and one covering the posterior area. For the apex region, three locations were examined, with one covering the area adjacent to anterior, one covering the apex tip, and one covering the area adjacent to posterior (Figure 2.1). Note that all samples were marked with a suture tied to the upper right corner to establish orientation.

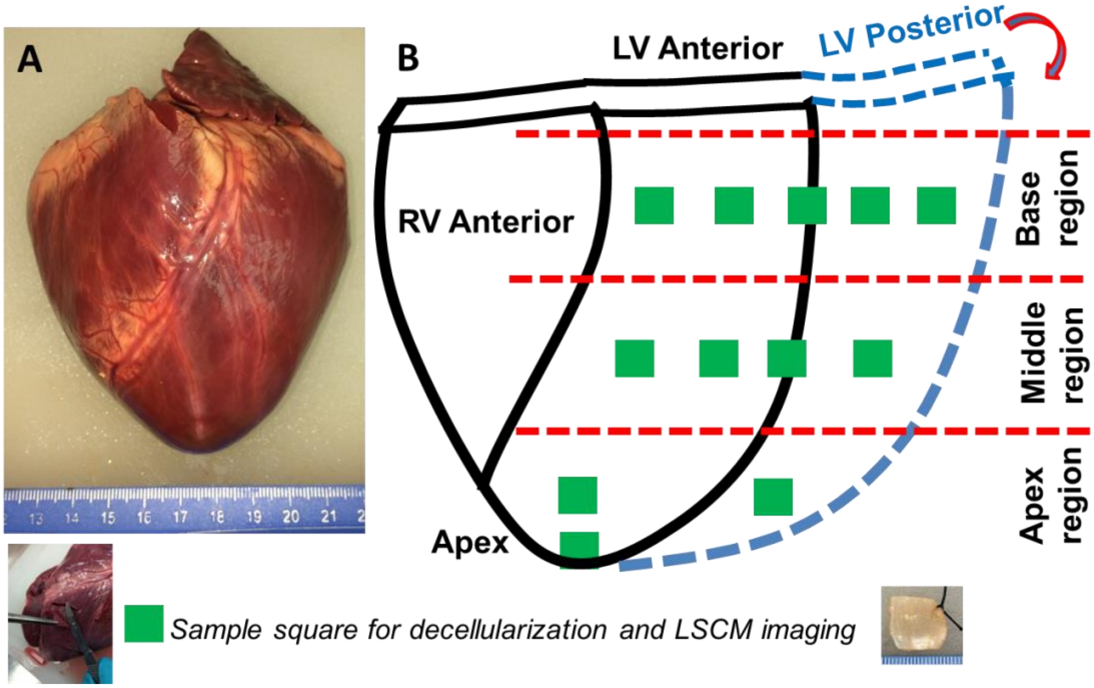

Figure 2.1 Schematic illustration of sample preparation plan.

2.2.2 Laser Scanning Confocal Microscopy and Histology

For laser scanning confocal microscopy (LSCM) sample preparation, an optimized version of our established decellularization method was used for preserving the cardiac ECM microstructure. Before processing the LSCM imaging, sample dimensions (length, width, and thickness) were first recorded before and after decellularization to assess possible dimensional changes. 10 samples were randomly dissected from the epicardium in the LV. For each dimension of one sample, three measurements were taken and the average was recorded. The samples were decellularized in a rotating bioreactor using 1% sodium dodecyl sulfate (SDS) with 0.01% trypsin, 1 mM phenylmethylsulfonylfluoride (protease inhibitor), 1% antibiotics (100 U/ml penicillin and 100 µg/ml streptomycin), 20 µg/ml RNase A and 0.2 mg/ml DNase at room temperature for 1 week. The decellularization solution was changed every two days to avoid contamination and tissue deterioration.

After verification of dimension preservation after decellularization, new fresh native samples underwent the full decellularization procedure mentioned above. After a PBS wash for 24 hours, the samples underwent a gradient glycerol treatment to obtain transparent samples, which enhance the laser light penetration depth. The detailed glycerol treatment steps are as followed: 30 minutes in 25% glycerol, 30 minutes in 50% glycerol, 75% glycerol, and 100% glycerol.

The decellularized and glycerol treated samples were subjected to Laser Scanning Confocal Microscopy (Zeiss Inc., Inverted mode, Axiovert 200 M) to visualize and image the 3D elastin network under CY3 channel (elastin autofluorescence, Ex = 543 nm) with z-stack imaging technique.

Due to the extremely low density of interstitial elastin in the myocardium, 3D LSCM cannot detect the elastin specific signal from the myocardium layer. Moreover, we also noticed that the elastin-specific LSCM signal from the endocardium layer is very diffused and blurred due to the fine and dense endocardial elastin network. We hence focused the 3D mapping on the epicardial elastin.

Starting from the epicardial surface, the 3D z-stack images covered a total tissue thickness of ~ 70 µm at ~ 1 µm interval. All images were acquired with a 12-bit gray scale and a dimension of 1024 × 1024 pixels. ImageJ (NIH, Bethesda, MD) was used to create 3D projections of the first 15 µm section, the last 15 µm section, and the full thickness of each image stack. Elastin fiber orientation and distribution in different layers were quantified using the OrientationJ plugin. For histological assessment, tissue samples were fixed in 10% buffered formalin solution for 72 hours, and sectioned to 5 μm thick. The slices were then stained using Movat's Pentachrome protocol, in which elastin is stained black, collagen stained yellow, and heart muscle stained red.

2.3 Results

2.3.1 Changes of Sample Dimensions Before and After Decellularization

The sample dimensions (length, width, and thickness) measured before and after decellularization were listed in Table 2.1. We calculated dimension reductions of each sample before and after decellularization. Overall average reductions of 10.47% in the circumferential direction, 17.86% in the longitudinal direction, and 20.09% in thickness were observed (Table 2.1). Our data show that the dimension reductions were reasonably small and mainly due to the wash-away of the attached myocardium, and the epicardial layer was maintained relatively well.

Table 2.1 Sample dimensions measured before and after decellularization and percent reductions after decellularization.

Unit: mm	Native Samples			Decellularized Samples			Percentage reduction, %		
	CD	LD	T	CD	LD	T	CD	LD	T
1	20.12	15.54	1.02	17.98	13.33	0.80	11.18%	14.22%	21.41%
2	18.54	14.75	0.88	16.09	11.79	0.70	13.21%	20.07%	20.06%
3	19.63	12.26	0.93	18.40	9.08	0.77	6.26%	25.94%	17.20%
4	15.87	10.27	0.99	14.10	8.31	0.81	11.15%	19.08%	18.18%
5	13.58	7.99	0.86	11.47	6.23	0.68	15.54%	22.03%	20.47%
6	18.00	10.67	0.97	16.63	9.15	0.71	7.61%	14.25%	26.42%
7	14.50	9.49	0.93	12.40	7.82	0.72	14.48%	17.60%	22.16%
8	16.95	14.23	0.96	15.57	11.47	0.84	8.14%	19.40%	12.50%
9	14.92	12.07	1.01	13.93	11.08	0.78	6.64%	8.20%	22.39%
				Overall Average			10.47%	17.86%	20.09%

Note: CD, LD, and T represent the circumferential direction, longitudinal direction, and thickness of each sample, separately.

2.3.2 LSCM Imaging Signal is Elastin Specific

Although the elastin autofluorescence has been widely used in confocal imaging, we conducted an experiment to prove that the LSCM imaging signal in our study was elastin specific (Clifford et al., 2011; Zipfel et al., 2003). As evidence that the signals were of elastin in origin, we compared the LSCM images of the decellularized epicardial layer, myocardial layer (dissected separately), myocardial region with blood vessels (dissected separately), and endocardial layer. We found that the fiber network signals in the epicardial layer (Figure 2.2-A) and endocardial layer (Figure 2.2-D) were abundant and showed a morphology consistent with our histological observation (Figures 2.7 and 2.8). However, in the decellularized myocardial layer, in which the collagen network is dominant, no fiber signal was detected (Figure 2.2-B). In the myocardial region with blood vessel, the fiber signals existed around the blood vessel wall.

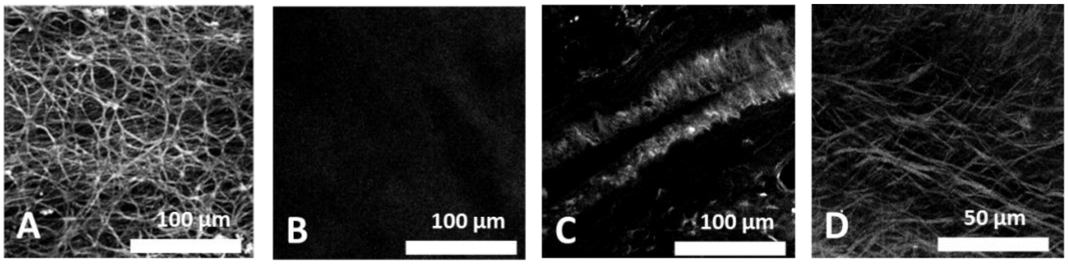

Elastin fiber signals in the decellularized **epicardial layer**

No detectable elastin fiber signals in the decellularized **myocardial layer**

Vasculature elastin fiber signals in the decellularized **myocardial layer**

Elastin fiber signals in the decellularized **endocardial layer**

Figure 2.2 LSCM fiber image signals are elastin specific.

Note: Elastin fiber signals are generated by autofluorescence of elastin under CY3 channel (Ex=543 nm). The collagen dominated decellularized myocardial layer produces no detectable signal of elastin (Panel B).

2.3.3 Mapping of Epicardial Elastin with LSCM

The epicardial elastin fiber network across the left ventricle was mapped in Figure 2.3 using the projection of all slices generated by the LSCM. We noticed that the epicardial elastin fiber network had an overall fiber orientation that is associated with the helical myocardial fiber orientation, which was observed from the base to the apex (Figure 2.3). An inclination in the longitudinal direction was observed from locations B2 and B4. On the lateral side B3, elastin fibers showed a random pattern of a slightly overall up-and-down trend. In the middle panel (where samples were obtained from middle region of the left ventricle), elastin fibers displayed a similar distribution of the up-and-down trend to what was observed in the base region. From the two locations M1 and M2 on the anterior sides, elastin fibers tended to tilt slightly toward the lateral, and then converged to the apex region. In the apex region, a unique spiral helix-like distribution was found (Figure 2.3-A2), whereas on the other two sides of the apex, elastin fibers showed a dominant longitudinal direction.

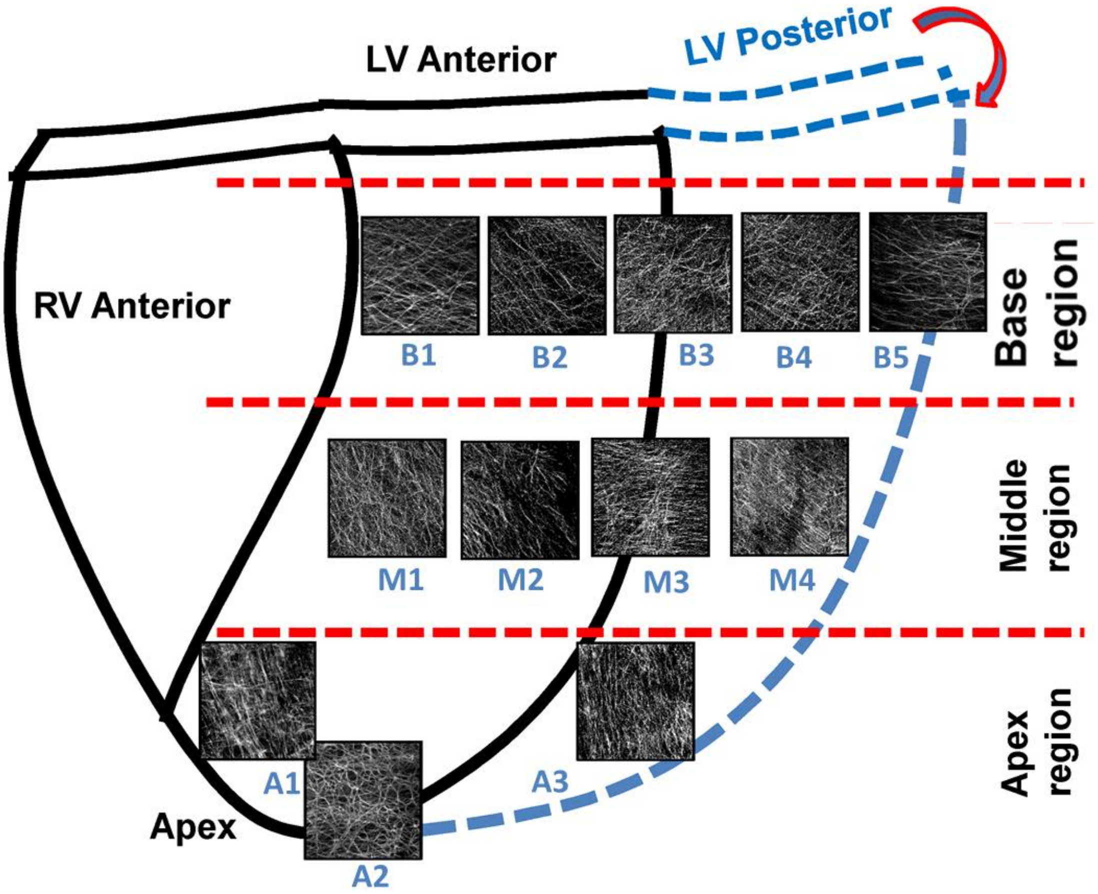

Figure 2.3 The overall distribution of epicardial elastin network in three regions of the left ventricle was obtained from 3D confocal microscopy.

Note: The top and middle panels represent regions of epicardium samples arranged from the anterior to the posterior side. The bottom panel represents the apex region of epicardium samples.

For all three region panels, we further divided stacks of image sequence of each sample into three projections. The first projection was obtained from the surface to the 15 μm deep into the sample (the first 15 μm). The second was then taken from the last 15 μm to the opposite side of the surface (the last 15 μm). The projection of full thickness was also examined. For each projection, we analyzed the distribution and orientation of elastin fiber network from different thicknesses (Figures 2.4 – 2.15). We found that, in locations of Base-1 (Figure 2.4) and Base-4 (Figure 2.7), the first 15 µm layers appeared to have denser elastin fibers with a random alignment, while a more aligned fiber distribution in the last 15 µm layer. In the location of Base-2 (Figure 2.5), elastin fibers were highly aligned along -45° in the first 15 µm, while the last 15 µm, the pattern was less oriented and more random. Elastin fibers on the basal lateral location (Base-3) (Figure 2.6) showed a tendency towards bimodal distribution in all three projections due to the presence of more vertical fibers. In the location of Base-5 (Figure 2.8), a horizontal alignment was found in the first 15 µm; however, in the last 15 µm the elastin fibers had a more random distribution.

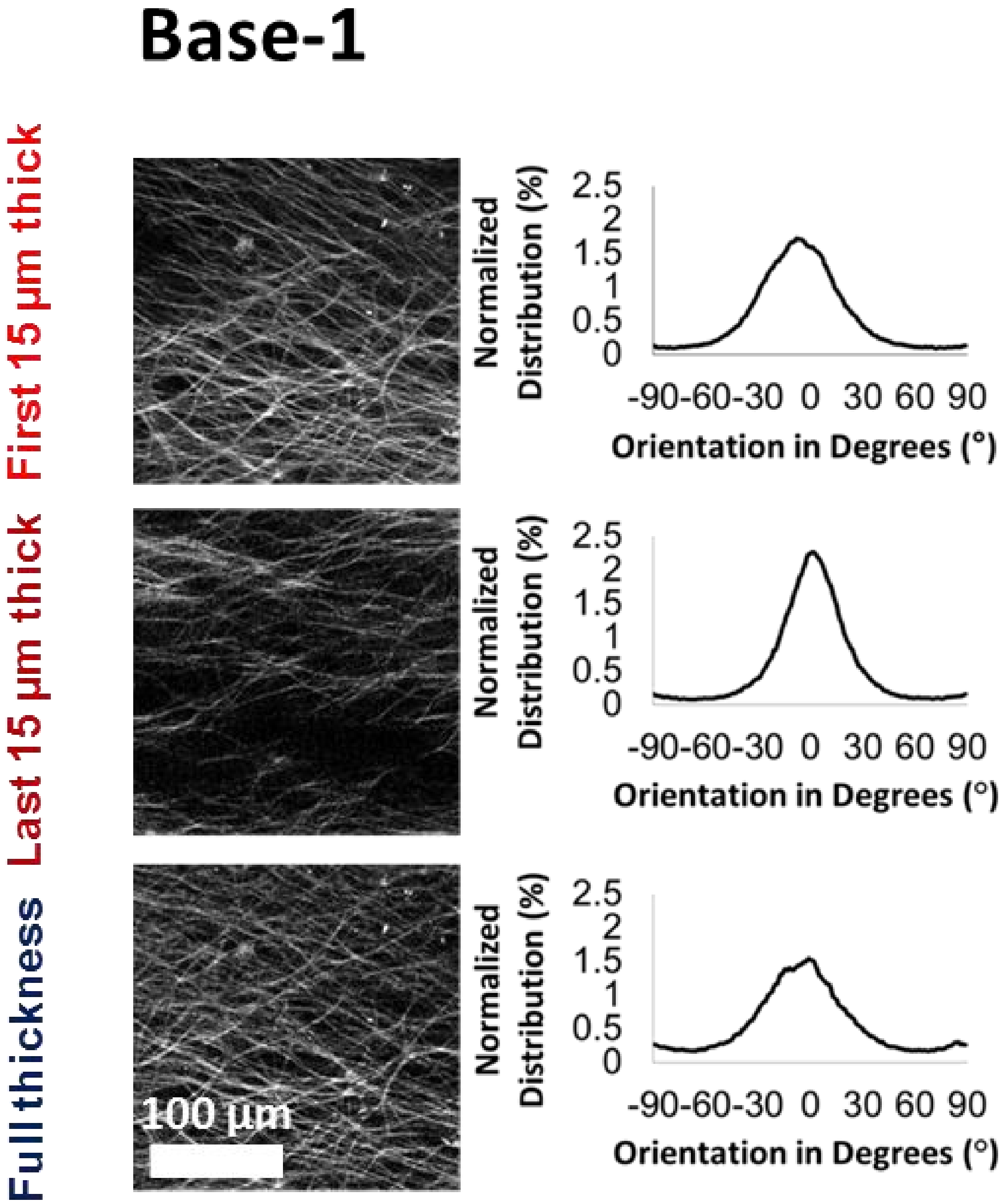

Figure 2.4 Layered epicardial elastin networks at the location of basal anterior (B1) of the left ventricle.

Note: Projections and normalized fiber distributions obtained from the location of basal anterior (B1). Top panel: the first 15 µm thick layer; Middle panel: the last 15 µm thick layer; Bottom panel: the full thickness of the sample. Scale bar = 100 µm.

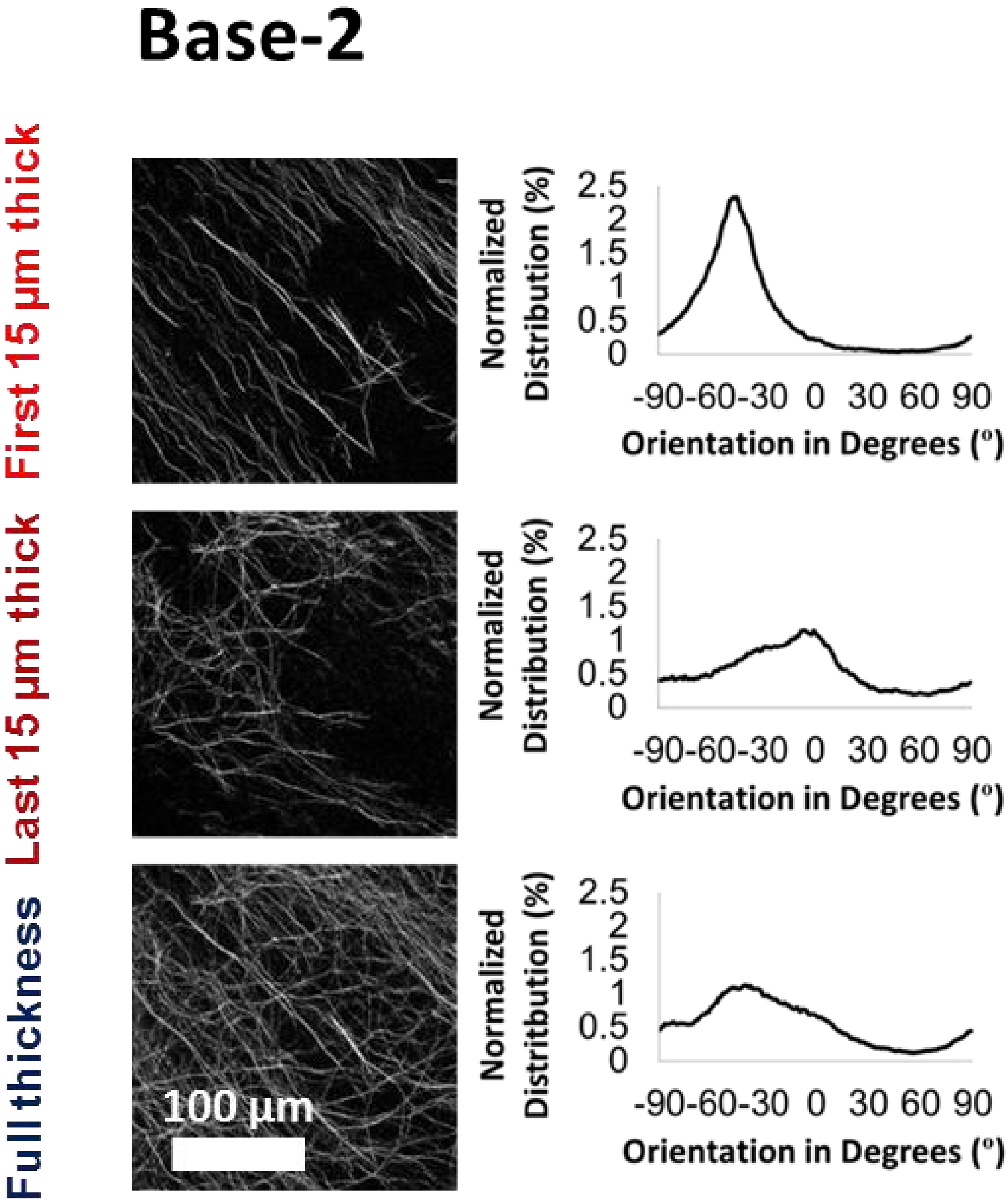

Figure 2.5 Layered epicardial elastin networks at the location of basal anterior (B2) of the left ventricle.

Note: Projections and normalized fiber distributions obtained from the location of basal anterior (B2). Top panel: the first 15 µm thick layer; Middle panel: the last 15 µm thick layer; Bottom panel: the full thickness of the sample. Scale bar = 100 µm.

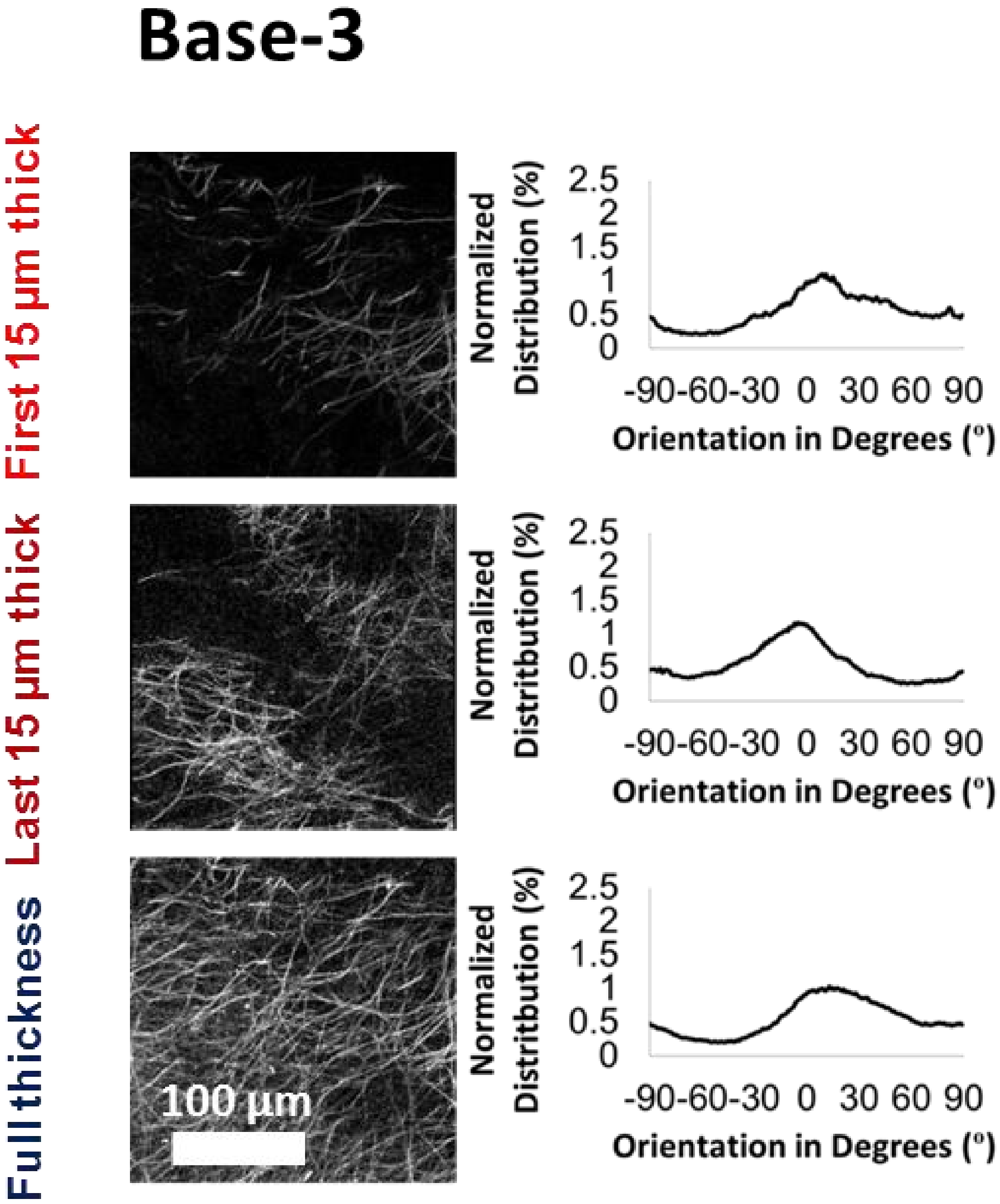

Figure 2.6 Layered epicardial elastin networks at the location of basal lateral (B3) of the left ventricle.

Note: Projections and normalized fiber distributions obtained from the location of basal lateral (B3). Top panel: the first 15 µm thick layer; Middle panel: the last 15 µm thick layer; Bottom panel: the full thickness of the sample. Scale bar = 100 µm.

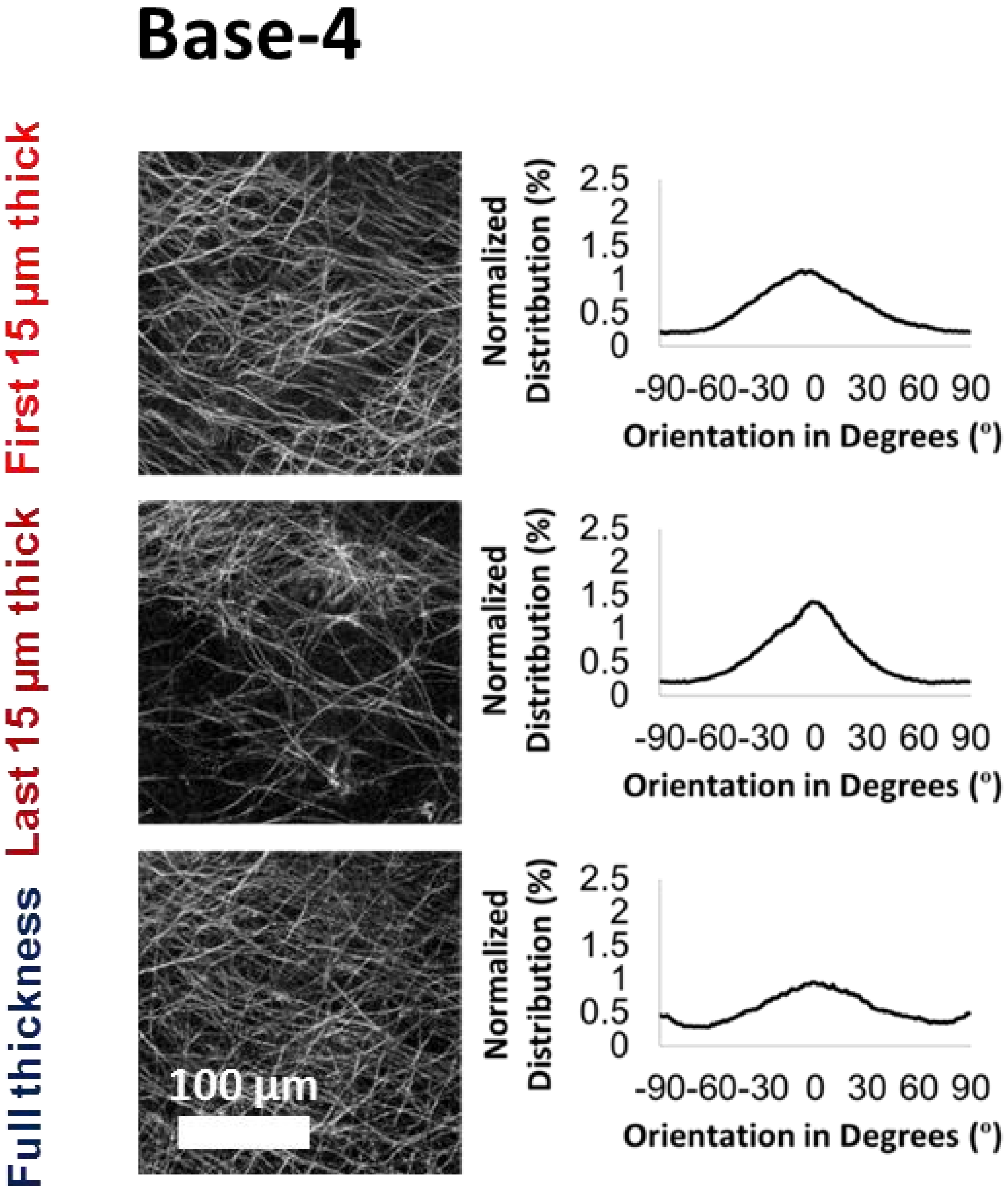

Figure 2.7 Layered epicardial elastin networks at the location of basal posterior (B4) of the left ventricle.

Note: Projections and normalized fiber distributions obtained from the location of basal posterior (B4). Top panel: the first 15 µm thick layer; Middle panel: the last 15 µm thick layer; Bottom panel: the full thickness of the sample. Scale bar = 100 µm.

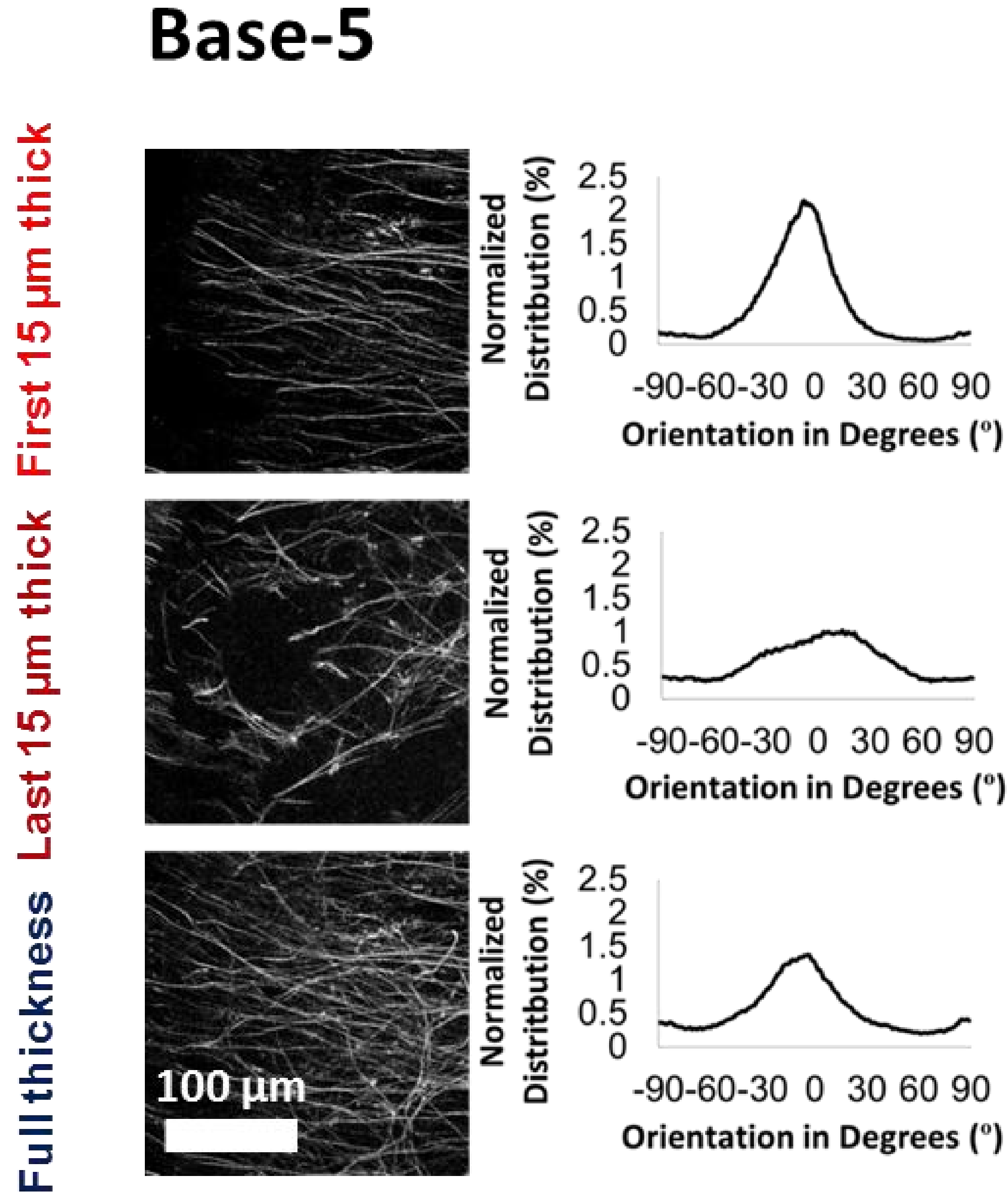

Figure 2.8 Layered epicardial elastin networks at the location of basal posterior (B5) of the left ventricle.

Note: Projections and normalized fiber distributions obtained from the location of basal posterior (B5). Top panel: the first 15 µm thick layer; Middle panel: the last 15 µm thick layer; Bottom panel: the full thickness of the sample. Scale bar = 100 µm.

All four locations from the middle region of the LV were analyzed by the same method of confocal microscopy. Figure 2.9 represents the outermost location from the anterior side (Middle-1). The top panel indicated that elastin fibers in the first 15 µm ran laterally (left) with a wide range of angle of inclination. When reaching the deep layer, most elastin fibers aligned more toward -80°. In the location of Middle-2 (Figure 2.10), elastin fibers in both the first and last 15 µm had an overall alignment at -60°, while the alignment of the last 15 µm was slightly higher. In the location of Middle-3 (Figure 2.11), in the first 15 µm layer elastin fibers highly aligned along horizontal direction, while in the last 15 µm layer elastin fibers had an overall alignment toward -60°. In the location of middle-4 (Figure 2.12), elastin fibers in the first 15 µm have an alignment along -45°, while in the last 15 µm elastin fibers exhibited a more random orientation.

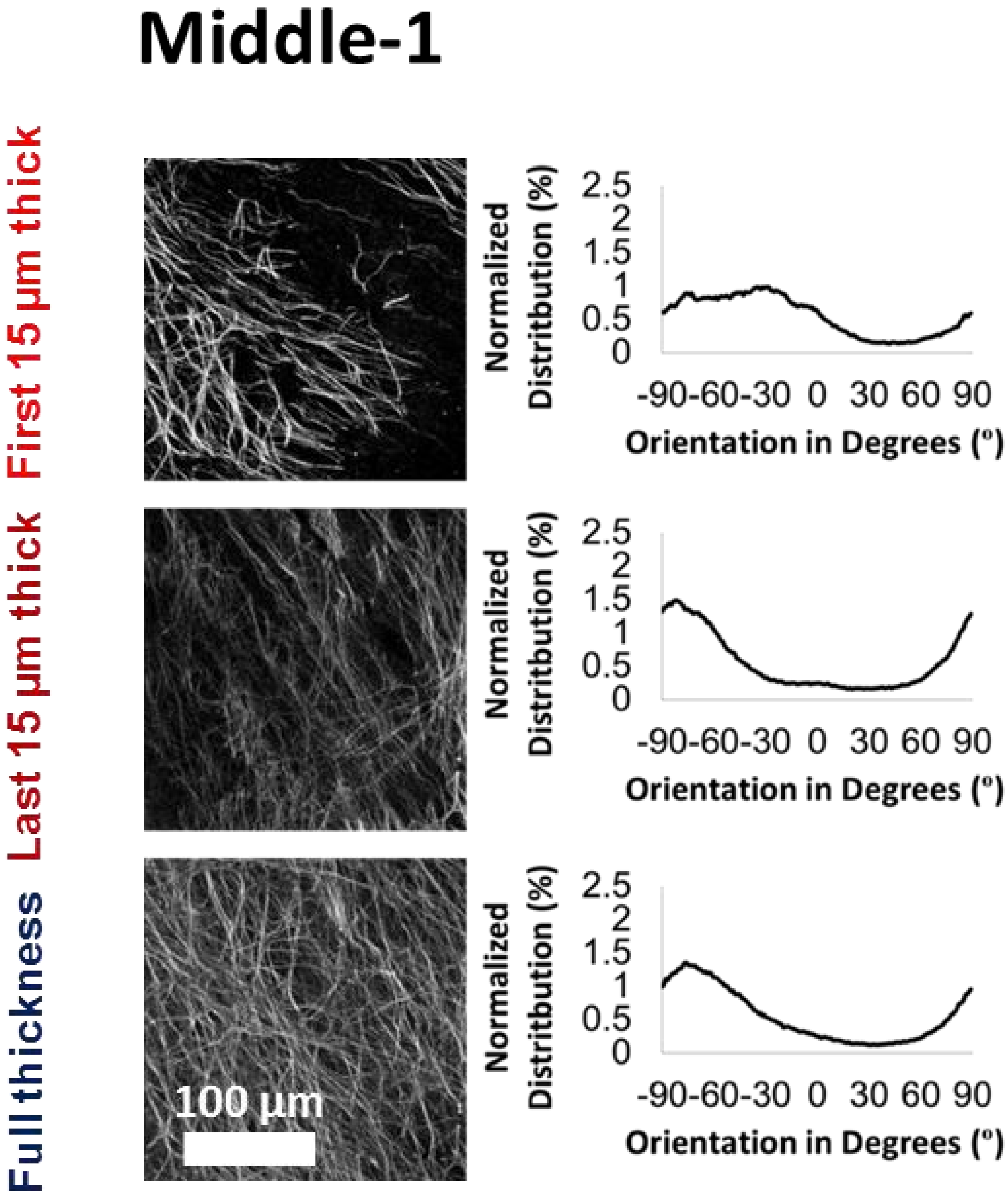

Figure 2.9 Layered epicardial elastin networks at the location of middle anterior (M1) of the left ventricle.

Note: Projections and normalized fiber distributions obtained from the location of middle anterior (M1). Top panel: the first 15 µm thick layer; Middle panel: the last 15 µm thick layer; Bottom panel: the full thickness of the sample. Scale bar = 100 µm.

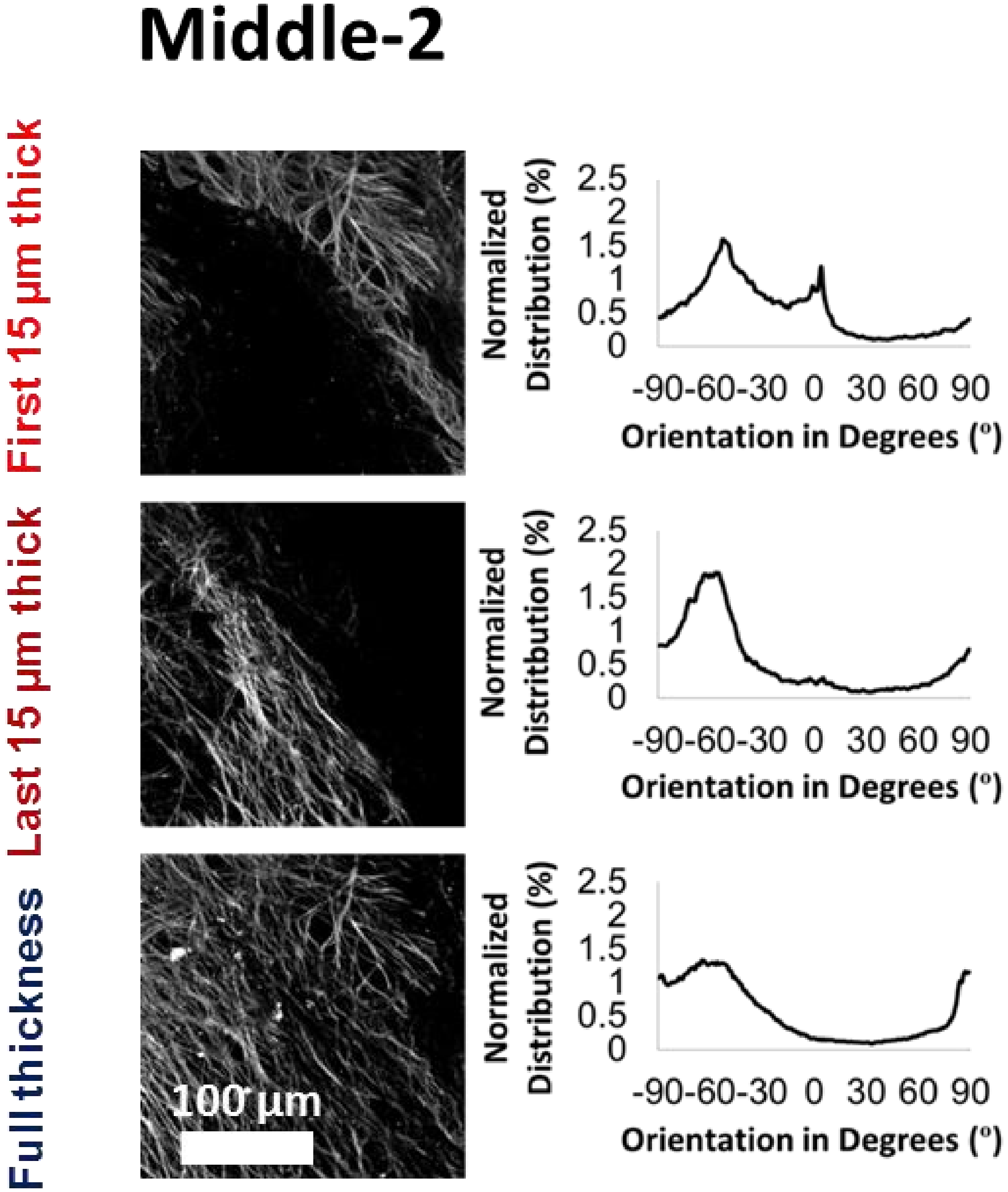

Figure 2.10 Layered epicardial elastin networks at the location of middle anterior (M2) of the left ventricle.

Note: Projections and normalized fiber distributions obtained from the location of middle anterior (M2). Top panel: the first 15 µm thick layer; Middle panel: the last 15 µm thick layer; Bottom panel: the full thickness of the sample. Scale bar = 100 µm.

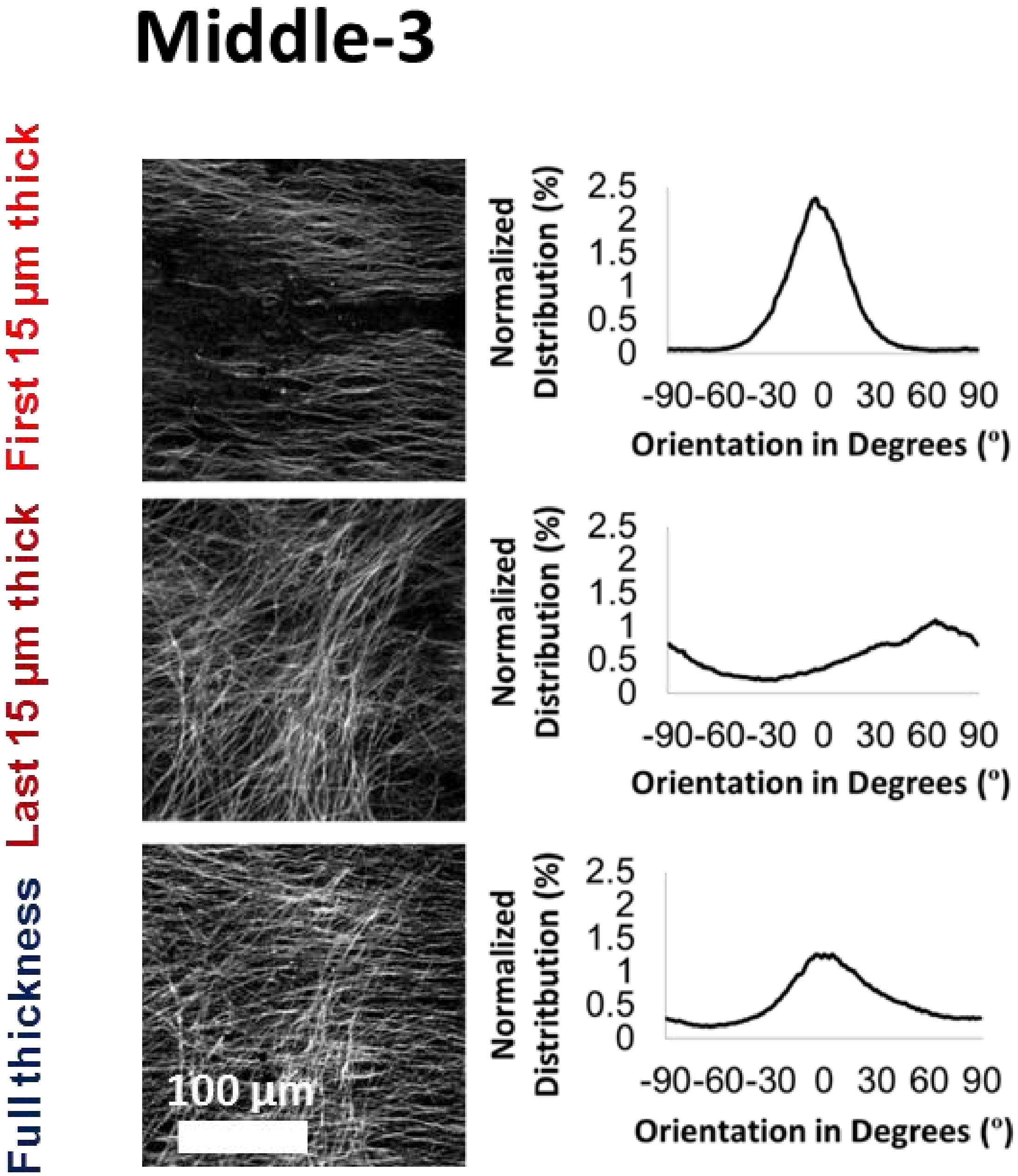

Figure 2.11 Layered epicardial elastin networks at the location of middle lateral (M3) of the left ventricle.

Note: Projections and normalized fiber distributions obtained from the location of middle lateral (M3). Top panel: the first 15 µm thick layer; middle panel: the last 15 µm thick layer; bottom panel: the full thickness of the sample. Scale bar = 100 µm.

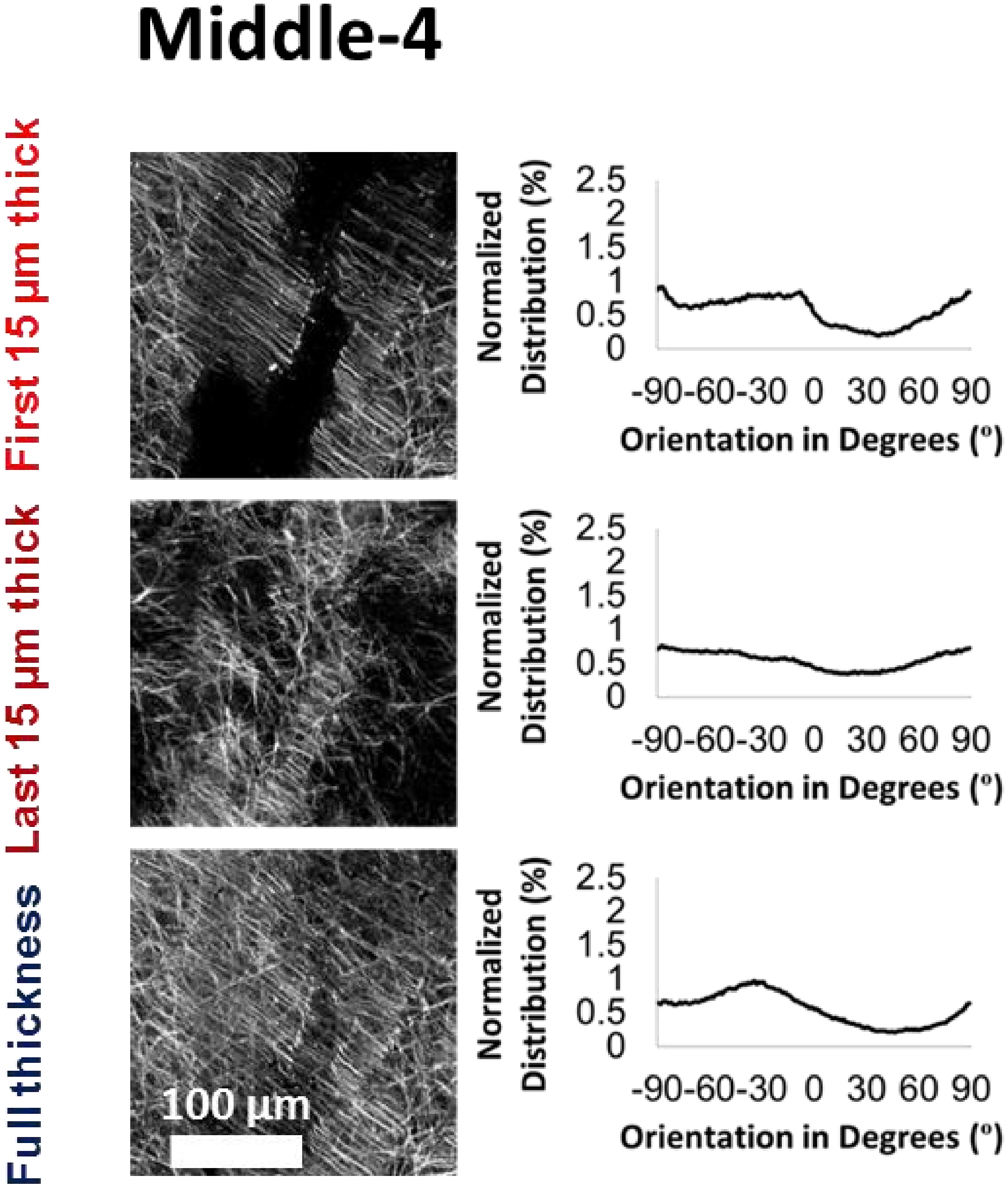

Figure 2.12 Layered epicardial elastin networks at the location of middle posterior (M4) of the left ventricle.

Note: Projections and normalized fiber distributions obtained from the location of middle posterior (M4). Top panel: the first 15 µm thick layer; middle panel: the last 15 µm thick layer; bottom panel: the full thickness of the sample. Scale bar = 100 µm.

Figures 2.12 – 2.14 depict the alignment and orientation of elastin fibers from all three locations in the apex region. In Figure 2.13 (Apex-1), the first 15 µm layer showed alignment around 90°, but the last 15 µm layer had a more random elastin fiber distribution. A unique pattern was observed in the location Apex-2 (Figure 2.14) which was the sample obtained from the apex point. Elastin fibers in the first 15 µm layer displayed a spiral helix-like structure, while highly oriented elastin fibers were found align along 20° in the last 15 µm layer. In the location of Apex-3 (Figure 2.15), both the first and last 15 µm elastin fibers were found aligned 90°.

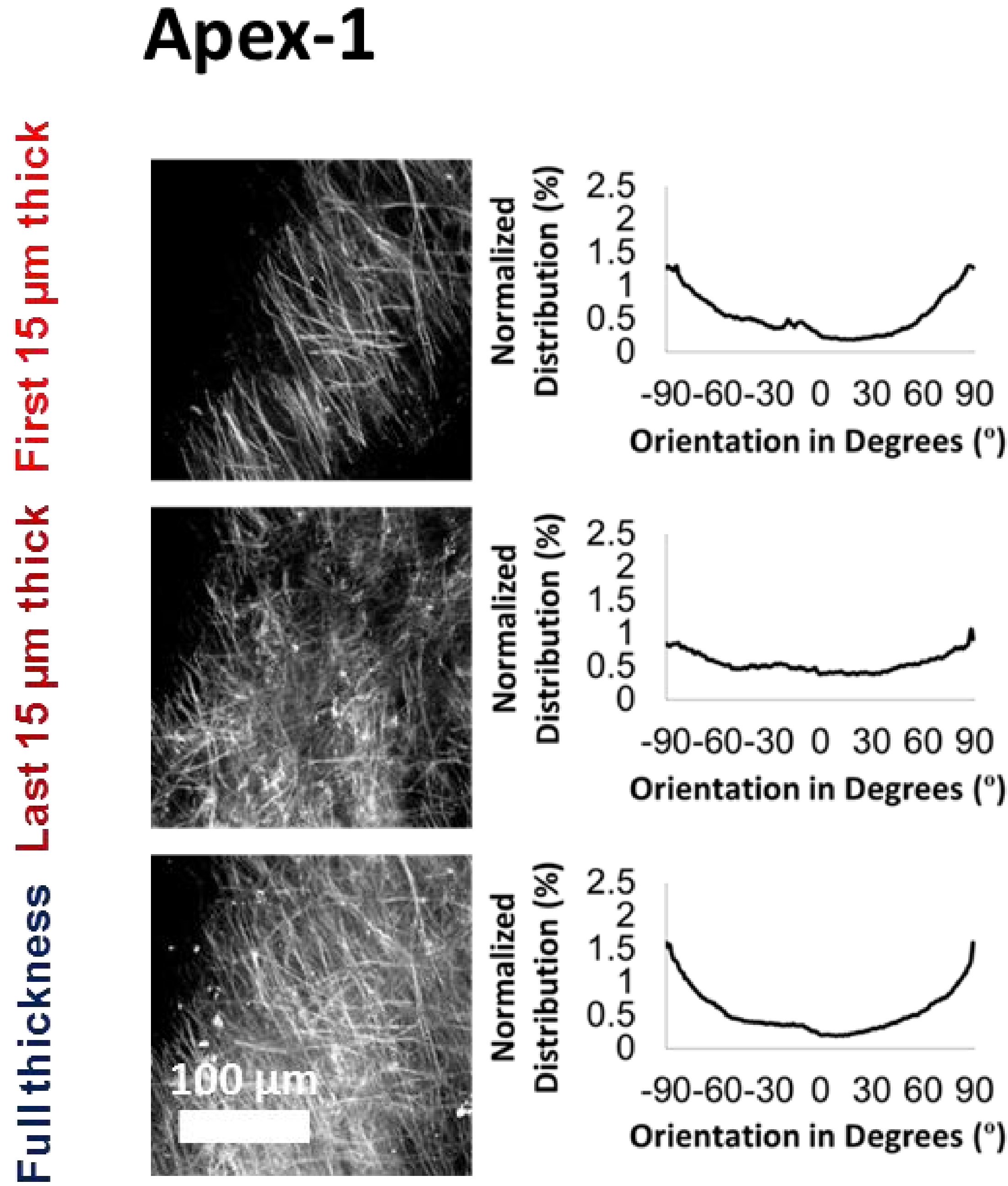

Figure 2.13 Layered epicardial elastin network at the location of apex anterior (A1) of the left ventricle.

Note: Projections and normalized fiber distributions obtained from the location of apex anterior (A1). Top panel: the first 15 µm thick layer; Middle panel: the last 15 µm thick layer; Bottom panel: the full thickness of the sample. Scale bar = 100 µm.

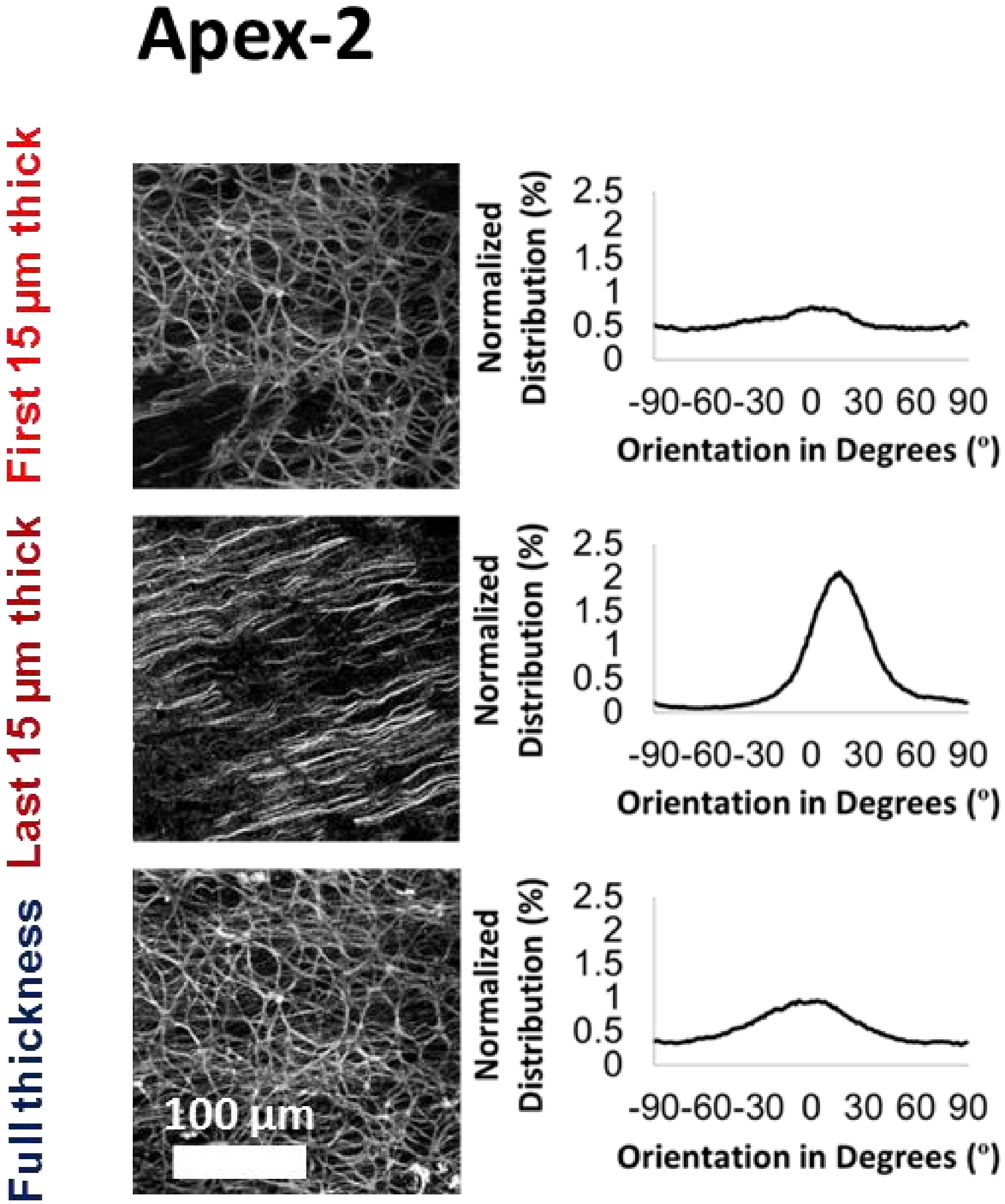

Figure 2.14 Layered epicardial elastin network at the location of apex point (A2) of the left ventricle.

Note: Projections and normalized fiber distributions obtained from the location of apex point (A2). Top panel: the first 15 µm thick layer; Middle panel: the last 15 µm thick layer; Bottom panel: the full thickness of the sample. Scale bar = 100 µm.

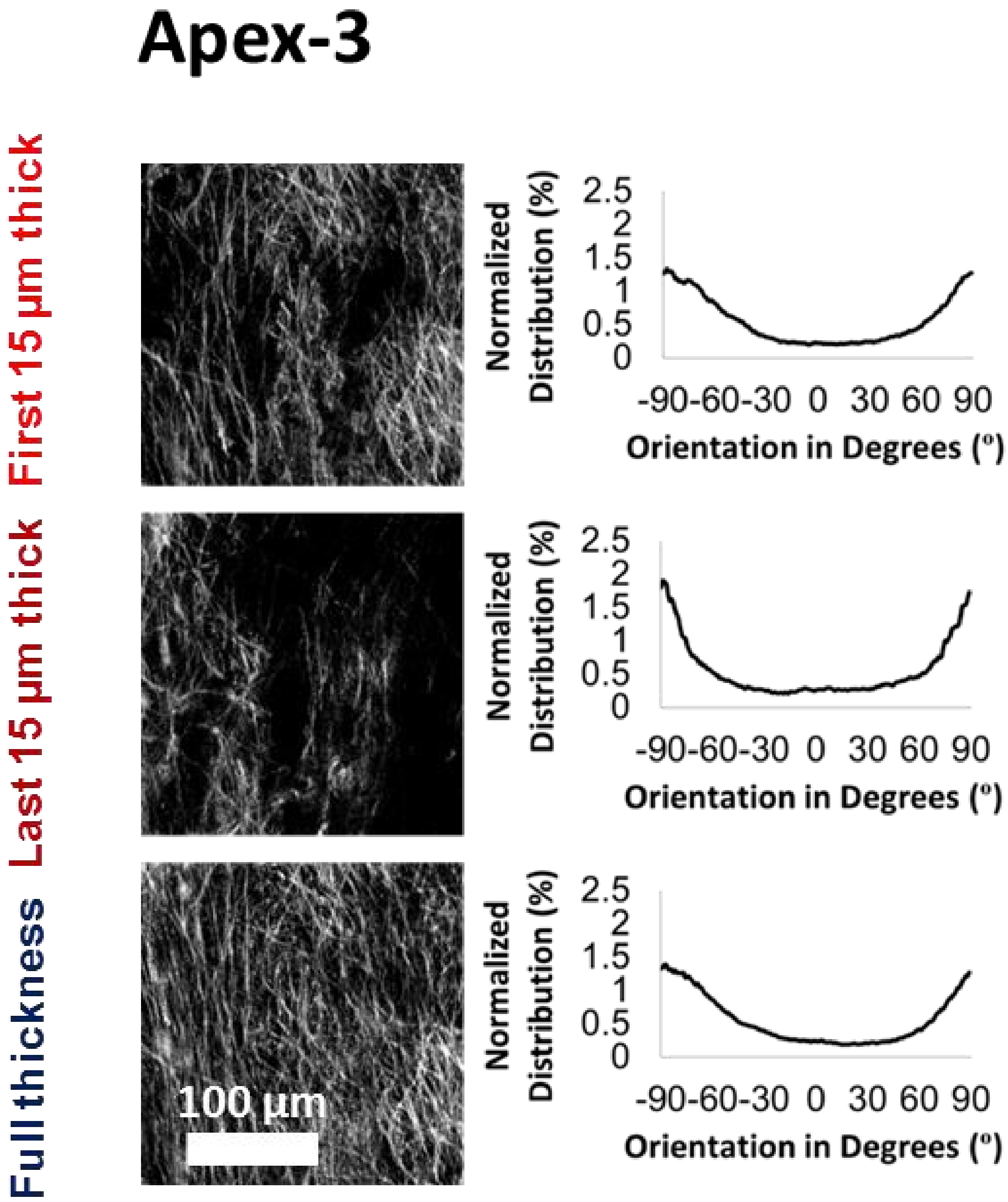

Figure 2.15 Layered epicardial elastin network at the location of apex posterior (A3) of the left ventricle.

Note: Projections and normalized fiber distributions obtained from the location of apex posterior (A3). Top panel: the first 15 µm thick layer; middle panel: the last 15 µm thick layer; bottom panel: the full thickness of the sample. Scale bar = 100 µm.

2.3.4 Histological Study of Cardiac Elastin

To obtain details of the cardiac elastin microstructure, a conventional histological method was then utilized. Native cardiac samples without decellularization were stained with Movat’s pentachrome. In the epicardium (Figure 2.16), elastin fibers (black) associated with collagen (yellow) covered a thickness range of ~ 100 – 200 µm. We noticed that different locations had various elastin fiber configurations, which verified the observations of our elastin mapping study (Figure 2.24).

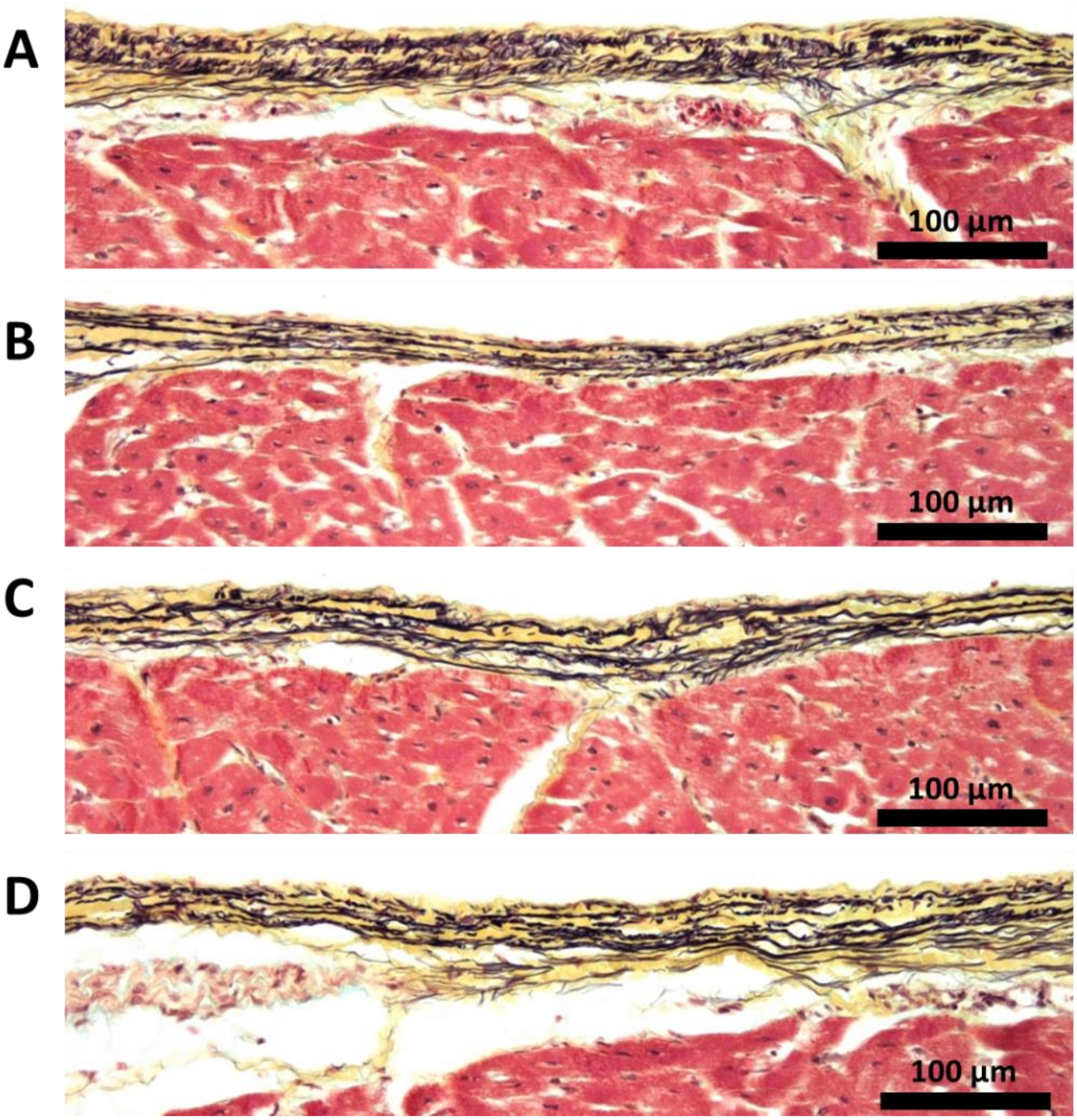

Figure 2.16 Histological images of the LV epicardial cross-sections with epicardial elastin morphology.

Note: Histological images of the epicardial cross-sections in the left ventricle were stained with Movat's pentachrome. Collagen is in yellow, elastin fibers in black, cardiac muscles in red, and Purkinje fibers in pale red. Scale bar = 100 µm.

Histological images in Figure 2.17 were obtained to illustrate typical patterns of endocardial elastin. Similar to the epicardial layer, different locations showed different microstructures. We also noticed the thickness of the endocardium was greater than the epicardium. The elastin fibers were also found to be denser, with a higher elastin-collagen ratio shown by Movat’s pentachrome staining. The elastin fibers also looked finer when compared to the elastin fibers in the epicardium.

Movat’s pentachrome staining was also able to detect the interstitial elastin fibers in the cardiac ECM (Figures 2.18 and 2.19). A close look in our histology results shows that interstitial elastin fibers in myocardium were sparse and mainly associated with the perimysial collagen that wraps around muscle bundles, and rarely associated with the endomysial collagen that ensheaths each individual muscle fiber (Figures 2.18 and 2.19). The vascular elastin was abundant in the walls of the blood vessels and a network of elastin was also found associated with the collagen network that meshes the blood vessels to the surrounding tissue (Figure 2.20).

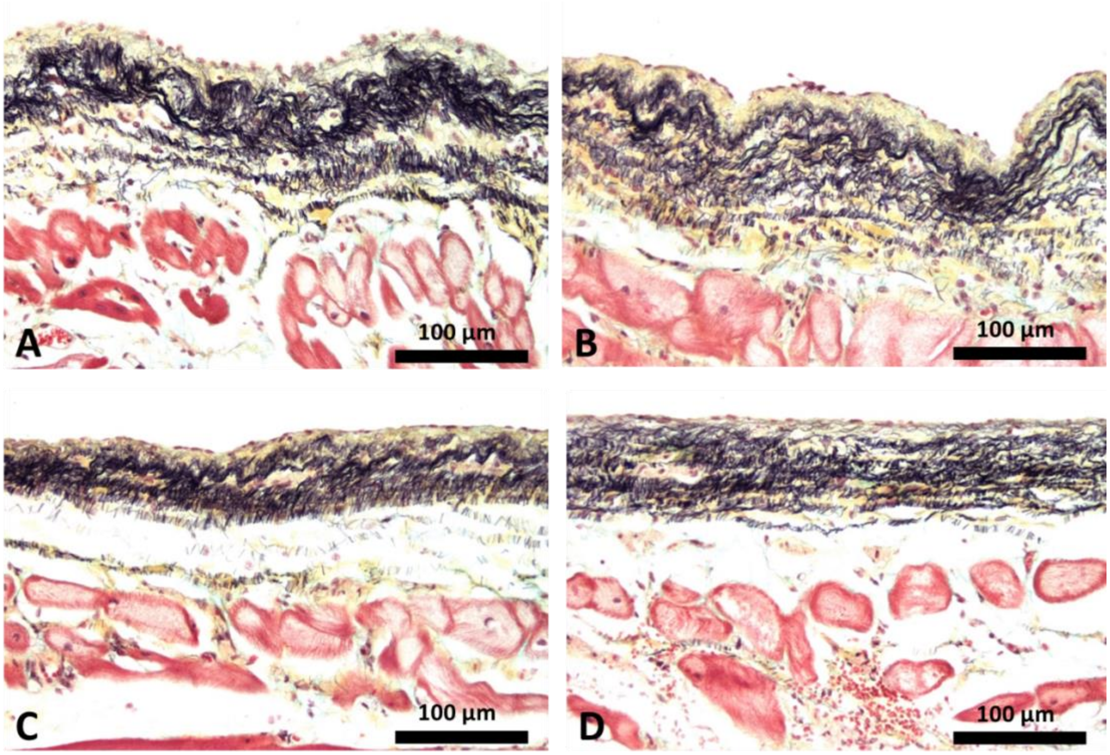

Figure 2.17 Histological images of the LV endocardial cross-sections with endocardial elastin morphology.

Note: Histological images of the endocardial cross-sections in the left ventricle were stained with Movat's pentachrome. Collagen is in yellow, elastin fibers in black, cardiac muscles and blood vessels in red. Scale bar = 100 µm.

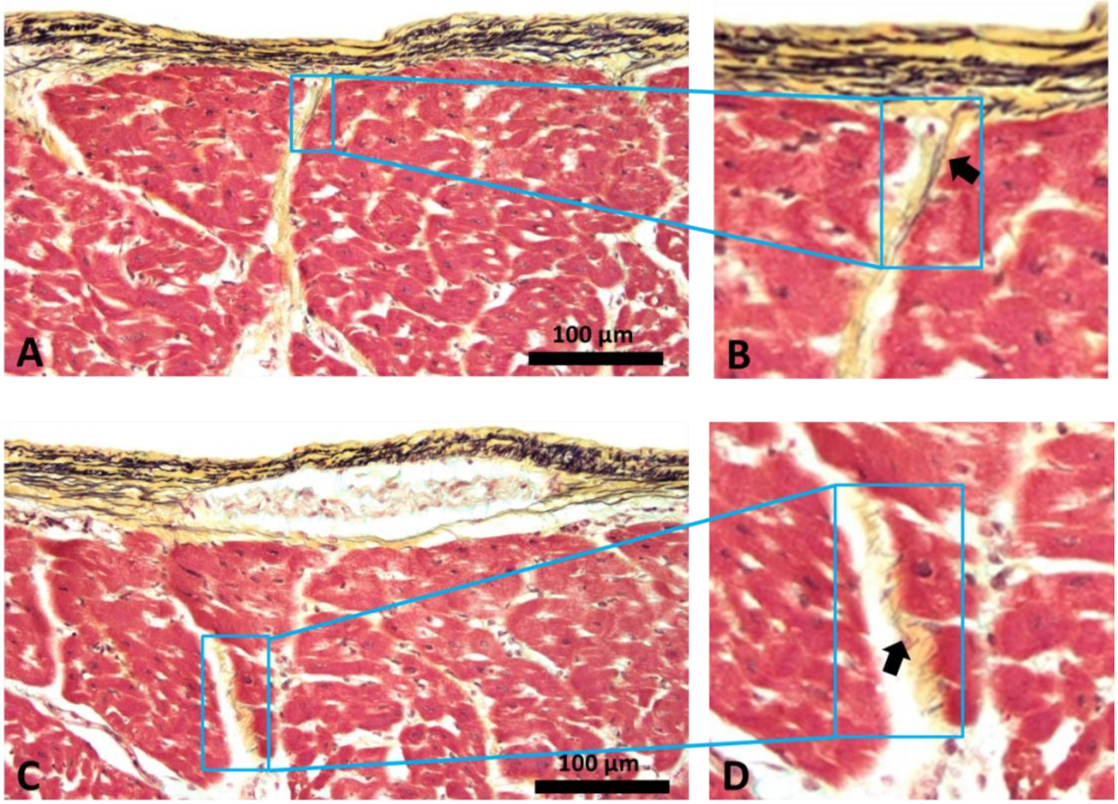

Figure 2.18 Histological images of the LV myocardial cross-sections with interstitial elastin fiber morphology highlighted.

Note: Histological images of the myocardial cross-sections in the left ventricle were stained with Movat's pentachrome Collagen is in yellow, elastin fibers in black, and cardiac muscles in red. Arrows in B and D point out zoomed in areas in A and C. Scale bar = 100 µm.

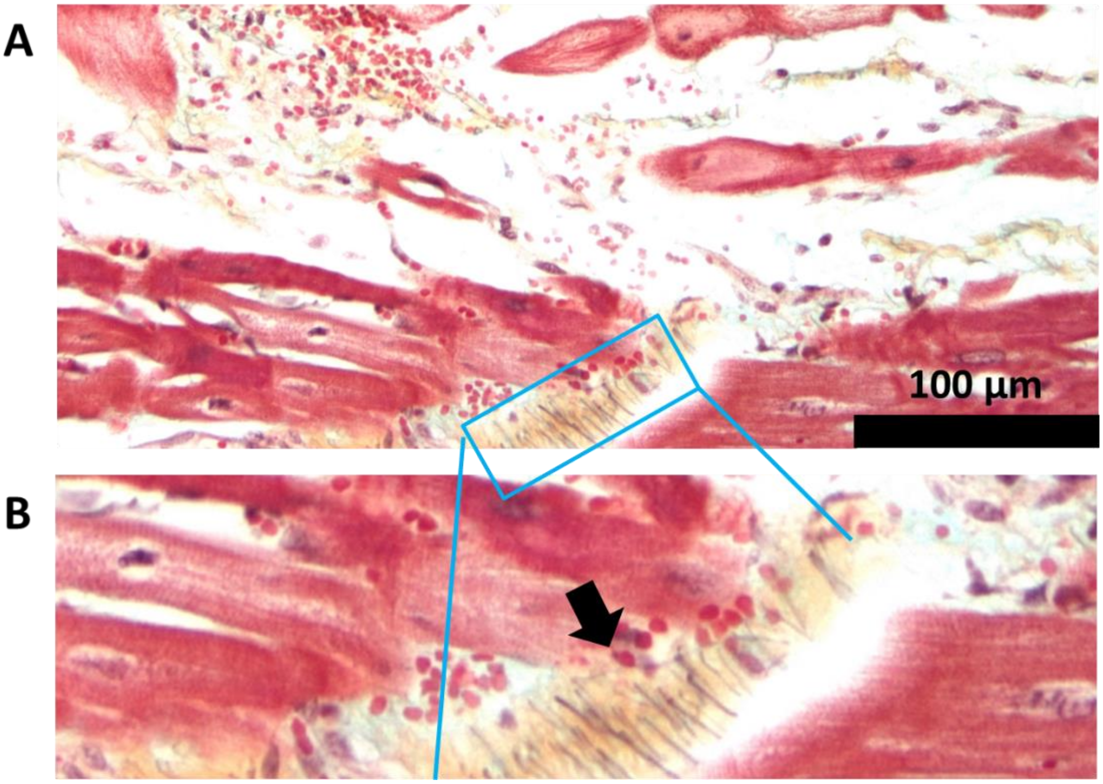

Figure 2.19 Histological images of the LV myocardial cross-sections showing interstitial elastin fibers in the perimysium.

Note: Histological images of the myocardial cross-sections in the left ventricle were stained with Movat's pentachrome. Collagen is in yellow, elastin fibers in black, and cardiac muscles in red. Arrows in B points out the zoomed in area in A. Scale bar = 100 µm.

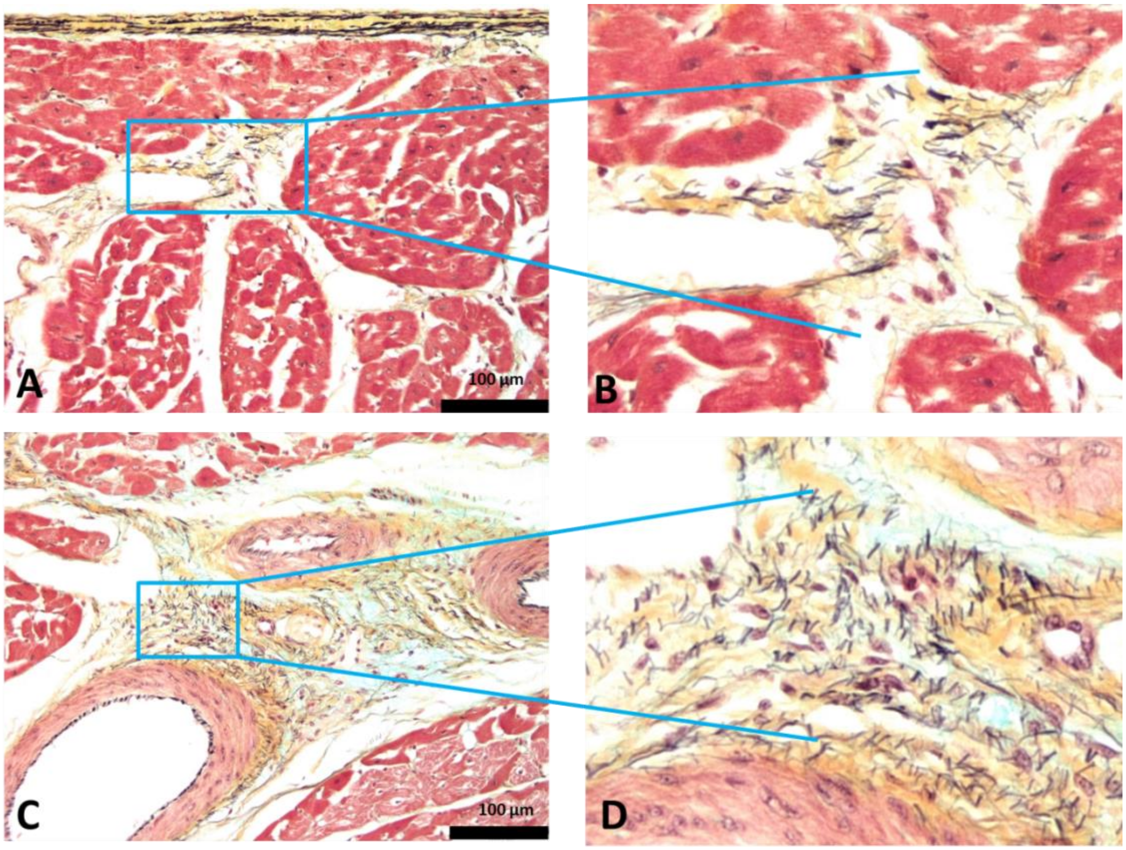

Figure 2.20 Histological images of the LV myocardial cross-sections featuring blood vessels surrounded with cardiac elastin fibers.

Note: Histological images of the myocardial cross-sections featuring blood vessels surrounded elastin fibers in the left ventricle were stained with Movat's pentachrome. Collagen is in yellow, elastin fibers in black, cardiac muscles in red, and Purkinje fibers in pale red. Arrows in B and D point out zoomed in areas in A and C. Scale bar = 100 µm.

We also found that elastin fibers associated with the Purkinje fibers, whose function to send electrical impulses to the cardiomyocytes in the ventricles of the heart. Figure 2.21-A shows a loose elastin fiber network wrapping around the Purkinje fibers and filling out conjunction gaps. Interestingly, elastin fibers were also observed scattering among the Purkinje fibers (Figures 2.21 (B, C) and 2.22).

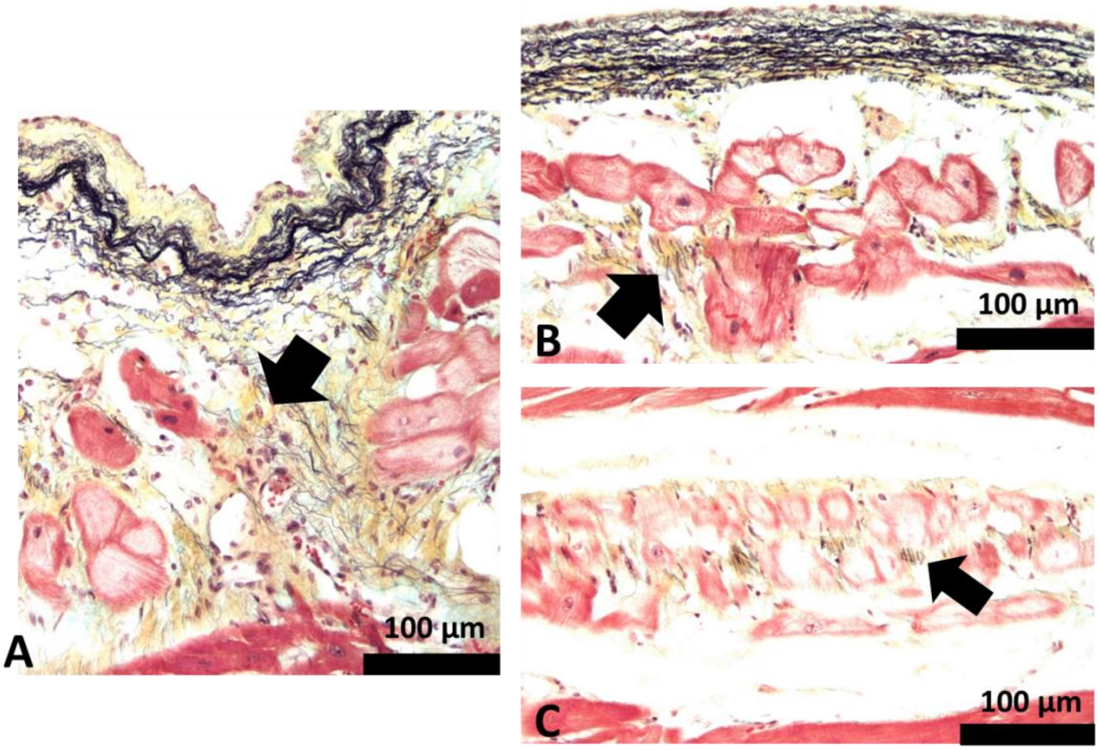

Figure 2.21 Histological images of the LV endocardial cross-sections showing Purkinje fibers-cardiac elastin fiber association.

Note: Histological images of the endocardial cross-sections in the left ventricle were stained with Movat's pentachrome. Collagen is in yellow, elastin fibers in black, cardiac muscles in red, and Purkinje fibers in pale red. Arrows in A, B, and C indicate scattered elastin fibers. Scale bar = 100 µm.

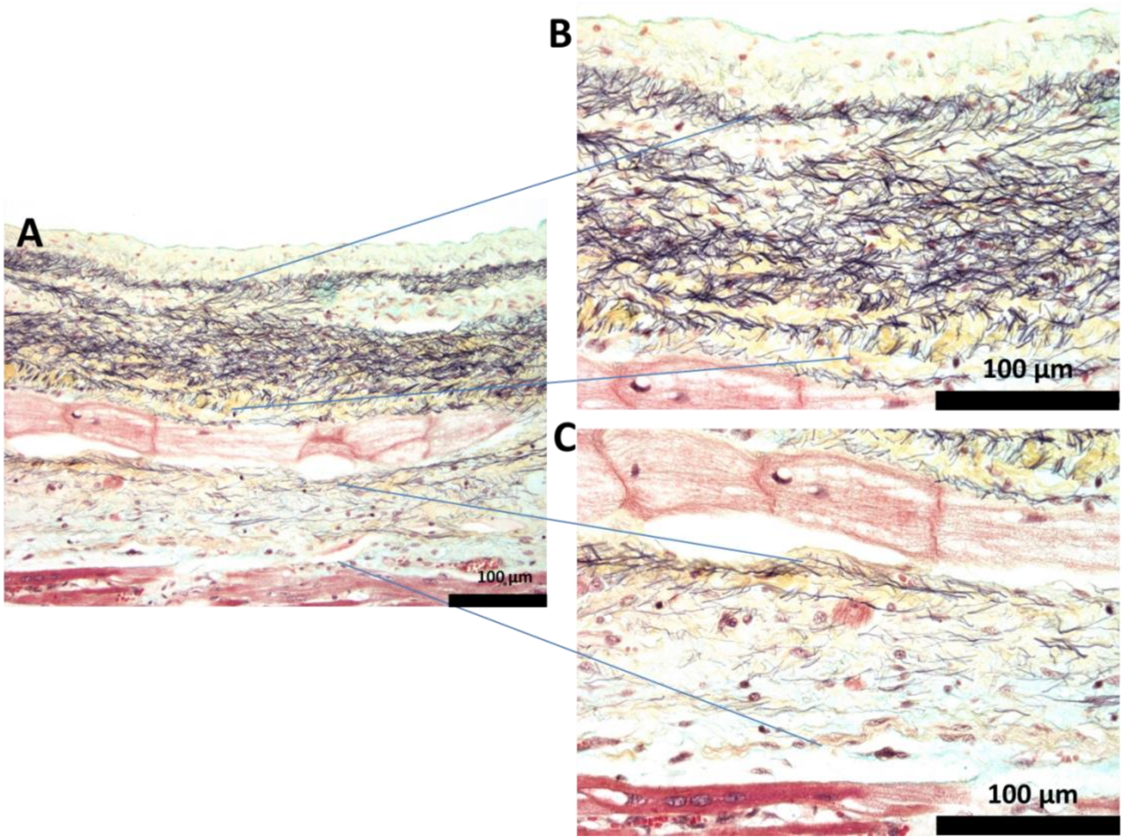

Figure 2.22 Histological images of the LV endocardial cross-sections showing cardiac elastin fibers associated with Purkinje fibers.

Note: Histological images of the endocardial cross-sections with Purkinje fibers in the left ventricle were stained with Movat's pentachrome Collagen is in yellow, elastin fibers in black, cardiac muscles in red, and Purkinje fibers in pale red. Scale bar = 100 µm.

2.4 Discussion

2.4.1 Mapping of Epicardial Elastin Fiber Network

This study aims to investigate the overall 3D microstructures of cardiac elastin in the left ventricle (LV) of porcine heart. By means of LSCM, we were able to create a mapping of the elastin network in the epicardium of the left ventricle. The overall mapping of epicardial elastin fiber networks in the LV is highly location-dependent and depth-dependent. Projections of full thicknesses from various locations reveal the overall orientation/alignment of elastin fibers in the LV in a thoroughly manner for the first time (Figure 2.3). We have also noticed that the overall architecture of the epicardial elastin network from the base to the apex (Figure 2.3) has a degree of correlation with the helical heart muscle fiber orientation revealed by our previous Diffusion-Tensor Magnetic Resonance Imaging (DT-MRI) study (Figure 2.23) (Zhang et al., 2010).

Figure 2.23 DT-MRI fiber structure of a normal heart explant.

Normal multilayered helical DT-MRI myocardial fibers were detected.

In comparison to the data from the epicardial layer using two-photon excitation fluorescence imaging (TPEF), in which only the first 50 μm was imaged (Jöbsis et al., 2007), we were able to image and analyze a more detailed 3D microstructure of the epicardial elastin fibers by LSCM. In our study, (i) we provided a thorough anatomically location-dependent elastin fiber map; (ii) the comparison between two different depths (the first 15 μm thick layer and the last 15 μm thick layer) demonstrated that elastin fibers often switch orientation/alignment patterns at different depths.

2.4.2 Histological Analyses

Two reasons caused us to only focus on 3D epicardial elastin mapping using LSCM, i.e., (i) LSCM cannot detect the very weak interstitial elastin signals in the myocardium due to the fact of sparse distribution of the interstitial elastin fibers; (ii) the endocardial elastin fibers are finer and much denser than the epicardial elastin fibers, and thus resulting in the diffused endocardial elastin signal difficult for individual fiber distinguishing and 3D analysis. We hence pursued the morphological study on interstitial elastin fibers in the myocardium, endocardial elastin fibers, as well as elastin fibers around the Purkinje fibers. The cross-sections of the native epicardium, endocardium, and myocardium were stained with Movat's pentachrome to delineate the distribution and morphology of different types of cardiac elastin fibers.

Note that the depth-dependency of the epicardial elastin fibers was further verified by Movat's pentachrome histology, which shows elastin fibers switch orientation at different sublayers (Figure 2.24).

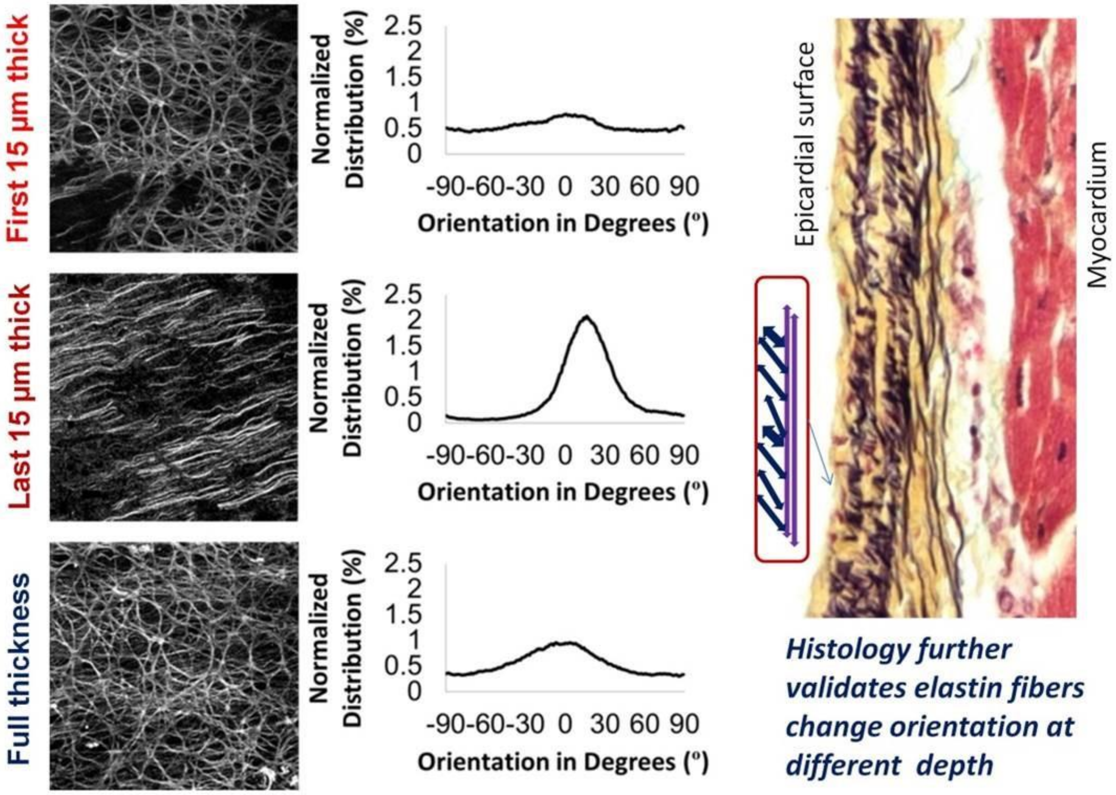

Figure 2.24 LSCM data on porcine hearts demonstrate that the epicardial elastin fiber network shows depth-dependency.

Note: The depth-dependency is also verified by histological observation. Movat's pentachrome stains elastin in black, heart muscle in read, and collagen in yellow.

For the interstitial elastin fibers in the myocardium, our major findings are (i) the interstitial elastin fibers sparsely co-exist with the perimysial collagen, helping bind the cardiomyocyte bundles; (ii) some interstitial elastin fibers even show hinge-like structures to connect the adjacent cardiomyocyte bundles (Figure 2.18 and 2.19). Those morphologies imply that the interstitial elastin fibers in the perimysium may function as hinges between different cardiac muscle bundles to assist with force transfer and recoiling (Figures 2.18 and 2.19).

Purkinje fibers have the significant function in conducting electrical impulse to the myocardium (Mendez, Mueller, & URGUIAGA, 1970; Rentschler et al., 2001; Sanguinetti & Kass, 1984; Vassalle, 1970). Our histological observations (Figures 2.21 and 2.22) showed that there are always cardiac elastin fibers, along with collagen fibers, closely associate with the Purkinje fibers. Various patterns of co-existence of the Purkinje fibers and cardiac elastin fibers have been revealed in Figures 2.21 and 2.22. One might speculate that those Purkinje fibers-associated cardiac elastin fibers may serve as functions such as a protective wrapping and an energy saving recoiling during the heart beating cycles.

In conclusion, our study proposed a detailed mapping of the epicardial elastin network in the left ventricle for the first time. We found that the elastin network shows certain patterns that are highly correlated to their anatomical locations. Besides the locational variation, epicardial elastin network also shows a 3D microstructural alteration from the surface to the deeper layers. Histological staining was applied to verify the 3D findings and provide supplemental details of interstitial elastin fibers (or called myocardial elastin fibers) and endocardial elastin fibers. The observed elastin fiber pattern, fiber orientation, and fiber alignment have the potential to help explain the biomechanical functions that help coordinating the heart contraction and relaxation.

CHAPTER III

RECONSTRUCT 3D NETWORK OF THE ELASTIN FIBER NETWORK AND EXAMINE BOTH THE TOPOLOGY AND GEOMETRY OF THIS NETWORK

3.1 Introduction

To understand the microstructure of the elastin fiber network, a variety of imaging methods were utilized in previous studies, including: two-photon excitation fluorescence imaging (TPEF) (Jöbsis et al., 2007), transmission electron microscopy (TEM) (Robinson et al., 1983), scanning electron microscopy (SEM) (Lu, Ganesan, Simionescu, & Vyavahare, 2004; Vesely, 1997), as well as laser scanning confocal microscopy (LSCM) in our "elastin fiber network mapping" study in Chapter II. The configuration of fiber networks in soft tissues is always intriguing and needs better understanding and quantification. As an example, D'Amore, Stella, Wagner, and Sacks (2010) reported an SEM image-based approach to characterize the 2D topology of collagen fibers in an engineered tissue scaffold obtained from rat carotid arteries. From the basic imaging analysis algorithm developed from MatLab (The MathWorks Inc., MA), general topological descriptors, such as fiber diameter/orientation/intersections, were extracts from the fiber network. However, current imaging techniques display limited descriptions of the full fiber network, such as fiber branching, 3D orientation distribution, numbers of branching points in the network, number of cliques, etc.

In this chapter, we developed an in-house 3D confocal image-based analysis algorithm to collect the fiber network descriptors and compute the reconstructed 3D topological and geometrical fiber metrics. Drawing knowledge from graph theory, topology, and image processing, we can extract the abstract elastin network from the LSCM imaging data, which can then be subjected to rigorous mathematical and statistical analysis.

3.2 Materials and Methods

3.2.1 Fiber Segmentation

Confocal microscopy images are noisy. A simple threshold based method that identified pixels with high intensities as fibers can generate spurious features and miss true fibers. Several approaches have been proposed in the literature for the related work of the blood vessel reconstruction. These approaches range from pre-segmentation (Florin, Moreau-Gobard, & Williams, 2004; Ronse, Baruthio, Armspach, & Maillot, 2006; Shikata, Hoffman, & Sonka, 2004), region-growing (Boskamp et al., 2004; Masutani, Schiemann, & Höhne, 1998; Metz, Schaap, Van Der Giessen, Van Walsum, & Niessen, 2007; Yi & Ra, 2003), active contours (Delingette & Montagnat, 2001; McInerney & Terzopoulos, 1996, 2000; Toledo et al., 2000), centerline-based approaches (Aylward & Bullitt, 2002; Kitagawa & Gersch, 2012; Koller, Gerig, Szekely, & Dettwiler, 1995; Tek, Comaniciu, & Williams, 2001; Ziegel, 1997), and stochastic approaches (Arulampalam, Maskell, Gordon, & Clapp, 2002; Florin, Paragios, & Williams, 2005; Smith, Doucet, de Freitas, & Gordon, 2013). Model-based approaches apply our prior knowledge to the fiber extraction, e.g., the fibers generally have elongated shape with high intensity in the middle of the shape. To study the local behavior of the pixels around a fiber, we examined the Taylor expansion:

$$I(x_0+\Delta x_0) \approx I(x_0)+\Delta x_0 \nabla x_0 + \frac{1}{2}\Delta x_0{}^2 H x_0 \tag{3.1}$$

where ∇x_0 and $H(x_0)$ are the gradient vector and Hessian matrix of the image $I(x_0)$. In particular, a hessian matrix can be used to identify the elongated shape since it gives a differential between the local center region and outside regions. Further, the calculation was carried out in the scale space to account for different radii of the fibers by selecting the largest "fiberness" value from a set of values from results at different scales. Improvement is needed in several places. First, the appropriate filters for the type of noise in the images, including the white noise and the blob-shaped spots, were found out. Second, fiber pixels from the preliminary work were evaluated and false positives and false negatives were identified, and our algorithm accordingly was improved. Repeated LSCM scans on the same sample were collected and built a ground truth by comparing multiple scans, rejecting outliers, as well as comparing to histology. The ground truth data was used to validate the algorithm.

3.2.2 Fiber Skeletonization

While fibers identified in the first step are suitable for 3D rendering, further computation requires an abstract representation of the structure and the connectivity of the fibers. Towards this goal, elastin fibers identified in Step 1 were skeletonized. Curve skeleton has been studied for virtual navigation in anatomy (Perchet, Fetita, & Preteux, 2004; Wan, Dachille, & Kaufman, 2001), computer animation (Bloomenthal, 2002), blood vessel centerline extraction (Aylward & Bullitt, 2002; Aylward, Jomier, Weeks, &

Bullitt, 2003; A. F. Frangi, Niessen, Hoogeveen, Van Walsum, & Viergever, 1999; Fridman, Pizer, Aylward, & Bullitt, 2004), registration (Aylward et al., 2003; Fritsch, Pizer, Morse, Eberly, & Liu, 1994; Pizer, Gerig, Joshi, & Aylward, 2003), matching (Brennecke & Isenberg, 2004; Cornea et al., 2005; Hilaga, Shinagawa, Kohmura, & Kunii, 2001; Sundar, Silver, Gagvani, & Dickinson, 2003), feature tracking (Vrolijk, Reinders, & Post, 2003), etc. For our purpose of reconstructing the elastin network, we require our skeletonization method to be homotopic, thin, centered in the fiber, robust, and smooth. We built our skeletonization method following the strategy used in Lee et al. (Lee, Kashyap, & Chu, 1994). First, we binarized the fiberness images from Step 1. Second, we iteratively removed the outside surface of the fibers if this does not change the homotopy of the fibers. The iteration stopped once we obtained a single-voxel-thick skeleton homotopic to the original fibers. We improved Lee's method by removing small spurious fibers and connected the broken fibers due to noise and imaging artifacts. We also applied anisotropic filters to the fiber images to infer the broken fibers automatically.

3.2.3 Topological and Geometrical Descriptors

Complexity in the elastin network is apparent from preliminary work. Therefore, it is a challenge to capture the essence of this network for gaining insight and further applications. Topological methods are suitable to reduce a complex network to a few key descriptors of the network connectivity. Similar to identifying large patterns in scale space in computer vision (Witkin, 1984), we built a hierarchy of a simplified elastin network. The results can be used for structural comparison, abnormality detection, and persistent feature identification. The hierarchical simplification was carried out by identifying important nodes with graph metrics; e.g., degree or the number of reachable nodes at “n” hops, and iteratively discarded the less important nodes and their edges. Further, we identified special local graph structures with anatomical relevant, e.g., star, chain, clique, bipartite, etc. The distribution of these special local structures in the graph was computed and analyzed. To complement the topological methods, we computed the geometrical shape descriptors from the skeletons including the length, curvatures, radius, etc. The combined topological and geometrical descriptors were utilized to analyze, compare, and visualize the 3D elastin network.

3.2.4 Network-based Metrics

The final step in the 3D constructions is to compute biometrics based on the elastin network. Traditionally biometrics images were computed on a pixel-based approach. We have pioneered the fiber-based metrics on diffusion tensor imaging fibers (Correia et al., 2008). Compared to voxel-based metrics, fiber-based metrics are more specific and more robust to the disturbance to fiber locations across subjects. We introduced the first set of metrics on elastin fibers. Potential metrics including fiber length, average fiber curvature, average scale along fiber, 3D orientation distribution in the network, numbers of branching points in the network, number of cliques in a network would be determined.

3.3 Results

3.3.1 Fiber Segmentation

Multiple-scale vessel enhancement filtering (A. Frangi, Niessen, Vincken, & Viergever, 1998) was used to segment the elastin fibers. A “fiberness” value at each pixel was obtained. The fiberness map was then rendered for display as a mask for further processing. Figure 3.1 shows the volume rendering of the computed fiberness in the confocal images at various locations on the heart.

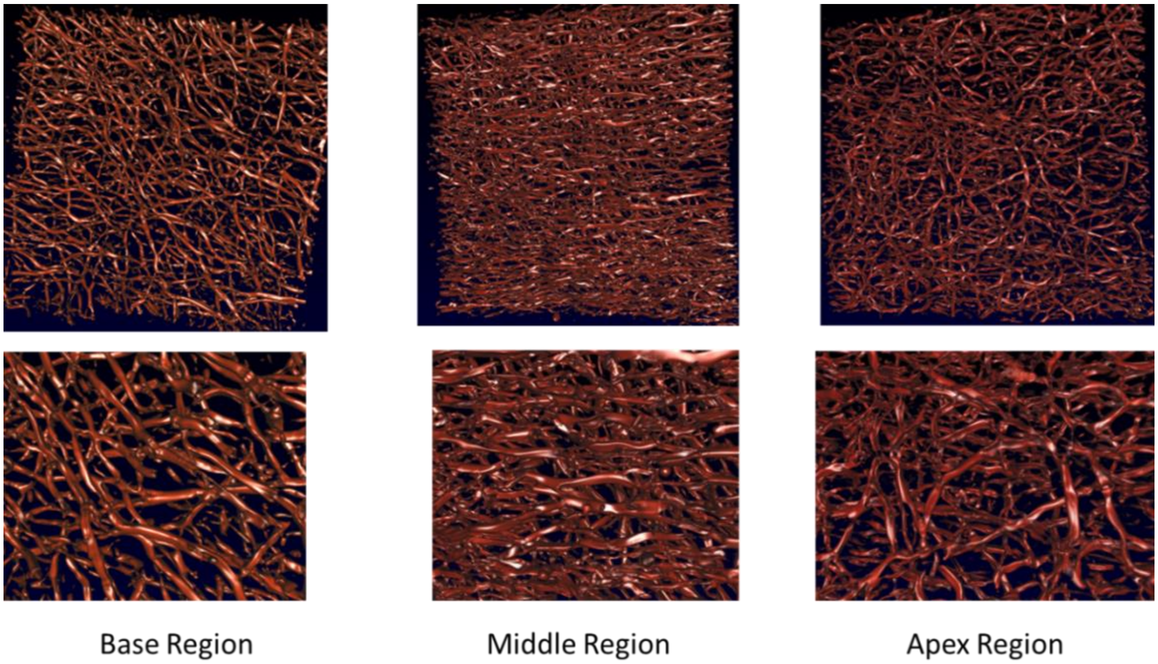

Figure 3.1 The 3D rendering of elastin fibers of the base, middle, and apex regions. Note: The bottom row images are magnified views of the top row images.

3.3.2 Fiber Skeletonization

We used the homotopic thinning algorithm (Lee et al., 1994) to produce a one-voxel-thick centerline skeleton for the elastin fibers. Additional to remove spurious fiber branches was also carried out. A multi-scale approach was applied to remove these spurious fiber branches. Smaller spurious branches disappeared on a higher scale image. Figure 3.2 shows the skeletonized centerlines of the fibers shown in Figure 3.1.

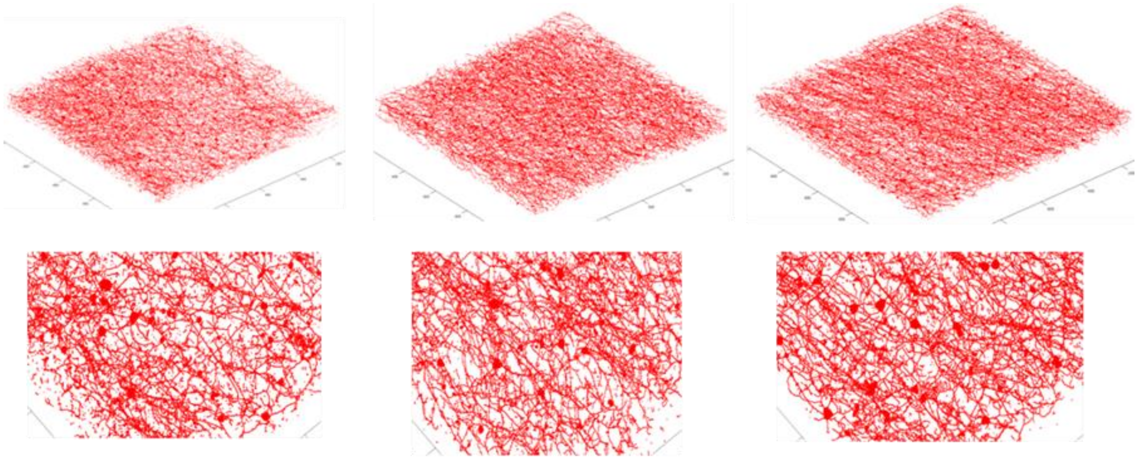

Base Region Middle Region Apex Region

Figure 3.2 The skeletonization of the elastin fibers of the base, middle, and apex regions.

Note: The density and complexity of the fibers suggest that a rich amount of information can be mined from a 3D topological and geometrical study.

3.3.3 Network Reconstruction

From the skeleton built in Figure 3.2, a network structure was further built by (i) removing the spurious fibers using length threshold, (ii) identifying nodes which connect two or more fibers, (iii) identifying links between a pair of nodes and terminal links where at least one of its end nodes has only one fiber connecting to it, and (iv) generating 3D orientation and distribution of the elastin fiber network. The result is shown in Figure 3.3. This network structure is necessary for our topological study. Topological analysis shows the distribution of cordless cycles in the network. Red, green, blue, magenta, and yellow fibers are part of the cordless cycles with 3 to 7 edges, respectively.

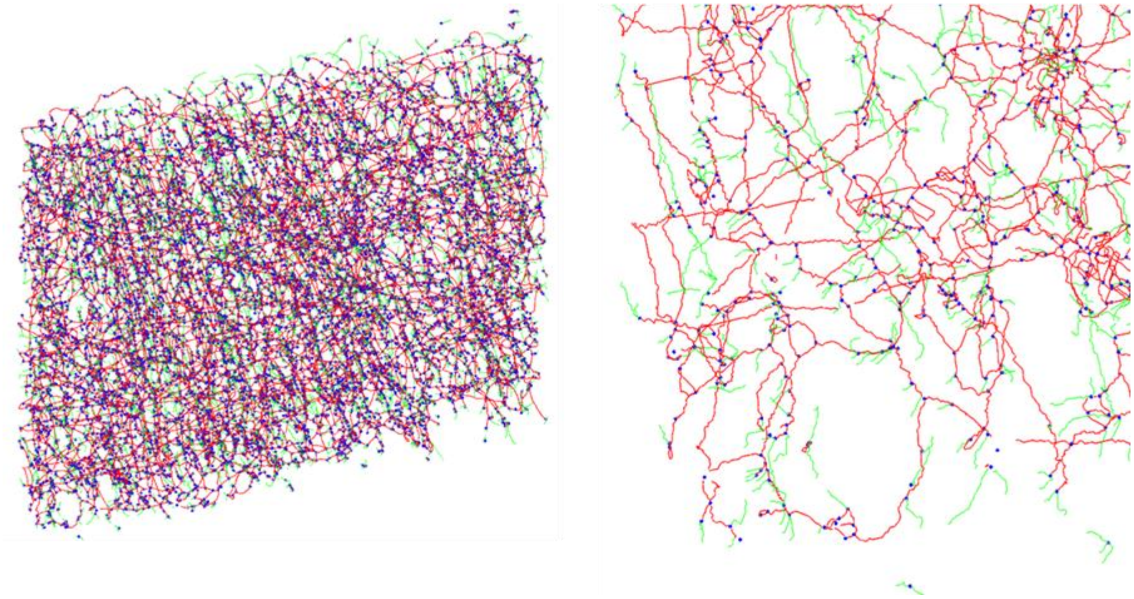

Figure 3.3 Images show the 3D elastin network structure in the apex region.

Note: The entire data set (left) and a zoomed in view (right). Nodes are represented by the blue dots. Internal links are colored red while external links are colored green.

3.3.4 3D Orientation and Distribution of Elastin fiber Network

Based on the reconstructed elastin fiber network, we were able to calculate the 3D orientation and distribution of the network (Figure 3.4). The top panel is the exemplified top views of the orientation and distribution of elastin fiber networks for the base region (A), middle region (B), and the apex region (C). The bottom panel is the side views for the same anatomical locations. Figure 3.4 shows that 3D orientation and distribution of the elastin fiber network demonstrate anatomical location-dependency.

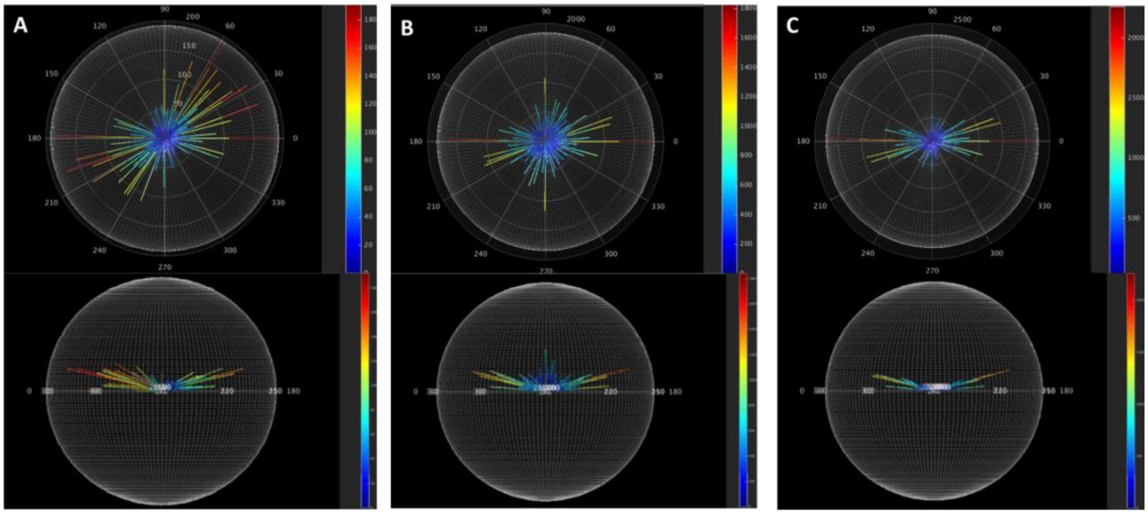

Base Region **Middle Region** **Apex Region**

Figure 3.4 Images show the 3D orientation and distribution of elastin fibers in the base, middle, and apex regions.

Note: Top panel: top views of the 3D orientation and distribution of the elastin fiber network. Bottom panel: side views of the 3D orientation and distribution of the elastin fiber network.

3.4 Discussion

In this study, fiber-based metrics reconstruction from the epicardial elastin network was achieved for the first time. Fiber-based biometrics is more specific and more robust to the disturbance to fiber locations across subjects. This fiberness map can be rendered for display or used as mask for further processing. The density and complexity of the fibers suggest that a rich amount of information can be mined from a 3D topological and geometrical study, which are highly correlated to their anatomical locations. The cycle structure can help reveal the biological design of the elastin fibers. Other than the metrics we obtained in this chapter, further potential metrics include fiber length, average fiber curvature, average scale along fiber in the network. The resulting abstract elastin network model can bring the study of cardiac elastin to a new level, and will have a broader impact to elastin network studies in other types of soft tissues.

CHAPTER IV

DEMONSTRATE THE EXISTENCE OF THE REGIONAL RESIDUAL STRESS OF THE EPICARDIAL ELASTIN IN THE LEFT VENTRICLE SURFACE VIA A NOVEL SURFACE CURLING ANGLE CHARACTERIZATION

4.1 Introduction

Investigations on heart failure have implied that congestive heart failure often results from diastolic dysfunction, which is defined as a mechanical abnormality that occurs during diastole (Zile & Brutsaert, 2002). The diastolic mechanics of the left ventricle (LV) have hence been broadly investigated (Arts, Veenstra, & Reneman, 1982; Humphrey, Strumpf, & Yin, 1990; Humphrey, Strumpf, & Yin, 1992; Kang, Humphrey, & Yin, 1996; Kang & Yin, 1996; McCulloch, Smaill, & Hunter, 1989). It is well known that heart muscle fibers in the myocardium have a fiber direction field, i.e., multilayered helical orientations (Zhang et al., 2010). During the systolic phase and diastolic phase, the cardiomyocytes (heart muscle cells) act along the fiber direction fields collectively in an anisotropically elastic manner to pressurize and relax the left ventricle as needed (Chadwick, 1982). Active relaxation of the cardiomyocytes and passive stiffness of the cardiac ECM are considered two factors to determine the properties of LV wall and the diastolic function (Zile & Brutsaert, 2002). As we summarized in Chapter 1, LV wall has three anatomically distinguishable layers, the epicardial layer, myocardial layer, and endocardial layer. The biomechanical properties of the myocardial layer have been extensively studied (Granzier & Irving, 1995; Kang et al., 1996; Kluge & Hovig, 1967). These studies have shown that heart muscle fibers interacted with myocardial ECM to realize the active contraction and passive dilation in a most effective and efficient manner. The myocardial ECM binds heart muscle fibers together, enables the overall architecture of multilayered helical orientation, provides tethering among muscle fibers, and prevents the over-stretch of muscle fibers during LV dilation (Chadwick, 1982). However, the mechanical properties and the impact of epicardial layer to the LV during diastole are largely ignored.

During our dissection of tissue samples from the heart surface, which were ~ 1.5 mm thick, we noticed an interesting phenomenon that has not been reported before, i.e., the bi-layered LV surface strip always curls towards the epicardium side. We pondered in this interesting behavior, and more dissections verified its repeatability. This surface curling clearly reveals that there is large surface stress existing in the epicardial layer. In other words, the rich elastin network in the epicardial layer is under tension when the epicardial layer covers the intact heart and is in its *in situ* 3D configuration. However, after a strip being dissected off the heart, the boundary condition that restricts the elastin network from contraction does not exist anymore. As a result, the contraction of epicardial layer bends the tissue strip and a curling morphology occurs. This interesting phenomenon points out the possible existence of residual stress in the epicardial layer.

According to Y. Fung (1991), residual stress in an organ is the stress that remains in tissue after all external loads are removed. A well-known example is the residual stress and strain in blood vessels. After the blood vessel is cut into ring segments, a single radial cut releases the residual stress in the blood vessel wall. The closed ring configuration cannot be maintained, and the ring opens, forming an arc confirmation. Y. Fung (1991) defined the opening angle as the angle formed between two lines extending from the tips of the opened ring to the midpoint of the inner arc of the opened ring.

The concepts of residual stress and residual strain have also been applied to the rat left ventricular wall. Omens and Fung (1990) showed that, if a radial cut is applied on an equatorial slice of a rat heart, the rat ventricle has an opening angle-like morphology (~30°), indicating residual stress existing in the whole ventricular wall. Jöbsis et al. (2007) performed a similar study on the residual stress of rat left ventricle by examining the gross opening angle of porcine left ventricle wall. They showed that peeling-off or disruption of the epicardium reduces the gross opening angle of the left ventricular wall, implying the likely contribution of the epicardium to the ventricular residual stress.

The curling of the LV surface strip provides us a more sensitive characterization of the possibly residual stress of the epicardial layer. As we pointed out in Chapter 2, elastin fiber microstructure, alignment, and distribution in the epicardial layer have both anatomical location-dependency and depth-dependency. We hence intended to use the heart surface strip curling as a mean to reveal and characterize the residual stress of the epicardial layer (effect of cardiac elastin in essence). We planned to measure the surface curling angle of the dissected porcine epicardial strips along both circumferential and longitudinal directions. 10% buffered formalin solution fixed whole porcine hearts were also used to record original curvatures of the heart surface as a reference. The formalin fixation "froze" the heart geometry and allowed us to have the baseline to calculate how much angular change experienced by the dissected surface strip due to curling.

4.2 Materials and Methods

4.2.1 Sample Preparation

Fresh porcine hearts (~ 6-month old) were obtained from a local abattoir and transported to the laboratory. Both circumferential and longitudinal LV surface strip samples were collected. Native epicardial strips (~ 15 mm × 5 mm × 1.5 mm) were dissected out from seven locations from three regions of the LV (three from the base, three from the middle, and one from the apex point) (Figure 4.1).

To use natural curvature of heart as a reference, as well as to validate that the curling is from the contraction of epicardial layer, intact native hearts were fixed in 10% buffered formalin solution for 72 hours, rinsed in PBS for 1 day. Formalin-fixed LV surface strips were then dissected out using the same dimension as native epicardial strips (~ 15 mm × 5 mm × 1.5 mm). Each group N = 5.

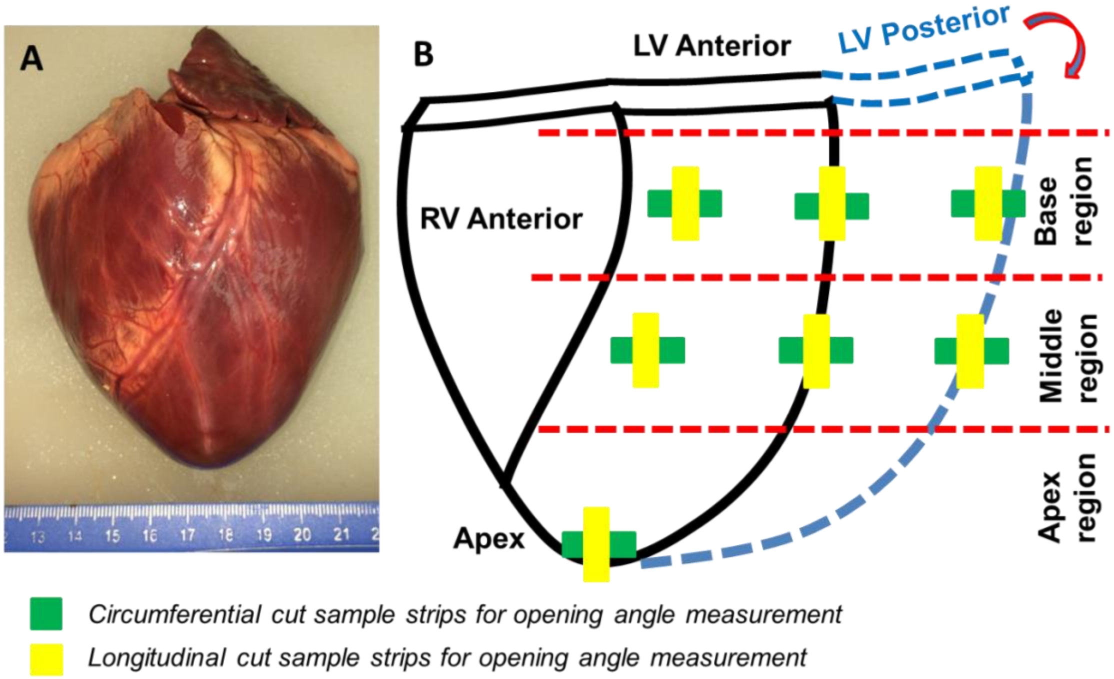

Figure 4.1 Schematic illustration of sample preparation plan.

4.2.2 Surface Curling Angle Measurement

After dissection, each LV tissue strip was immersed in 1X PBS in petri-dish to create a free floating and stress-free status. Note that the free floating of LV tissue strip could reduce the friction of petri-dish bottom to minimum and the stress-free status could hence be obtained. Digital pictures of each strip (side view) were taken right after the full occurrence of curling, i.e., the curvature of each tissue strip experienced no more change and stayed stable. LV tissue strips dissected from formalin-fixed hearts were imaged in the same way as the native LV tissue strips.

ImageJ (NIH, Bethesda, MD) was used to analyze the curly-enclosed angle. Step 1: outline the side view of the epicardial surface and measure its length. Step 2: use half length of the curve measured in step 1 to find and mark the midpoint. Step 3: draw straight lines connecting the two ending points of the strip to the midpoint and measure the curly-enclosed angle (Figure 4.2).

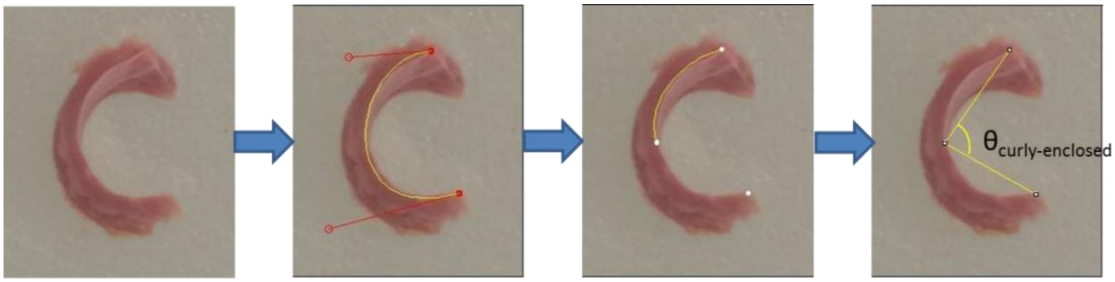

Free-floating strip in PBS bath **Step 1** **Step 2** **Step 3**

Figure 4.2 Illustration of the surface curly-enclosed angle measurement.

In order to estimate the total curling angular change of each LV tissue strip related to the natural curvature of the heart, four types of angles were defined: $\theta_{\text{curly-enclosed}}$ as the surface curly-enclosed angle from native LV strips after being dissected out and reaching a stable curling status (Figure 4.3, method in Figure 4.2); θ_{natural} as the angle defined by the natural curvature contour measured from the formalin-fixed tissue strip, i.e., the angle enclosed by the two lines that link the two ending points to the midpoint of the surface curve (Figure 4.3); θ_{reflex} represents the reflex angle of $\theta_{\text{curly-enclosed}}$ defined by equation 4.1 (Figure 4.3); and θ_{Δ} is the total curling angular change defined by Equation 4.2 (Figure 4.3).

$$\theta_{reflex} = 360° - \theta_{curly-enclosed} \tag{4.1}$$

$$\theta_{\Delta} = \theta_{\Delta 1} + \theta_{\Delta 2} = \theta_{reflex} - \theta_{natural} \tag{4.2}$$

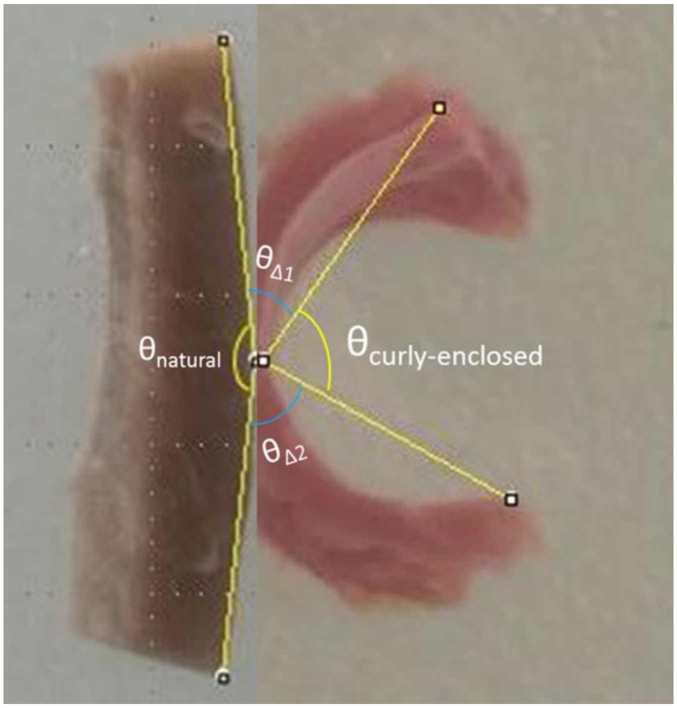

Figure 4.3 Schematic illustration shows four defined angles and the calculation of total curling angular change.

4.3 Results

Heart surface strips along the circumferential direction and longitudinal direction (Figures 4.4 and 4.6) were assessed in both native status (Panel A) and 10% buffered formalin solution fixed status (Panel B). Our first observation was that the heart surface strips showed various degrees of curling in all the anatomical locations we examined. Quantification results were shown in Figure 4.5 for circumferential direction and Figure 4.7 for longitudinal direction for all the anatomical locations, with Panel A showing the curly-enclosed angle ($\theta_{\text{curly-enclosed}}$), Panel B showing the natural angle (θ_{natural}), Panel C showing the reflex angle (θ_{reflex}), and Panel D showing the total angular change due to curling (θ_{Δ}).

4.3.1 Natural Angle ($\theta_{natural}$)

As shown in Figures 4.4-A and 4.6-A, 10% buffered formalin solution was able to preserve the natural curvature of the intact heart even after the surface strips were dissected from the intact heart. For surface strips dissected along both the circumferential direction and longitudinal direction, natural angles ($\theta_{natural}$) fell into the range between 140° – 180° (Figures 4.5-C and 4.7-C). Based on our definition, the smaller the natural angle ($\theta_{natural}$), the larger the curvature of the heart. From Figure 4.5-C, we noticed that for the circumferential direction, the basal lateral location (B2), middle lateral location (M2), and apex location had larger heart surface curvatures when compared to the basal anterior location (B1), basal posterior location (B3), middle anterior location (M1), and middle posterior location (M3) (Figure 4.5-C). As to the longitudinal direction, the apex region had obviously larger heart surface curvature and other anatomical locations had smaller curvatures (Figure 4.7-C).

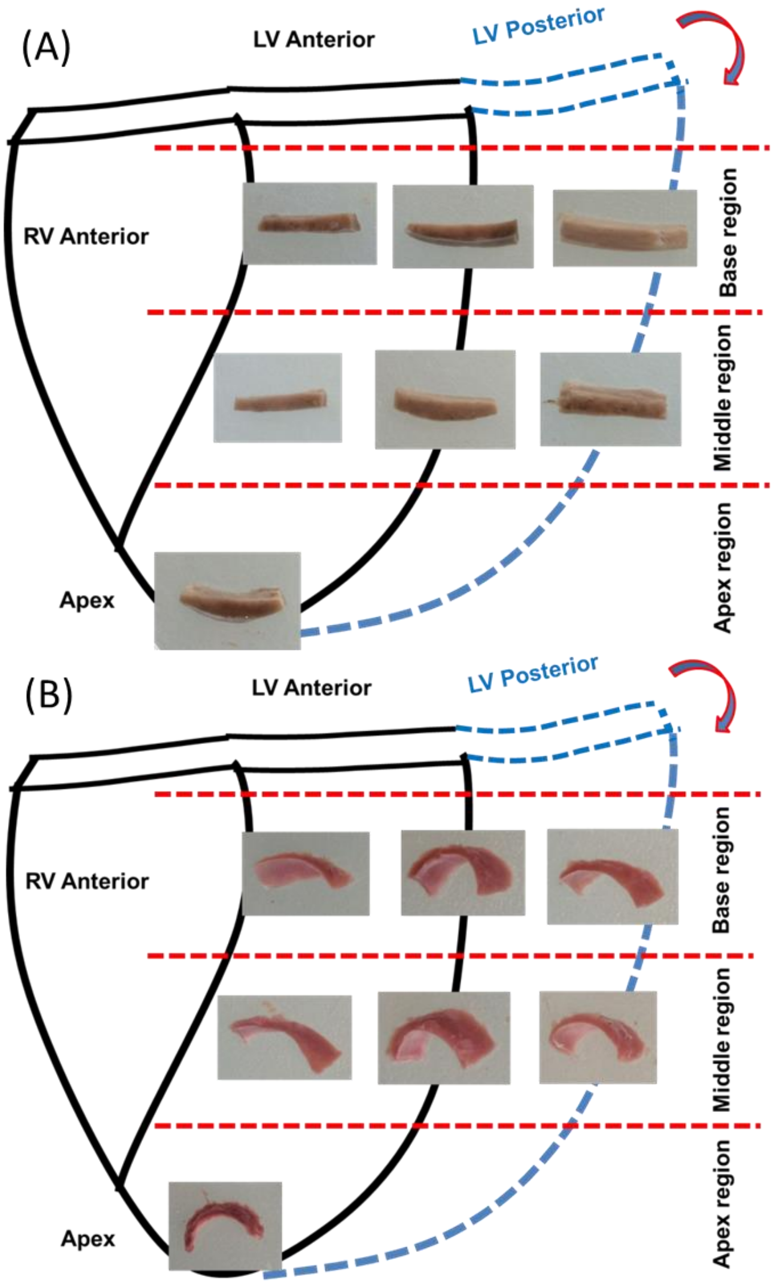

Figure 4.4 Representative epicardial surface strips curling along the circumferential direction. All seven anatomical locations of the left ventricle are shown.

Note: (A) Epicardial surface strips dissected from the 10% buffered formalin solution fixed intact heart; 10% buffered formalin solution was able to preserve the natural curvature of the intact heart. (B) Epicardial surface strips dissected from the native intact heart. Native epicardial surface strips show various degree of curling in different anatomical locations.

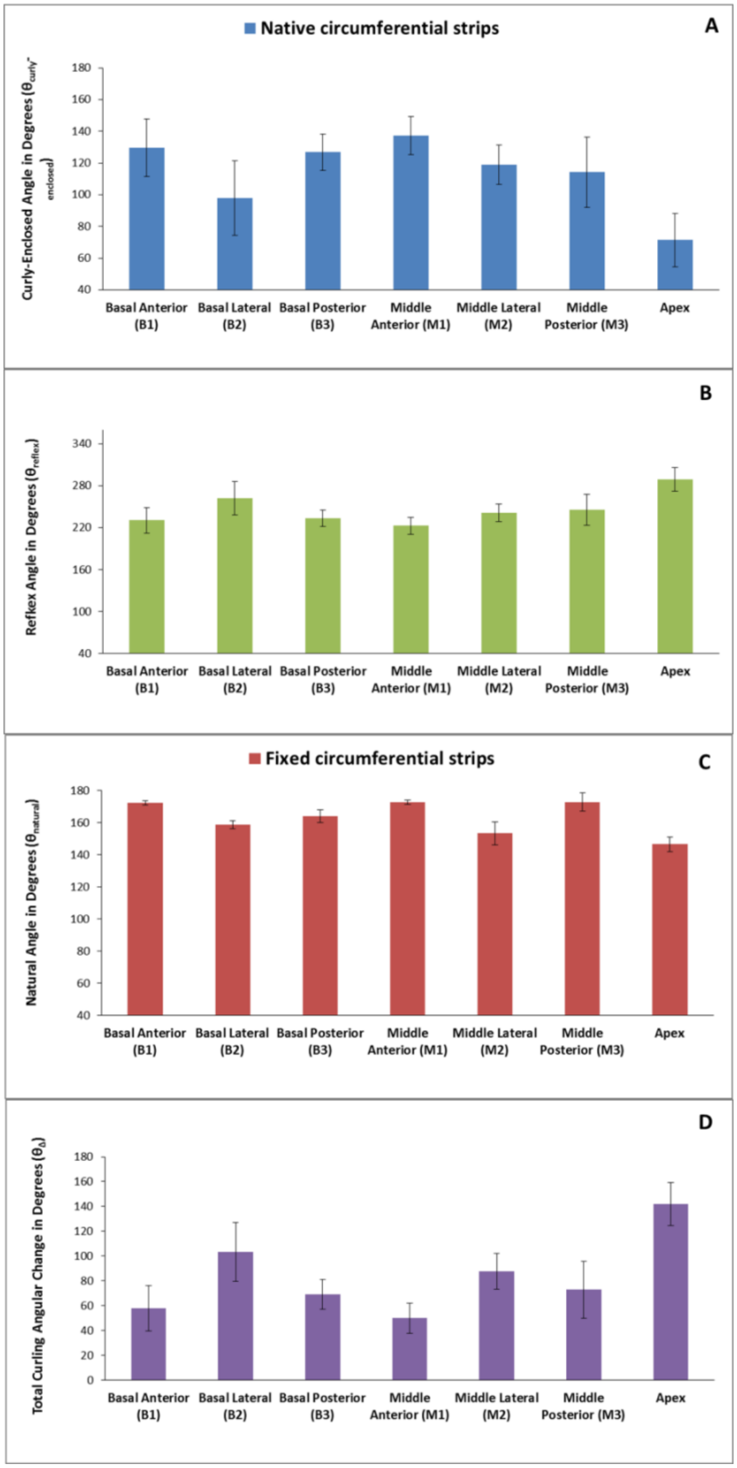

Figure 4.5 Measurements of four types of angles to quantify the epicardial surface strip curling (circumferentially-dissected).

Note: (A) Curly-enclosed angle ($\theta_{\text{curly-enclosed}}$) in degrees; (B) Reflex angle (θ_{reflex}) in degrees; (C) Natural angle (θ_{natural}) in degrees; and (D) Total curling angular change (θ_{Δ}) in degrees.

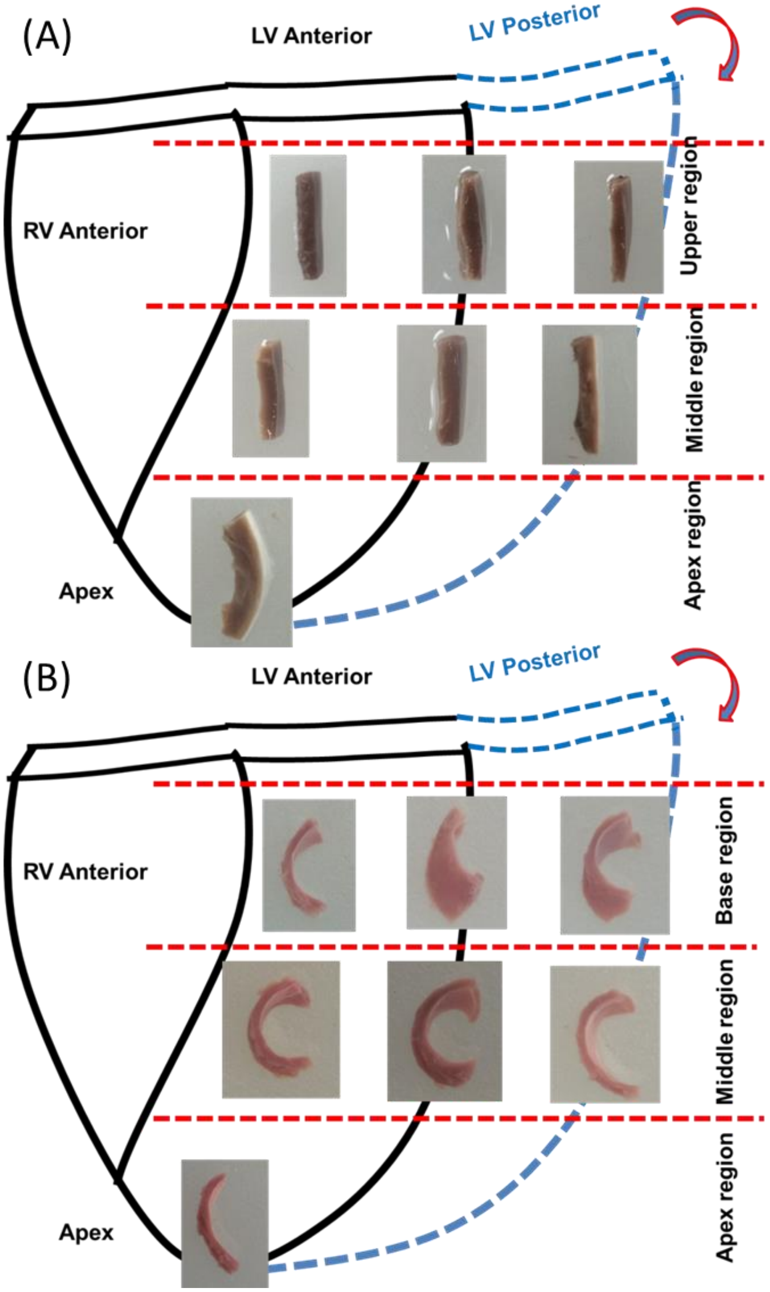

Figure 4.6 Representative epicardial surface strip curling along the longitudinal direction. All seven anatomical locations of the left ventricle are shown.

Note: (A) Epicardial surface strips dissected from the 10% buffered formalin solution fixed intact heart; 10% formalin solution was able to preserve the natural curvature of the intact heart. (B) Epicardial surface strips dissected from the native intact heart. Native epicardial surface strips show various degree of curling in different anatomical locations.

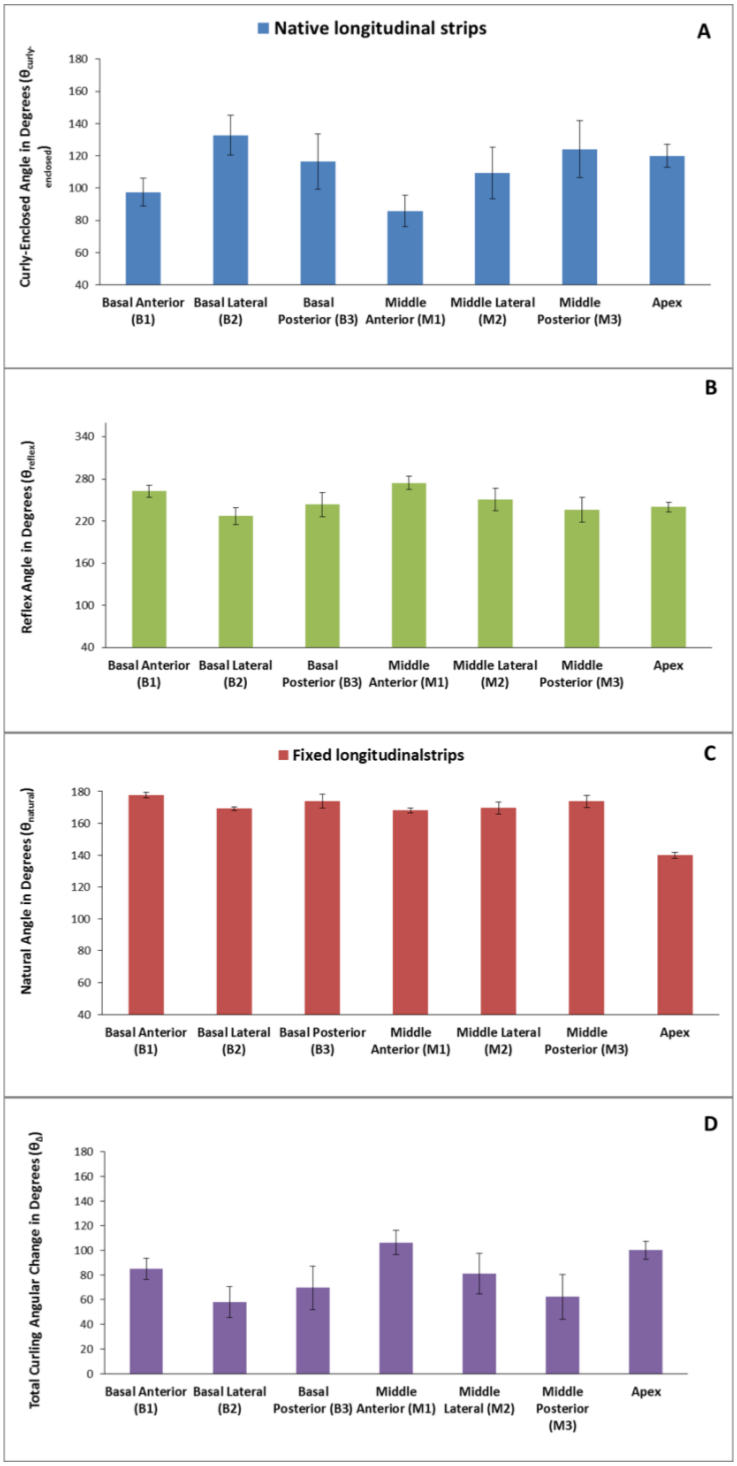

Figure 4.7 Measurements of four types of angles to quantify the epicardial surface strip curling (longitudinally-dissected).

Note: (A) Curly-enclosed angle ($\theta_{curly\text{-}enclosed}$) in degrees; (B) Reflex angle (θ_{reflex}) in degrees; (C) Natural angle ($\theta_{natural}$) in degrees; and (D) Total curling angular change (θ_{Δ}) in degrees.

Table 4.1 Data summary for four types of angles measurements. The goal is to quantify the total curling angle changes of the epicardial surface strips.

N = 5 (Unit: degree °)		$\theta_{\text{curly-enclosed}}$	θ_{natural}	θ_{Δ}
Basal Anterior (B1)	CD	129.62±18.11	172.42±1.35	59.97±18.16
	LD	97.43±8.58	117.62±1.73	84.95±8.75
Basal Lateral (B2)	CD	97.99±23.53	158.78±2.32	103.22±23.65
	LD	132.79±12.29	169.18±1.10	58.04±12.34
Basal Posterior (B3)	CD	126.74±11.38	164.12±4.13	69.14±12.11
	LD	116.43±17.22	173.92±4.44	69.64±17.78
Middle Anterior (M1)	CD	137.22±12.18	172.74±1.34	50.04±12.25
	LD	85.77±9.70	168.02±1.53	106.21±9.82
Middle Lateral (M2)	CD	118.99±12.50	153.44±7.18	87.57±14.42
	LD	109.33±15.94	169.53±3.86	81.15±16.40
Middle Posterior (M3)	CD	114.17±22.05	172.96±5.63	72.87±22.76
	LD	124.05±17.70	173.68±3.62	62.27±18.06
Apex	CD	71.34±16.92	146.66±4.45	142.00±17.50
	LD	120.01±7.14	139.86±2.03	100.13±7.42

Note: $\theta_{\text{curly-enclosed}}$ is the curly-enclosed angle, θ_{natural} is the natural angle, and θ_{Δ} is the total curling angular change. CD represents the circumferential direction, and LD represents the longitudinal direction.

4.3.2 Curly-Enclosed Angle ($\theta_{\text{curly-enclosed}}$) and Total Curling Angular Change (θ_{Δ})

Based on the definition of curly-enclosed angle ($\theta_{\text{curly-enclosed}}$, Figure 4.2), the smaller the curly-enclosed angle, the larger the reflective angle of $\theta_{\text{curly-enclosed}}$, and hence the larger the curling happens. Using natural angle (θ_{natural}) as the baseline, we were able to obtain the total curling angular change (θ_{Δ}) due to the surface strip curling (total curling angular change) after dissected off the heart (Figures 4.5-D and 4.7-D).

For the circumferential direction, the total curling angular change revealed that (i) the large curling happened in the basal lateral location (B2) (103.22±23.65°) when compared to the basal anterior location (B1) (59.97±18.16°) and basal posterior location (B3) (69.14±12.11°); (ii) the larger curling happened in the middle lateral location (M2) (87.57±14.42°) when compared to the middle anterior (M1) (50.04±12.25°) and middle posterior (M3) (72.87±22.76°); (iii) the circumferential curling is also very large in the apex location (142.00±17.50°) (Figure 4.5-D). What we can possibly derive from those angular change data due to curling is that the circumferential residual stress is larger in the lateral locations, i.e., (i) the circumferential residual stress in the basal lateral location (B2) is larger than the circumferential stresses of the basal anterior location (B1) and basal posterior location (B3); (ii) the circumferential residual stress in the middle lateral location (M2) is larger than the circumferential stresses of the middle anterior location (M1) and middle posterior location (M3) ; (iii) the circumferential residual stress is large in the apex location.

For the longitudinal direction, (i) the curling was larger in the basal anterior location (B1) (84.95±7.85°) when compared to the basal lateral location (B2) (58.04±16.40°) and basal posterior location (B3) (69.64±17.78°); (ii) the curling in the middle anterior location (M1) (106.21±9.82°) was larger than the middle lateral location (M2) (81.15±14.40°) and the middle posterior location (M3) (62.27±18.06°); (iii) the curling in the apex location was also large (100.13±7.42°) (Figure 4.7-D). Again, we can possibly conclude that, the longitudinal residual stress in the anterior locations is larger than the longitudinal stresses of the lateral and posterior locations. Moreover, the longitudinal residual stress in the apex region is comparable to the longitudinal stresses of the anterior locations.

We can also possibly compare the strip orientation from the same anatomical location. For instance, we found that for the basal anterior location (B1), the circumferential total curling angular change (57.97±18.16°) was smaller than the longitudinal total curling angular change (84.95±8,75°), likely indicating that, in the basal anterior location (B1), the circumferential residual stress is smaller than the longitudinal residual stress. The same conclusion, i.e., the circumferential residual stress is smaller than the longitudinal residual stress, can likely be reached for the middle anterior location (M1) (total curling angular change: circumferential (50.04±12.34°) vs. longitudinal (106.21±9.82°)). In both cases, the differences in total curling angular change between the circumferential and longitudinal directions were very large, and it is thus a bit safe to make the above conclusions. Similarly, we might be able to conclude that, in the apex location, the circumferential residual stress is larger than the longitudinal residual stress (total curling angular change: circumferential vs. longitudinal). However, caution should be taken when doing the comparison if the difference in total curling angular changes is small since this approach is not rigorously quantitative.

4.4 Discussion

As we just mentioned, this novel curling angle characterization on the heart surface strips provides an intuitive method to reveal the existence of residual stress in the epicardial layer on the intact heart left ventricle. By measuring the curly-enclosed angle ($\theta_{\text{curly-enclosed}}$) of the dissected native strips and the natural angle (θ_{natural}) reflecting the heart surface curvature, we were able to obtain the total angular change due to curling (θ_{Δ}). This total curling angular change (θ_{Δ}) gives us the semi-quantitative information about the degree of residual stress.

The reason we call this total curling angular change (θ_{Δ}) semi-quantitative is due to the challenge of dissection. We tried the best to make sample dimensions consistent to target ~ 15 mm × 5 mm × 1.5 mm; however, experimentalists all understand the challenge of soft tissue dissections, i.e., the dissected samples will have small variations in dimensions. As an example, for this study the sample thickness will likely affect the degree of curling. Even though the uncertainties caused by factors such as dissection and heart-to-heart variation will likely be averaged out by repetitive testings ($N = 5$), we would rather trust the comparison only if the difference in total curling angular change (θ_Δ) is large.

As to the selection of ~15 mm × 5 mm × 1.5 mm for curling angle study, we reach to those dimensions by two major reasons:

(i) Strip thickness is a crucial factor that determines optimal curling. We need a bi-layered structure with one side is the epicardial layer with rich elastin network and the other side is the myocardium. As a consequence, the contraction of the epicardial layer results in bending of the dissected native strip (curling). The ~ 1.5 mm thickness includes the epicardial layer (~ 200 μm) and a thin myocardial layer (~ 1300 μm) and gives the best curling behavior of the dissected native strip (Figure 4.8).

(ii) The ~ 15 mm × 5 mm dimension is also to provide the optimal curling, as well as help the tissue strip be able to “stand” in the 1X PBS solution to achieve the stress-free status, i.e., minimum friction from the bottom of the petri dish but not floating around and unstable. With a good “standing” configuration, the side view picture can be taken for the curly-enclosed angle quantification.

From some of the images of the curling trips shown in Figures 4.4 and 4.6, one can notice that the curling often accompanies with a degree of twisting. This twisting might be the result of elastin fibers orientation in that location. For instance, if the overall orientation of the elastin fibers has an angel with the rectangular strip, the curling might accompany with certain twisting due to the pulling of elastin contraction is not aligned with the long axis of the rectangular strip; a phenomenon might be worthy further investigation.

10% buffered formalin solution has a function to crosslink the collagen, elastin, and cells in tissue, fully fix the tissue, and preserve the morphology when subjected to fixation. We did find that the very strong cross-link diminished the molecular, fibrillar, cellular level mobility, and the whole strip was "fixed" stayed and maintained equilibrium of stress status. These formalin-fixed LV surface strips provided us an opportunity to measure the natural curvature of heart at different anatomical locations. With this natural curvature and the curly-enclosed angle of the native LV surface strips, we were able to estimate the total curling angular change due to the release of residual stress in the epicardial layer.

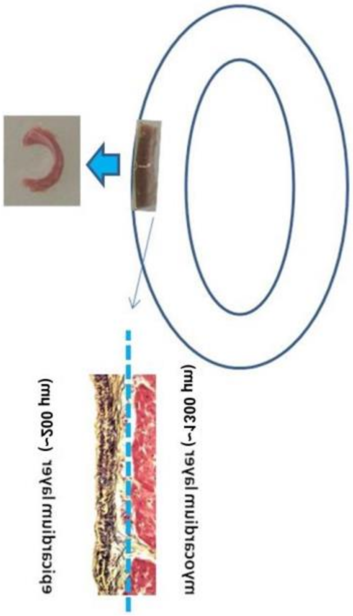

Figure 4.8 Schematic illustration showing the curling phenomenon of the epicardial surface strips dissected from the native intact heart.

CHAPTER V

QUANTIFY THE REGIONAL RESIDUAL STRESS IN THE EPICARDIAL LAYER OF THE LEFT VENTRICLE

5.1 Introduction

In Chapter IV, we carried out a curling angle study of tissue strips obtained from the left ventricular epicardial layer, which indicates the existence of residual stress on the heart surface. The curling angle study also points out the residual stresses from the base region to the apex region are certain location-dependent. However, the curling angle measurement by itself cannot provide accurate estimation of the residual stress. In this chapter, we developed a four-step methodology to estimate/calculate the regional residual stress of the epicardial layer on the left ventricle surface. The four steps are as follows:

(i) Quantify the residual strains existing on the epicardial layer. We first measured the *in situ* marker dimensions (4 markers) on the intact heart. After that, we dissected the marker labeled epicardial layer from the heart and measured the new marker dimensions (stress-released status). The residual strains along circumferential and longitudinal directions could thus be calculated.

(ii) The biomechanical behavior of the epicardial layers was quantified using a biaxial testing system to capture the tension-stretch (or stress-stretch) curves along the circumferential and longitudinal directions. The biaxial curves of various regions on the left ventricle were recorded. Note that biaxial testing all started from the 0.5g tare load.

(iii) Adjust the biaxial tension-stretch (stress-stretch) curves to the 0g load reference status. We compared the marker dimensions calculated from marker coordinates under the 0.5g tare load and under the 0g load. The amount of strain differences along both the circumferential and longitudinal directions were then compensated for the biaxial testing results to fix the curves starting from the 0g load.

(iv) For each location, residual stresses along the circumferential and longitudinal directions were then read from the adjusted biaxial curves by identifying the residual strains reported from step (i).

This is the first time that the residual stress of the epicardial layer on the left ventricle was quantitatively estimated. This will help us better understand the overall status of residual stress exerted by the LV epicardial layer.

5.2 Materials and Methods

5.2.1 Estimation of Residual Strain of the Epicardial Layer on the Intact Heart

A four-step estimation method was developed to quantify the regional residual strain of the LV epicardial layer on the intact heart. As we mentioned above, by putting four squarely-arranged markers on the epicardial surface of the intact heart, we could obtain the *in situ* marker dimensions while the residual strain existing. After dissecting the same region off the heart, the residual strain was found being released, and the isolated epicardial layer bore no stress. By putting the isolated epicardial layer into a petri-dish and immersing the sample in the 1X PBS, we obtained the new marker dimension of the epicardial layer under stress-free status. The residual strain of the epicardial layer along both the circumferential and longitudinal directions could thus be estimated.

Native juvenile porcine hearts were transported from a local abattoir to the laboratory. Seven epicardial layer sample locations (~ 10 mm × 10 mm × 1 mm) were chosen from the left ventricle (three from anterior, lateral, and posterior locations of the base region; three from anterior, lateral, and posterior locations of the middle region; one from the apex point) (Figure 5.1). Before dissection, four black markers were glued onto the surface of each sample location of the intact left ventricle using minimum amount of cyanoacrylate glue. A ruler with actual size was printed onto a paper. The paper ruler can be placed onto the left ventricle surface, perfectly fitting the left ventricle surface curvature. By this way, the readings of the real marker coordinates on the intact heart can be accurate, without being skewed by using a straight ruler for a curved surface. Digital pictures of each sample location (four markers along with the fitted paper rulers) were taken using a camera. After that, samples of each location were dissected out and immersed in 1X PBS in petri-dishes to make sure they were in the stress-free status. Rulers with actual size were printed on a straight transparent film and then placed along with the stress-free epicardial layer surface. Digital pictures of each stress-free sample (four markers along with the straight film rulers) were taken.

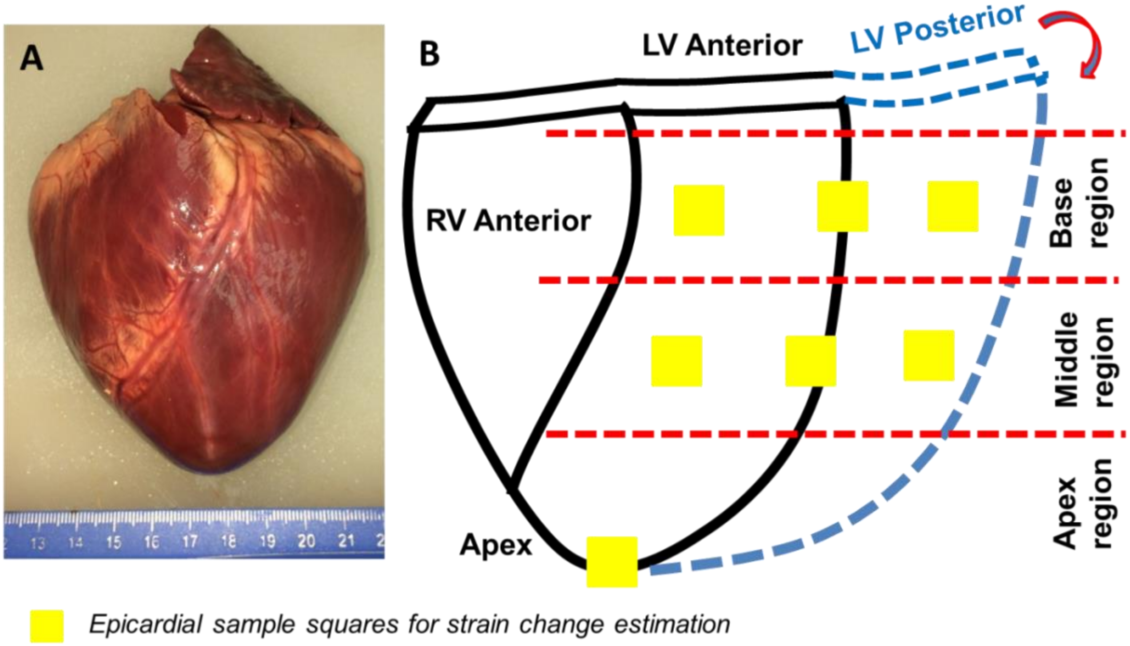

Figure 5.1 Schematic illustration of sample dissection plan for estimating residual strain of the epicardial layer on the intact left ventricle surface.

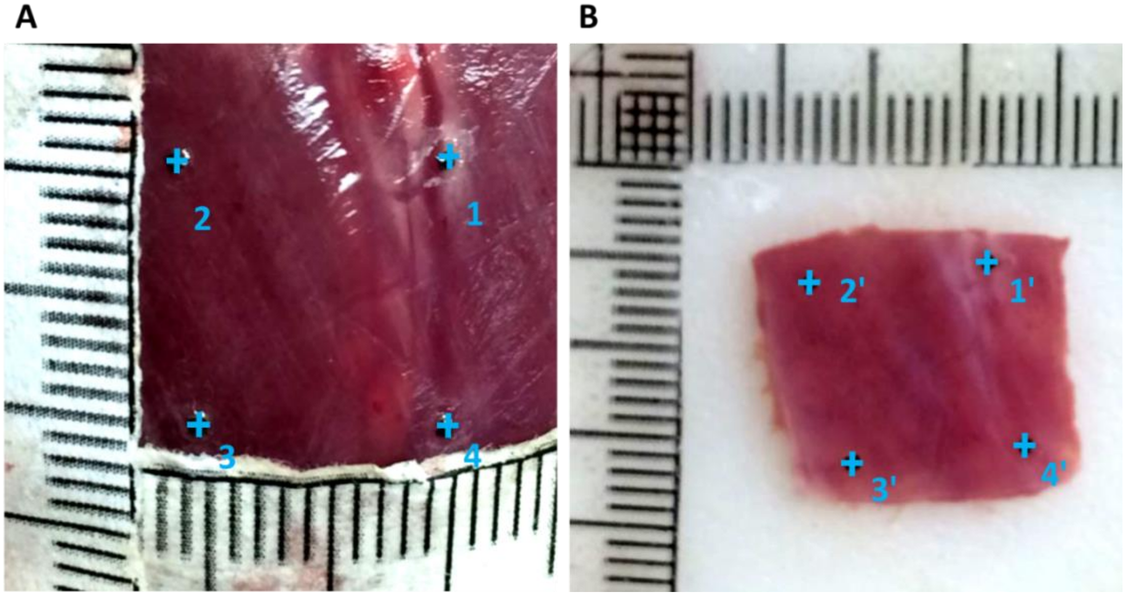

Figure 5.2 Markers tagged from ImageJ for both in situ sample (A) and stress-free sample (B).

Note: (A) 1 – 4 label markers for the *in situ* sample; (B) 1' – 4' label markers for the stress-free sample.

To calculate the residual strain, we first measured the x and y coordinates of each marker using ImageJ. For the markers on the heart surface, the coordinates were (x_1, y_1), (x_2, y_2), (x_3, y_3), and (x_4, y_4). For the markers on the stress-free samples, the coordinates were ($x_{1'}$, $y_{1'}$), ($x_{2'}$, $y_{2'}$), ($x_{3'}$, $y_{3'}$), and ($x_{4'}$, $y_{4'}$) (Figure 5.2). For each sample, we first converted the length in pixel to length in mm using each ruler. For the *in situ* samples, L_X and L_Y were calculated using Equations 5.1 and 5.2, respectively (Billiar & Sacks, 2000; Hoffman & Grigg, 1984). Note that Lx was the average of L_{X12} (marker distance between marker 1 and marker 2) and L_{X34} (marker distance between marker 3 and marker 4). L_Y was the average of L_{Y23} (marker distance between marker 2 and marker 3) and L_{Y14} (marker distance between marker 1 and marker 4). Similarly, from the stress-free samples, $L_{X'}$ and $L_{Y'}$ were calculated using Equations 5.3 and 5.4, respectively (Billiar &

Sacks, 2000; Hoffman & Grigg, 1984). Note that Lx’ was the average of Lx’$_{12}$ (marker distance between marker 1’ and marker 2’) and Lx’$_{34}$ (marker distance between marker 3’ and marker 4’). L$_{Y’}$ was the average of L$_{Y’23}$ (marker distance between marker 2’ and marker 3’) and L$_{Y’14}$ (marker distance between marker 1’ and marker 4’).

$$L_X = \frac{L_{X_{12}}+L_{X_{34}}}{2} = \frac{\sqrt{(x_1-x_2)^2+(y_1-y_2)^2}+\sqrt{(x_4-x_3)^2+(y_4-y_3)^2}}{2} \quad (5.1)$$

$$L_Y = \frac{L_{Y_{23}}+L_{Y_{14}}}{2} = \frac{\sqrt{(x_3-x_2)^2+(y_3-y_2)^2}+\sqrt{(x_4-x_1)^2+(y_4-y_1)^2}}{2} \quad (5.2)$$

$$L_{X\prime} = \frac{L_{X\prime_{12}}+L_{X\prime_{34}}}{2} = \frac{\sqrt{(x_1\prime-x_2\prime)^2+(y_1\prime-y_2\prime)^2}+\sqrt{(x_4\prime-x_3\prime)^2+(y_4\prime-y_3\prime)^2}}{2} \quad (5.3)$$

$$L_{Y\prime} = \frac{L_{Y\prime_{23}}+L_{Y\prime_{14}}}{2} = \frac{\sqrt{(x_3\prime-x_2\prime)^2+(y_3\prime-y_2\prime)^2}+\sqrt{(x_4\prime-x_1\prime)^2+(y_4\prime-y_1\prime)^2}}{2} \quad (5.4)$$

Estimated residual strains along the circumferential direction (ε_X) and longitudinal direction (ε_Y) were calculated by Equations 5.5 and 5.6, respectively.

$$\varepsilon_X = \frac{\Delta l}{l} = \frac{l_{X\prime}-l_X}{l_{X\prime}} = \frac{l_X}{l_{X\prime}} - 1 \quad (5.5)$$

$$\varepsilon_Y = \frac{\Delta l}{l} = \frac{l_{Y\prime}-l_Y}{l_{Y\prime}} = \frac{l_Y}{l_{Y\prime}} - 1 \quad (5.6)$$

5.2.2 Biaxial Mechanical Testing

Biaxial mechanical testing was performed to obtain the tissue mechanical behavior of the LV epicardial layer. In order to describe the possible location-dependency of the mechanical properties of the epicardial layer, we dissected square samples from the same anatomical locations, i.e., anterior, lateral, and posterior locations from the base region; anterior, lateral, and posterior locations from the middle region; and the apex point (for each location, N = 5). A custom made biaxial mechanical testing system was used to capture the tissue behavior under physiologically-relevant loading conditions. Biaxial testing is well known for its sensitivity to detect tension-stretch (stress-stretch) behavior alterations due to subtle tissue microstructural changes (Wang et al., 2010; Wang et al., 2012; Wang et al., 2013).

One axis of the square sample (~ 13 mm × 13 mm × 1 mm) was aligned with the circumferential direction (CD) of the heart and the other with the longitudinal direction (LD). Each side of the square sample was mounted onto four stainless steel hooks that are attached to two loops of 000 polyester sutures. Four fiducial graphite markers, affixed to the center of the square sample with cyanoacrylate adhesive, were monitored via a CCD camera to capture the real time stretch ratios. The sample was preconditioned biaxially by imposing 10 cycles of 60 N/m maximum Lagrangian membrane tension. After preconditioning, an equi-biaxial tension protocol of T_{CD}:T_{LD} = 60:60 N/m was performed to capture the biaxial behavior. All the testings were performed with a 0.5g tare load applied as a prerequisite for the software loading control protocol. The marker dimensions at 0.5g tare load were used as the reference status of biaxial mechanical testing.

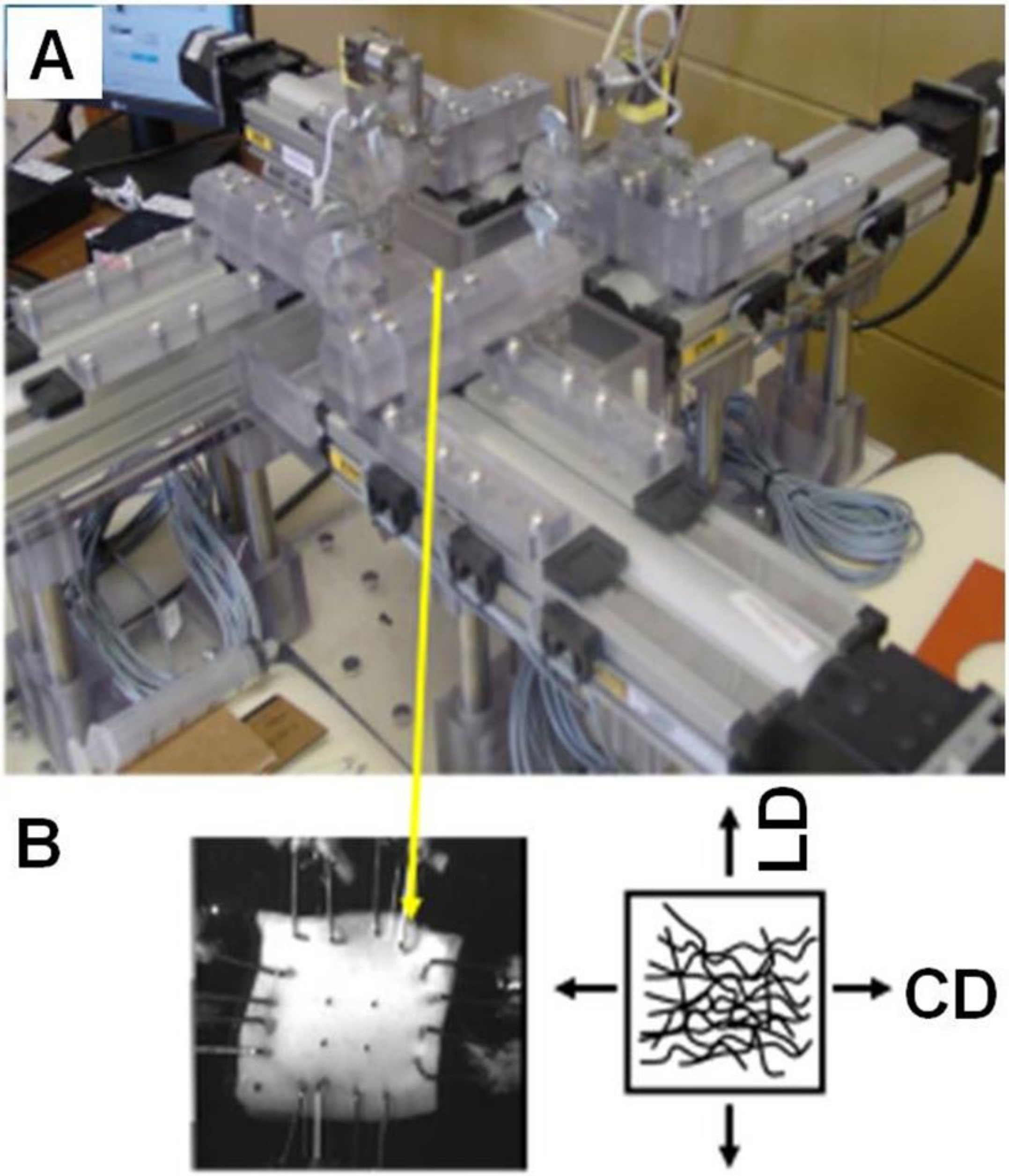

Figure 5.3 Biaxial mechanical testing system for soft tissues.

Note: (A) Biaxial mechanical testing system for soft tissues. (B) Left: sample picture shows how tissue being mounted; right: biaxial loading was applied along circumferential direction (CD) and longitudinal direction (LD) of the sample.

5.2.3 Adjust the Biaxial Curves to the 0g Load Reference Status

We compared the marker dimensions calculated from marker coordinates under the 0.5g tare load with marker dimensions under the 0g load. The amount of strain differences along both the circumferential and longitudinal directions were then compensated for the biaxial testing results to fix the curves starting from the 0g load.

As we just mentioned, during 60:60 N/m biaxial mechanical testing, a 0.5g tare load was applied to allow the software load control protocol. Therefore, it was necessary to adjust the biaxial curves to the real 0g load reference status, instead of using the dimensions at the 0.5g tare load as reference. Samples were obtained in the same way as described in the biaxial mechanical testing (section **5.2.2**). Each sample mounted onto the biaxial machine was first applied the 0.5g tare load, and the coordinates of four markers were saved as the 0.5g tare load reference files. The tare load was then released by adjusting the motor movement to 0g in both x (CD) and y (LD) directions. The tension releasing motor movement was stopped immediately once the load cell reading reported 0g. The marker positions of 0g load were consequently saved by the software as the 0g load reference files.

The compensatory strains of the 0.5g tare load status compared to 0g load status was then qualified using equations similar to Equations 5.1 – 5.4 (unit now all in pixels), as well as Equations 5.7 and 5.8. Briefly, ImageJ was first applied to obtain x and y coordinates for all markers. After calculating $l_{X(0.5)}$, $l_{Y(0.5)}$, $l_{X(0)}$, $l_{Y(0)}$ using marker coordinates and equations similar to Equations 5.1 – 5.4, the compensatory strains caused by the 0.5g tare load ($\varepsilon_{X(0.5)}$ and $\varepsilon_{Y(0.5)}$) were estimated by Equations 5.7 and 5.8.

$$\varepsilon_{X(0.5)} = \frac{\Delta l}{l} = \frac{l_{X(0.5)} - l_{X(0)}}{l_{X(0)}} = \frac{l_{X(0.5)}}{l_{X(0)}} - 1 \qquad (5.7)$$

$$\varepsilon_{Y(0.5)} = \frac{\Delta l}{l} = \frac{l_{Y(0.5)} - l_{Y(0)}}{l_{Y(0)}} = \frac{l_{Y(0.5)}}{l_{Y(0)}} - 1 \qquad (5.8)$$

For each location, the compensatory strains of the 0.5g tare load status vs. the 0g load status were averaged from three measurements. Schematic illustration in Figure 5.4 describes how the compensatory strains under the 0.5g tare load status were calculated. The compensatory strains, i.e., $\varepsilon_{X(0.5)}$ and $\varepsilon_{Y(0.5)}$ (Equations 5.7 and 5.8), were then used to adjust the biaxial tension-stretch (or stress-stretch) curves by adding those amount of strains ($\varepsilon_{X(0.5)}$ and $\varepsilon_{Y(0.5)}$) into each toe region correspondingly (curves hence shifting toward right). After the adjustment, the new curves started from the 0g load reference status.

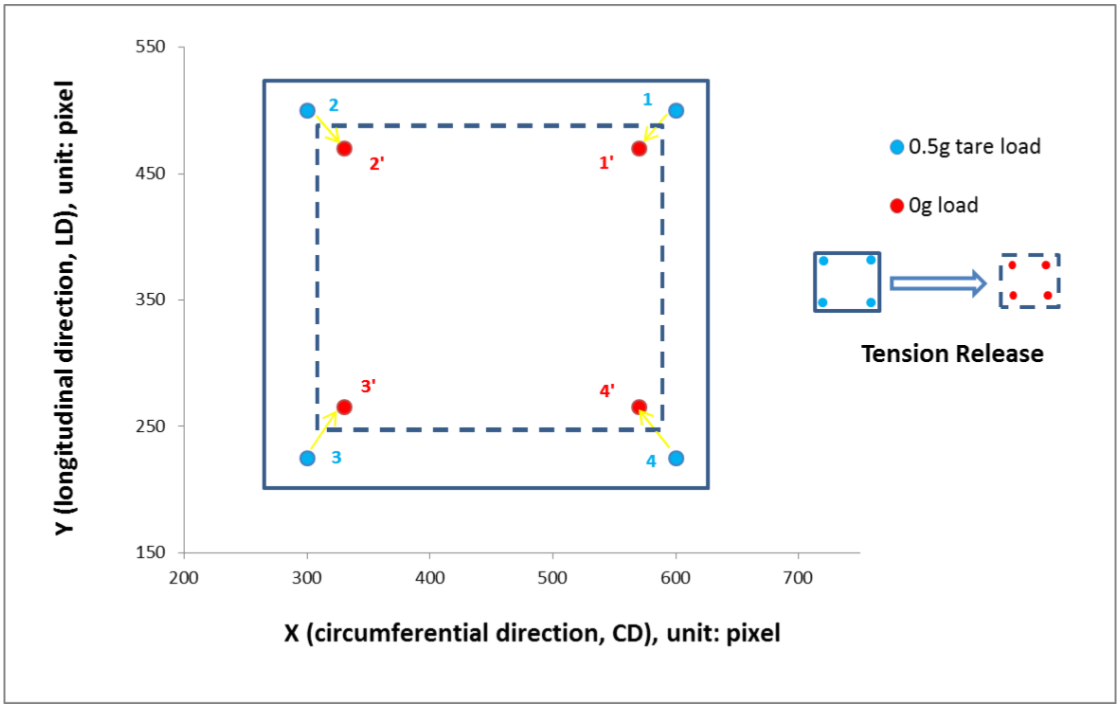

Figure 5.4 Schematic illustration shows how the compensatory strains under the 0.5g tare load status were calculated.

Note: Blue dots labeled 1 to 4 represent marker positions at the 0.5g tare load. Likewise, red dots 1’ to 4’ represent marker positions at the 0g load after tension released.

5.3 Results

5.3.1 Residual Strain of Epicardial Layer Estimated from *in situ* and Stress-Free Dimensions

The average estimated residual strains (ε_X and ε_Y) for each anatomical location are listed in Table 5.1. Several observations of Table 5.1 are summarized as follows:

(i) For nearly all the anatomical locations, except for the circumferential direction (ε_X) of basal anterior location (B1) and middle anterior location (M1), the residual strains of both the circumferential and longitudinal directions, ε_X and ε_Y, were positive.

(ii) For all other anatomical locations, except for the basal anterior location (B1) and middle anterior location (M1), ε_X and ε_Y were positive, and ε_X was slightly smaller than ε_Y.

Table 5.1 Residual strains estimated by comparing stress-free marker dimensions and *in situ* marker dimensions.

		Overall Average ± Standard Deviation
Basal Anterior (B1)	ε_X	-0.94 ± 4.1%
	ε_Y	7.76 ± 3.43%
Basal Lateral (B2)	ε_X	4.70 ± 1.41%
	ε_Y	6.02 ± 1.59%
Basal Posterior (B3)	ε_X	2.01 ± 4.35%
	ε_Y	4.94 ± 3.16%
Middle Anterior (M1)	ε_X	-3.90 ± 3.16%
	ε_Y	7.92 ± 6.35%
Middle Lateral (M2)	ε_X	6.26 ± 3.53%
	ε_Y	7.49 ± 2.40%
Middle Posterior (M3)	ε_X	3.99 ± 1.46%
	ε_Y	6.27 ± 2.13%
Apex	ε_X	5.02 ± 2.00%
	ε_Y	7.24 ± 3.71%

Note: Stress-free marker dimensions were used as reference to calculate the residual strains.

5.3.2 Biaxial Tension-Stretch Curves of Epicardial Layer (with 0.5g Tare Load)

The average dimensions of the epicardial layer samples for each anatomical location are shown in Table 5.2. The overall average dimensions of the epicardial sample were 13.33±0.30 mm in the circumferential direction (CD), 12.76±0.55 mm in the longitudinal direction (LD), and 1.01±0.069 mm in thickness (Table 5.2). We also ran two-tailed unpaired student t-tests with $\alpha=0.05$ for all seven anatomical locations between the CD and LD.

Table 5.2 Biaxial mechanical testing sample dimensions

N = 5 (Unit: mm)	CD	LD	Thickness
Basal Anterior (B1)	13.10±1.33	11.90±2.12	0.97±0.90
Basal Lateral (B2)	12.85±1.47	12.28±0.98	1.13±0.17
Basal Posterior (B3)	13.22±0.98	13.51±1.27	1.01±0.11
Middle Anterior (M1)	13.55±1.85	12.76±1.69	1.03±0.10
Middle Lateral (M2)	13.69±1.39	13.21±1.43	1.06±0.12
Middle Posterior (M3)	13.34±1.67	12.66±1.22	1.00±0.11
Apex	13.59±0.63	12.99±0.46	0.91±0.062
Overall Average ± Standard Deviation	13.33±0.30	12.76±0.55	1.01±0.069

Note: Table lists the length in CD, length in LD, and thickness (unit: mm) of the epicardial samples for each anatomical location.CD represents the circumferential direction, and LD represents the longitudinal direction.

Read from the biaxial tension-stretch curves, we observed the CD was stiffer than the LD in all seven anatomical locations. For the base region (Figure 5.5), under equibiaxial tension of 60:60 N/m, the maximum extensibilities of CD vs. LD were E_X = 5.71±2.01% vs. E_Y = 22.47±5.35%, E_X = 5.31±0.93% vs. E_Y = 19.94±1.39%, and E_X = 4.23±1.77% vs. E_Y = 21.91±4.22% for the basal anterior location (B1), basal lateral location (B2), and basal posterior location (B3). From the results of the two-tailed unpaired student t-test, all three locations of the base region showed significant differences between the CD and LD: (i) for the basal anterior location (B1) p-value = 3.01×10^{-5}; (ii) for the basal lateral location (B2) p-value = 5.20×10^{-8}; and (iii) for the basal posterior location (B3) p value = 2.50×10^{-5}. For the middle region (Figure 5.6), under equibiaxial tension of 60:60 N/m, the maximum extensibilities of CD vs. LD were E_X = 12.81.08±7.21% vs. E_Y = 20.95±4.46%, E_X = 9.74±3.05% vs. E_Y = 18.50±6.35%, and E_X = 9.11±3.92% vs. E_Y = 19.35±2.49% for middle anterior location (M1), middle lateral location (M2), and middle posterior location (M3). Two-tailed unpaired student t-tests showed that (i) the CD and LD had no significant difference for the middle anterior location (M1) (p-value = 0.17 > 0.05); (ii) there were significant differences for the middle lateral location (M2) (p-value = 0.024 < 0.05) and middle posterior location (M3) (p-value = 0.0012 < 0.05). For the apex region, under equibiaxial tension of 60:60 N/m, the maximum extensibilities of CD vs. LD were $E_X = 6.38 \pm 1.05\%$ vs. $E_Y = 17.23 \pm 2.82\%$, and there was significant difference (p-value = 0.00036 < 0.05) between CD and LD.

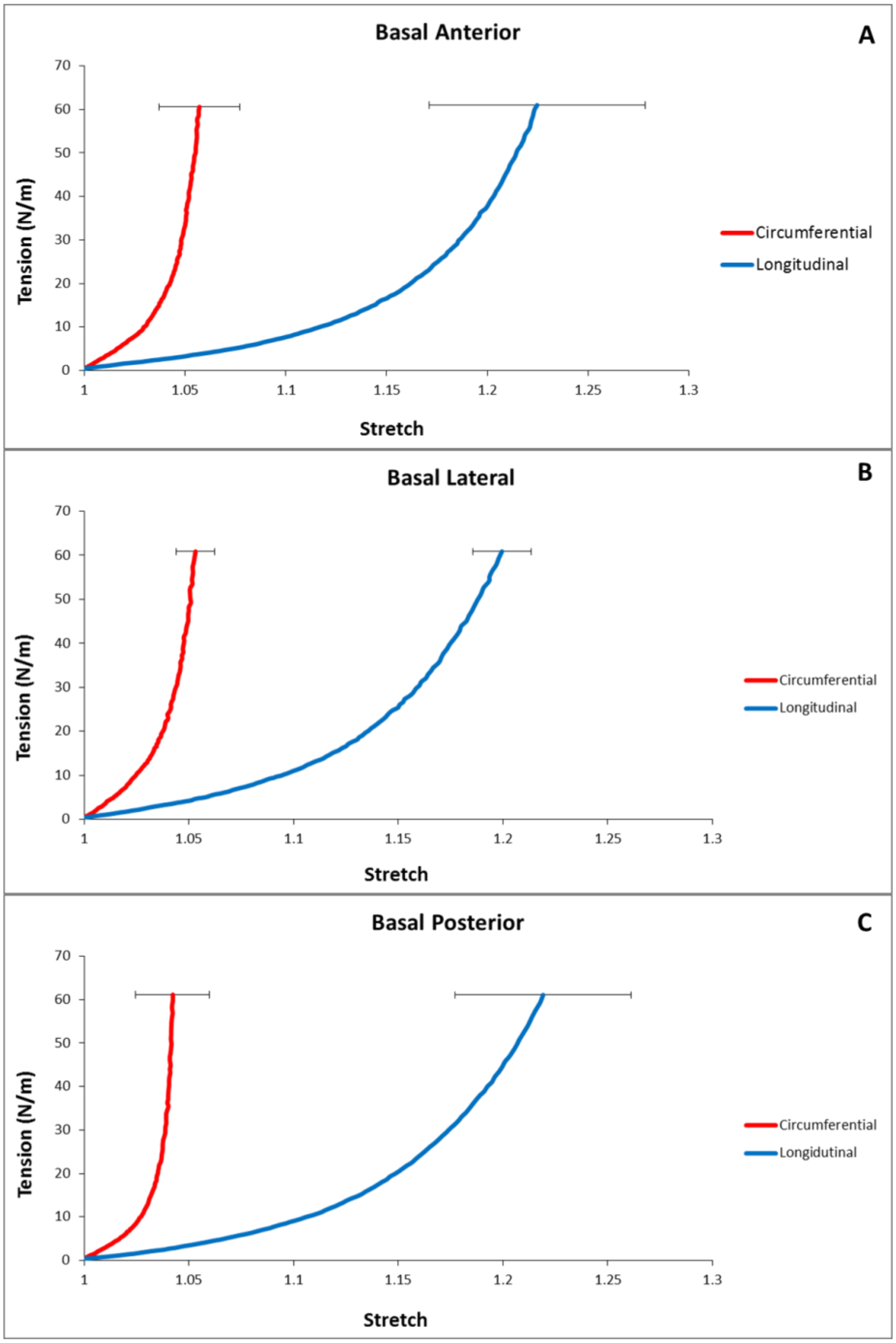

Figure 5.5 Biaxial tension-stretch curves for the epicardial layer samples harvested from the base region.

Note: Three locations in the base region were dissected from the (A) basal anterior; (B) basal lateral; and (C) basal posterior. The red curves represent the tension-stretch curves of the circumferential direction (CD); the blue curves represent the tension-stretch curves of the longitudinal direction (LD).

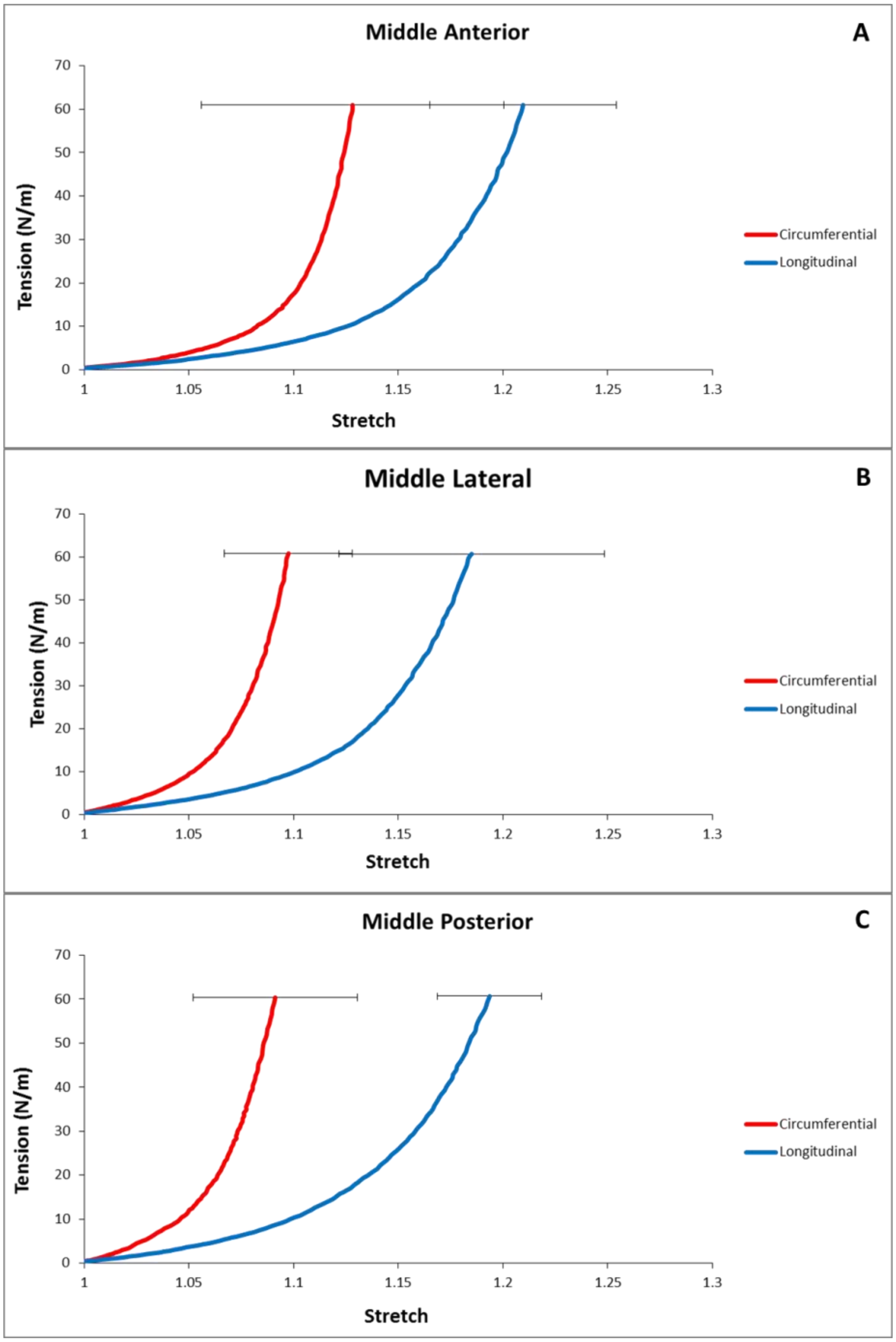

Figure 5.6 Biaxial tension-stretch curves for the epicardial layer samples harvested from the middle region.

Note: Three locations in the middle region were dissected from the (A) middle anterior; (B) middle lateral; and (C) middle posterior. The red curves represent the tension-stretch curves of the circumferential direction (CD); the blue curves represent the tension-stretch curves of the longitudinal direction (LD).

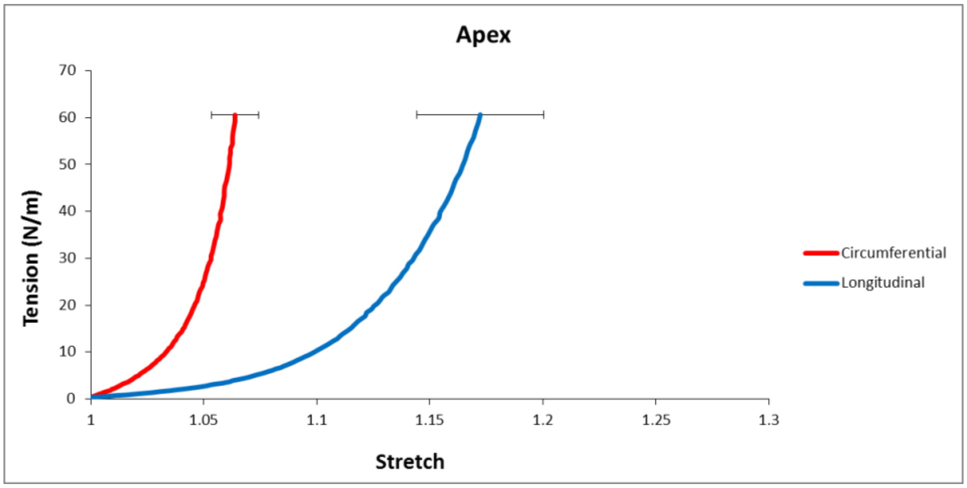

Figure 5.7 Biaxial tension-stretch curve for the epicardial layer samples harvested from the apex location.

Note: The red curve represents the tension-stretch curve of the circumferential direction (CD); the blue curve represents the tension-stretch curve of the longitudinal direction (LD).

5.3.3 Compensatory Strains of the 0.5g Tare Load with Respect to the 0g Load Reference

Table 5.3 lists (i) the marker dimensions ($L_{X(0.5)}$, $L_{Y(0.5)}$) calculated from the marker coordinates under the 0.5g tare load, (ii) the marker dimensions ($L_{X(0)}$, $L_{Y(0)}$) calculated from the marker coordinates under the 0g load, and (iii) the compensatory strains ($\varepsilon_{X\,(0.5)}$, $\varepsilon_{Y\,(0.5)}$) with respect to the 0g load reference, which were needed to adjust the biaxial tension-stretch curves. As we mentioned in Section **5.2.3**, the biaxial tension-stretch curves were obtained via the biaxial testing routine that required the 0.5g tare load for the software load control protocol.

Table 5.3 Average dimensions (in pixel) of epicardial sample squares and the compensatory strains by comparing between the 0.5g tare load and the 0g load in each anatomical location.

(Unit: pixel)	0.5g Tare Load		0g Load		Compensatory Strain	
Basal Anterior (B1)	$L_{X\,(0.5)}$	377.05	$L_{X\,(0)}$	371.04	$\varepsilon_{X\,(0.5)}$	1.62%
	$L_{Y\,(0.5)}$	220.42	$L_{Y\,(0)}$	213.52	$\varepsilon_{Y\,(0.5)}$	3.23%
Basal Lateral (B2)	$L_{X\,(0.5)}$	391.18	$L_{X\,(0)}$	385.85	$\varepsilon_{X\,(0.5)}$	1.38%
	$L_{Y\,(0.5)}$	258.02	$L_{Y\,(0)}$	256.33	$\varepsilon_{Y\,(0.5)}$	0.66%
Basal Posterior (B3)	$L_{X\,(0.5)}$	308.87	$L_{X\,(0)}$	304.44	$\varepsilon_{X\,(0.5)}$	1.46%
	$L_{Y\,(0.5)}$	226.14	$L_{Y\,(0)}$	223.91	$\varepsilon_{Y\,(0.5)}$	1.00%
Middle Anterior (M1)	$L_{X\,(0.5)}$	348.34	$L_{X\,(0)}$	345.36	$\varepsilon_{X\,(0.5)}$	0.87%
	$L_{Y\,(0.5)}$	235.73	$L_{Y\,(0)}$	232.57	$\varepsilon_{Y\,(0.5)}$	1.36%
Middle Lateral (M2)	$L_{X\,(0.5)}$	372.36	$L_{X\,(0)}$	368.15	$\varepsilon_{X\,(0.5)}$	1.14%
	$L_{Y\,(0.5)}$	269.09	$L_{Y\,(0)}$	265.49	$\varepsilon_{Y\,(0.5)}$	1.36%
Middle Posterior (M3)	$L_{X\,(0.5)}$	299.97	$L_{X\,(0)}$	287.77	$\varepsilon_{X\,(0.5)}$	3.25%
	$L_{Y\,(0.5)}$	261.07	$L_{Y\,(0)}$	258.55	$\varepsilon_{Y\,(0.5)}$	3.80%
Apex	$L_{X\,(0.5)}$	326.11	$L_{X\,(0)}$	319.47	$\varepsilon_{X\,(0.5)}$	2.08%
	$L_{Y\,(0.5)}$	257.84	$L_{Y\,(0)}$	248.92	$\varepsilon_{Y\,(0.5)}$	3.58%

5.3.4 Adjusted Biaxial Tension-Stretch Curves of Epicardial Layer (with the 0g Load Reference)

The compensatory strains ($\varepsilon_{X\,(0.5)}$, $\varepsilon_{Y\,(0.5)}$) with respect to the 0g load reference were used to shift the biaxial tension-stretch curves of the CD and LD directions accordingly (Figures 5.5 – 5.7). After the adjustment, we were able to re-plot the biaxial tension-stretch curves with the real 0g load reference (Figures 5.8 – 5.10).

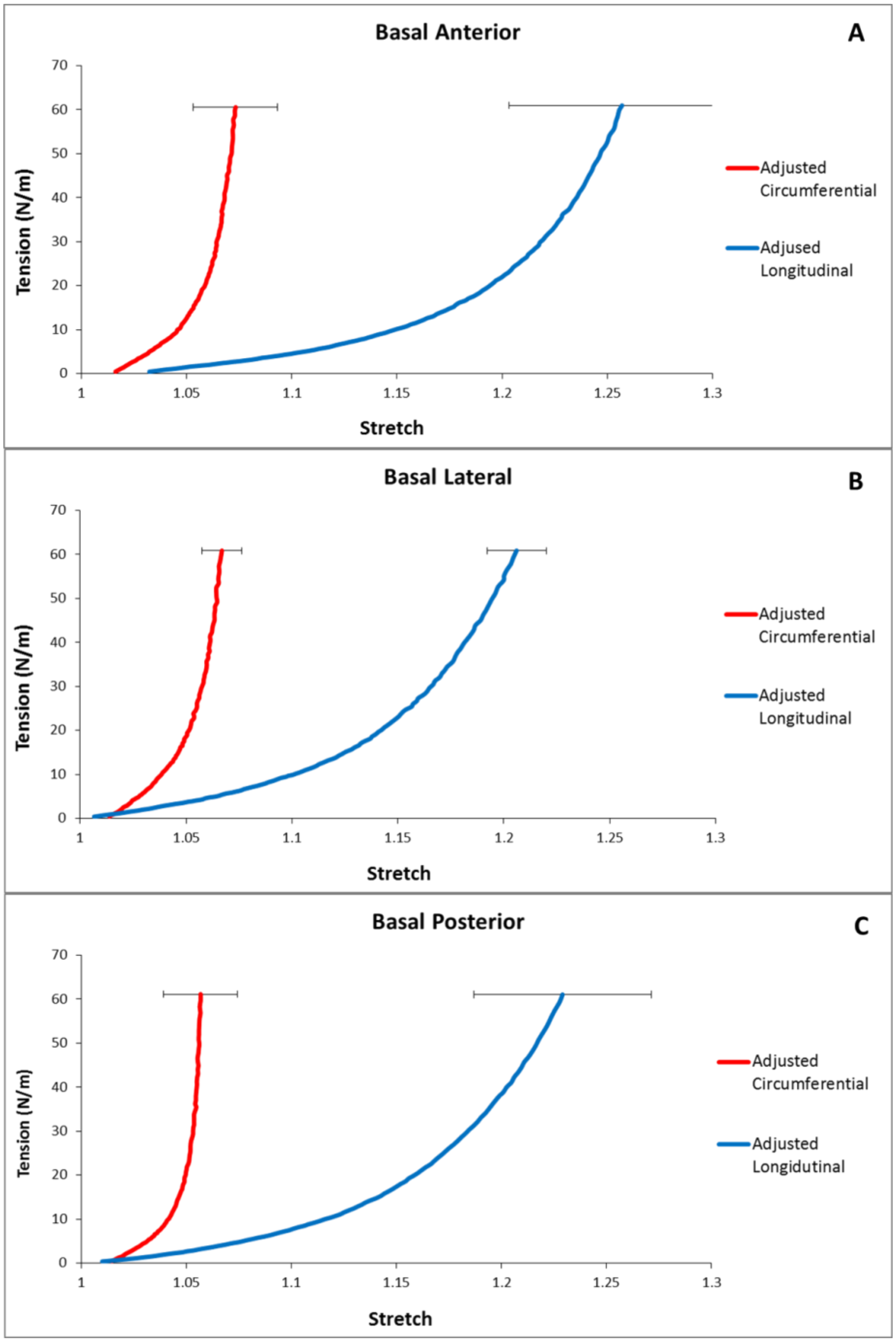

Figure 5.8 Adjusted biaxial tension-stretch curves for the epicardial layer samples harvested from the base region.

Note: Three locations in the base region were dissected from the (A) basal anterior; (B) basal lateral; and (C) basal posterior. The biaxial tension-stretch curves now start with the real 0g load reference. The red curves represent the tension-stretch curves of the circumferential direction (CD); the blue curves represent tension-stretch curves of the longitudinal direction (LD).

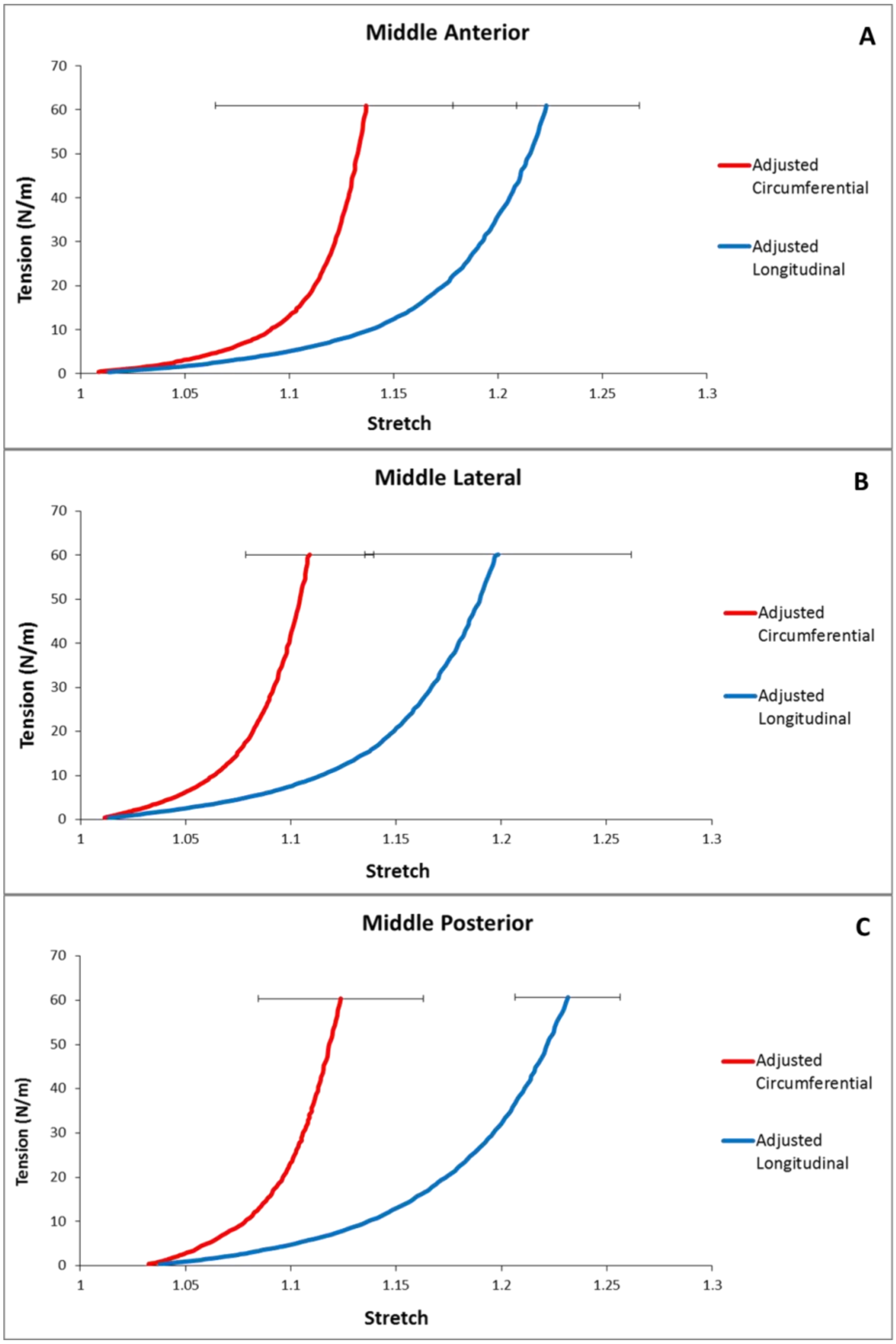

Figure 5.9 Adjusted biaxial tension-stretch curves for the epicardial layer samples harvested from the middle region.

Note: Three locations in the middle region were dissected from the (A) middle anterior; (B) middle lateral; and (C) middle posterior. The biaxial tension-stretch curves now start with the real 0g load reference. The red curves represent the tension-stretch curves of the circumferential direction (CD); the blue curves represent tension-stretch curves of the longitudinal direction (LD).

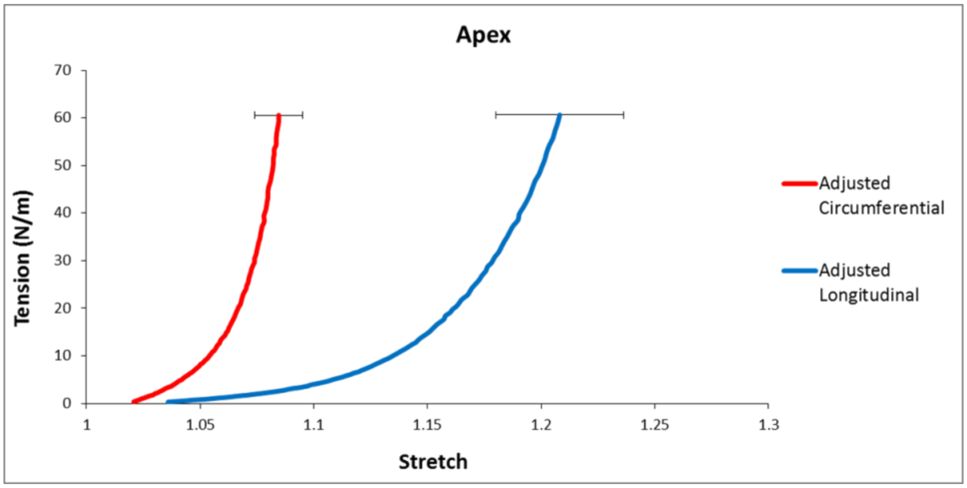

Figure 5.10 Adjusted biaxial tension-stretch curves for the epicardial layer samples harvested from the apex location.

Note: The biaxial tension-stretch curve now starts with the real 0g load reference. The red curve represents the tension-stretch curve of the circumferential direction (CD); the blue curve represents tension-stretch curve of the longitudinal direction (LD).

5.3.5 Estimation of the Residual Stresses along the CD and LD ($\sigma_{X(residual)}$, $\sigma_{Y(residual)}$) for Each Anatomical Location

With the thickness measurements of all the testing samples, we were able to plot the biaxial tension-stretch curves into biaxial stress-stretch curves. Figures 5.11 – 5.13 show the same biaxial curves of Figures 5.8 – 5.10 plotted in stress-stretch format. With the biaxial stress-stretch data (Figures 5.11 – 5.13) and the residual strain data (Table 5.1), we could estimate the residual stresses of both the CD and LD for each anatomical location. In Figures 5.11 – 5.13, red dash lines label the circumferential residual stresses ($\sigma_{X(residual)}$) predicted by the circumferential residual strains (ε_X), and blue dash lines label the longitudinal residual stresses ($\sigma_{Y(residual)}$) predicted by the longitudinal residual strains (ε_Y). The detailed numbers of $\varepsilon_X \rightarrow \sigma_{X(residual)}$ and $\varepsilon_Y \rightarrow \sigma_{Y(residual)}$ for each anatomical location are listed in Table 5.4.

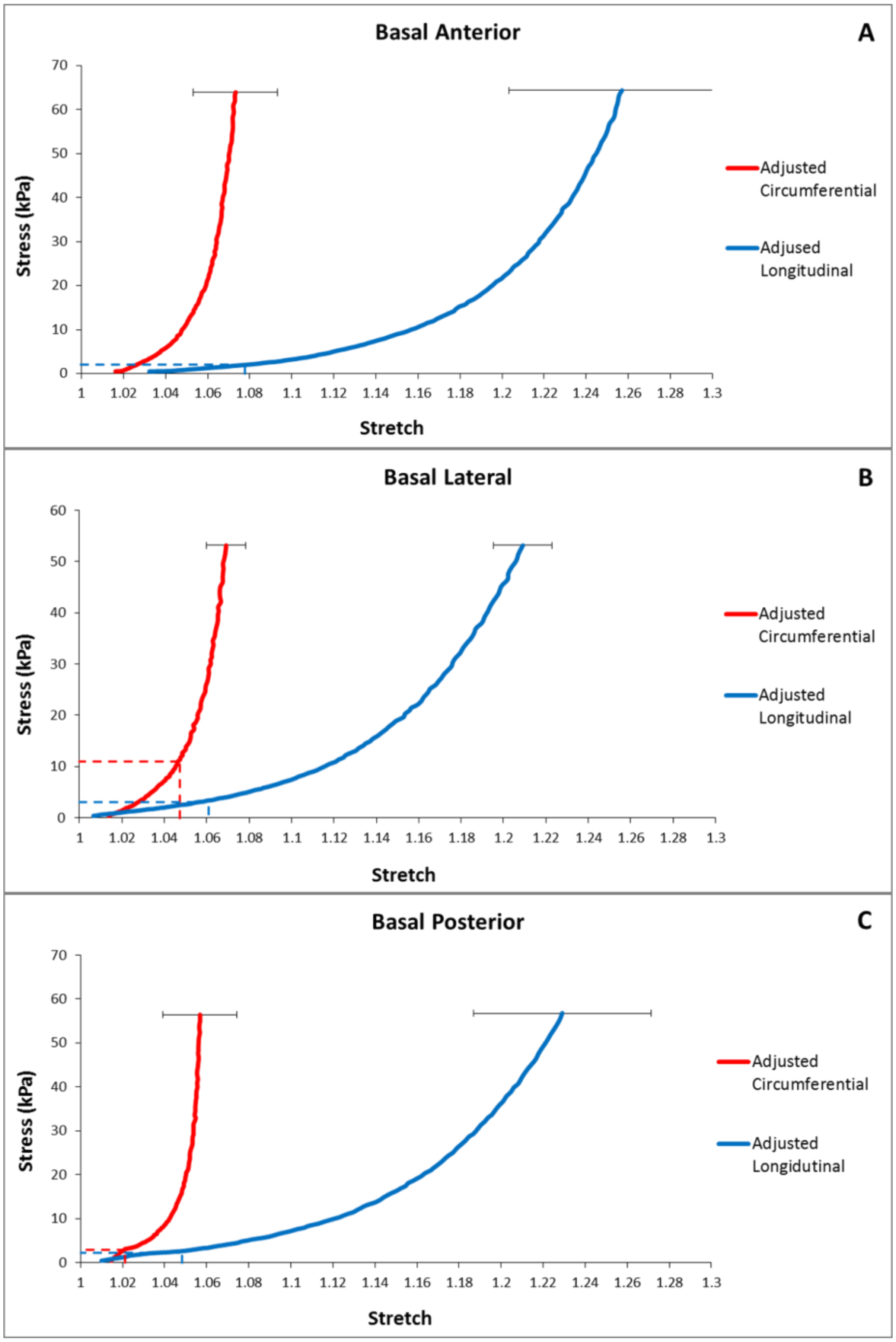

Figure 5.11 Residual stresses of $\sigma_{X(residual)}$ and $\sigma_{Y(residual)}$ predicted by residual strains (ε_X and ε_Y) in the base region.

Note: Three locations in the base region were dissected from the (A) basal anterior; (B) basal lateral; and (C) basal posterior. The red dash lines label the circumferential residual stresses ($\sigma_{X(residual)}$) predicted by the circumferential residual strains (ε_X), and the blue dash lines label the longitudinal residual stresses ($\sigma_{Y(residual)}$) predicted by the longitudinal residual strains (ε_Y). The red curves represent the tension-stretch curves of the CD; the blue curves represent tension-stretch curves of the LD.

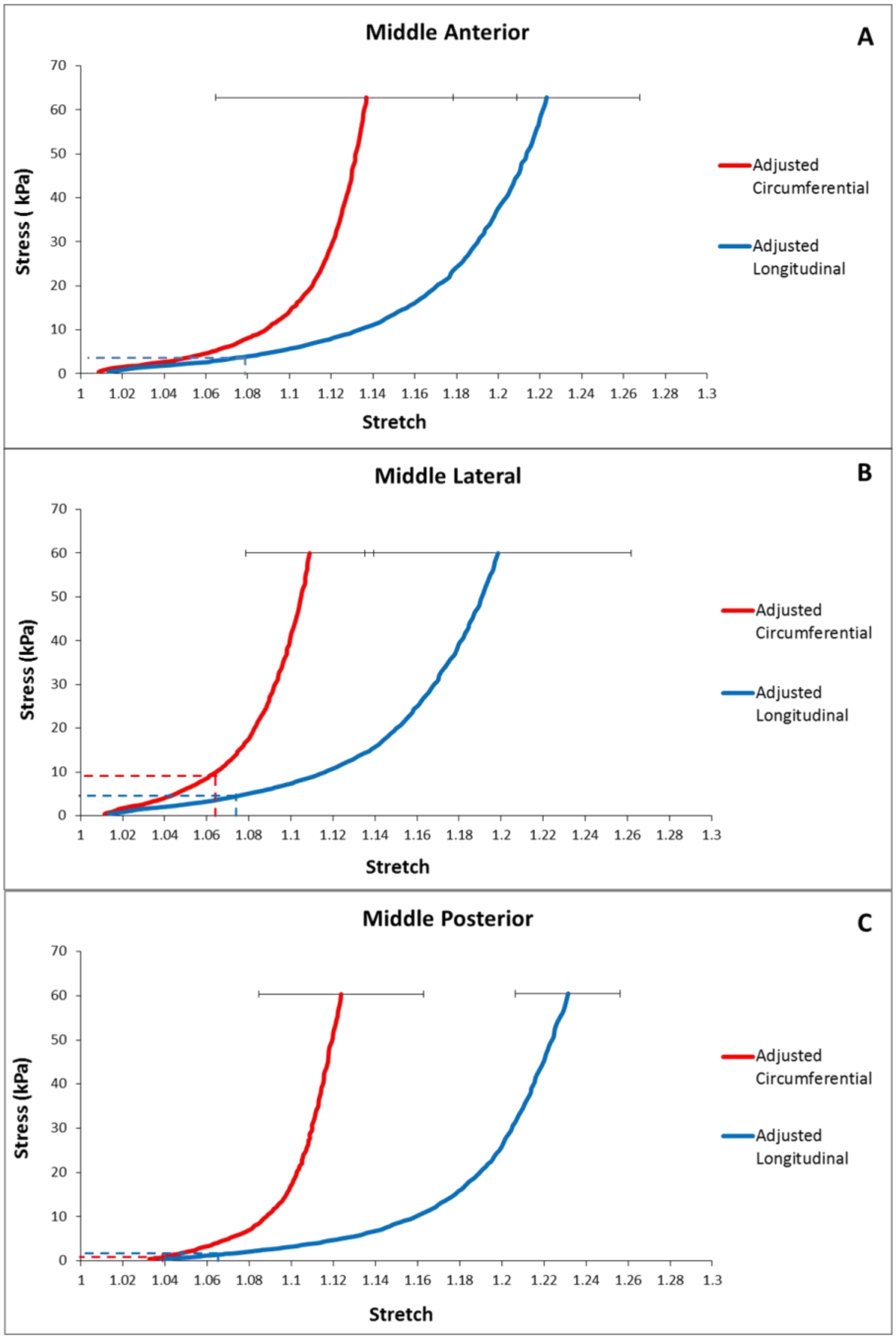

Figure 5.12 Residual stresses of $\sigma_{X(residual)}$ and $\sigma_{Y(residual)}$ predicted by residual strains (ε_X and ε_Y) in the middle region.

Note: Three locations in the middle region were dissected from the (A) middle anterior; (B) middle lateral; and (C) middle posterior. The red dash lines label the circumferential residual stresses ($\sigma_{X(residual)}$) predicted by the circumferential residual strains (ε_X), and the blue dash lines label the longitudinal residual stresses ($\sigma_{Y(residual)}$) predicted by the longitudinal residual strains (ε_Y). The red curves represent the tension-stretch curves of the CD; the blue curves represent tension-stretch curves of the LD.

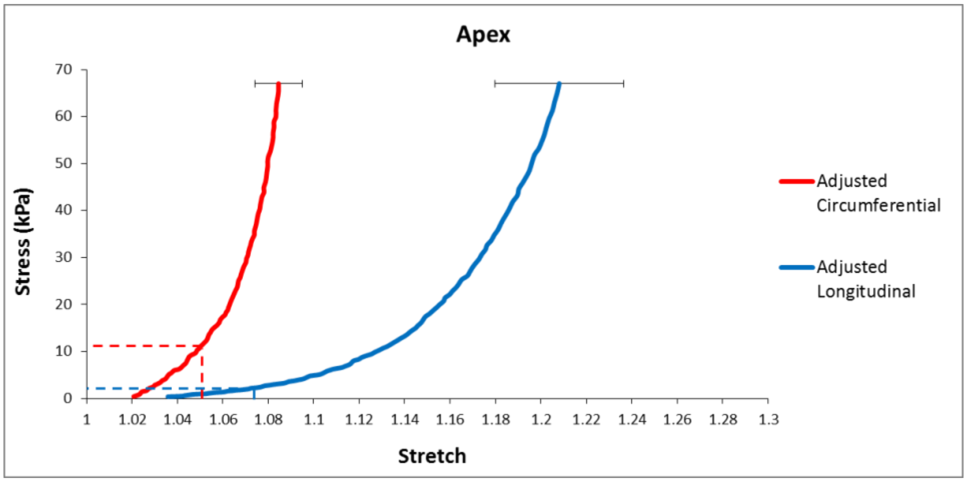

Figure 5.13 Residual stresses of $\sigma_{X(residual)}$ and $\sigma_{Y(residual)}$ predicted by residual strains (ε_X and ε_Y) in the apex region.

Note: The red curve represents the stress-stretch curve of the CD; the blue curve represents the stress-stretch curve of the LD. The red dash line labels the circumferential residual stress ($\sigma_{X(residual)}$) predicted by the longitudinal residual strain (ε_X), and blue dash line labels the longitudinal residual stress ($\sigma_{Y(residual)}$) predicted by the longitudinal residual strain (ε_Y).

Table 5.4 Estimated residual stresses of the epicardial layer on the intact heart.

Residual Stress (kPa)	ε_X	$\sigma_{X(residual)}$	ε_Y	$\sigma_{Y(residual)}$
Basal Anterior (B1)	-0.94%	0	7.76%	1.99
Basal Lateral (B2)	4.70%	11.18	6.02%	3.16
Basal Posterior (B3)	2.01%	2.97	4.94	2.66
Middle Anterior (M1)	-3.90%	0	7.92%	3.88
Middle Lateral (M2)	6.27%	9.54	7.49%	4.46
Middle Posterior (M3)	3.99%	0.96	6.27%	1.27
Apex	5.02%	11.02	7.24%	2.22

Note: The detailed numbers of $\varepsilon_X \rightarrow \sigma_{X(residual)}$ and $\varepsilon_Y \rightarrow \sigma_{Y(residual)}$ for each anatomical location.

The mapping of residual stresses on the left ventricle showed that residual stresses did exist and varied with different anatomical locations. Both the basal anterior location (B1) ($\sigma_{X(residual)} = 0$ kPa, $\sigma_{Y(residual)} = 1.99$ kPa) and middle anterior location (M1) ($\sigma_{X(residual)} = 0$ kPa, $\sigma_{Y(residual)} = 3.88$ kPa) showed very low circumferential residual stresses and longitudinal residual stresses of several kPa. The basal posterior location (B3) ($\sigma_{X(residual)}$ = 2.97 kPa, $\sigma_{Y(residual)}$ = 2.66 kPa) had a relatively larger circumferential residual stress and a longitudinal residual stress of several kPa; middle posterior location (M3) ($\sigma_{X(residual)}$ = 0.96 kPa, $\sigma_{Y(residual)}$ = 1.27 kPa) had both circumferential and longitudinal residual stresses at several kPa range. However, both the basal lateral location (B2) ($\sigma_{X(residual)}$ = 11.18 kPa, $\sigma_{Y(residual)}$ = 3.16 kPa) and middle lateral location (M2) ($\sigma_{X(residual)}$ = 9.54 kPa, $\sigma_{Y(residual)}$ = 4.46 kPa) showed a pattern of very large circumferential residual stresses but longitudinal residual stresses of several kPa. The apex region ($\sigma_{X(residual)}$ = 11.02 kPa, $\sigma_{Y(residual)}$ = 2.22 kPa) showed a very similar pattern to laterals, i.e., a very large circumferential residual stress but longitudinal residual stress of several kPa.

5.4 Discussion

In this chapter, we were able to estimate the regional residual stress of the epicardial layer on the intact left ventricle via a four-step methodology. We first quantified the regional residual strains along both the circumferential and longitudinal directions of the epicardial layer by comparing the *in situ* marker dimensions and dissected marker dimensions under stress-free status. The regional tension-stretch/stress-stretch curves along the CD and LD for all anatomical locations were obtained by biaxial mechanical testing. Due to the software loading control protocol that the biaxial mechanical testing started with the 0.5g tare load applied on the sample, we compared the marker dimensions between the 0.5g tare load status and the 0g load status and estimated the compensatory strains that should be used to adjust the biaxial tension-stretch/stress-stretch curves to start from the real 0g load reference. The residual stresses along the circumferential and longitudinal directions for each anatomical location were thus estimated by the adjusted biaxial stress-stretch curves and the residual strains we obtained already. This is the first time that the residual stress of the epicardial layer on the intact left ventricle was quantitatively estimated, which will help us better understand the overall status of residual stress exerted by the epicardial layer on the left ventricle of the heart.

We found that there are residual stresses in almost all the anatomical locations, i.e., basal anterior (B1), basal lateral (B2), basal posterior (B3), middle anterior (M1), middle lateral (M2), basal posterior (M3), and apex locations (Table 5.4). Moreover, the residual stresses along the circumferential direction ($\sigma_{X(residual)}$) and longitudinal directions ($\sigma_{Y(residual)}$) seem to be location-dependent. For example, both the basal lateral location (B2) and middle lateral location (M2) had relatively large circumferential residual stresses (basal lateral: $\sigma_{X(residual)} = 11.18$ kPa, $\sigma_{Y(residual)} = 3.16$ kPa, middle lateral: $\sigma_{X(residual)} = 9.54$ kPa, $\sigma_{Y(residual)} = 4.46$ kPa). We also noticed that the similar pattern was observed in the apex region ($\sigma_{X(residual)} = 11.02$ kPa, $\sigma_{Y(residual)} = 2.22$ kPa).

Considering the geometry of intact heart, the circumferential direction of the lateral locations, as well as the apex location, often experience very large curvature. The relatively large circumferential residual stresses ($\sigma_{X(residual)}$) of basal lateral location (B2), middle lateral location (M2), and the apex point might have correlation with the sharp circumferential direction wrapping around the epicardial layer at the lateral and apex locations (large curvature of heart surface). We also noticed that the basal anterior location (B1) and middle anterior location (M1) had very low circumferential residual stresses ($\sigma_{X(residual)}$) and residual strains (Table 5.4). We speculate that this might also be related to their anatomical locations, possibly a relatively flat circumferential direction while the longitudinal direction under more tension.

Our quantitative approach provides a much needed knowledge on the epicardial residual stress on the intact heart. The epicardial layer, with its rich elastin content, seems like a balloon wrapping around the heart. The residual stress was also found to be dependent on different anatomical locations of the left ventricle. The residual stress was found to be larger in the locations with larger surface curvature, such as the circumferential direction of the lateral and apex locations. From biomechanical perspective, the residual stress might set up a boundary condition that assists with the contraction of the left ventricle by epicardial recoiling. Our future study will be focusing on the understanding of how the residual stress facilitates cardiac biomechanical functions and how heart diseases could possible alter the residual stress status of the epicardial layer and hence cost the efficiency of ventricle contractions.

CHAPTER VI

SUMMARY, LIMITATIONS, AND FUTURE STUDY

Up to now, the knowledge of the distribution and microstructural arrangement of elastin fibers in the heart tissue remains limited. The detailed contribution of cardiac elastin in cardiac tissue mechanics is still unclear. There is an apparent knowledge gap in 3D cardiac elastin structures and its biomechanical roles in mediating cardiac tissue behavior, which hinders a comprehensive understanding of the delicate 3D structure and performance of cardiac ECM. Hence, we are motivated to fill this knowledge gap with biomedical imaging and bioengineering means.

Cardiac extracellular matrix (ECM) is essential for physiological functioning of a healthy heart by providing structural support to cardiac cells, tethering and enabling force transfer among cardiomyocytes, preventing muscle fiber excessive stretch, transmitting cell signal, etc. Cardiac ECM experiences compositional and structural alterations in heart diseases such as myocardial infarction. Hence there is a growing research need to understand the structural and biomechanical properties of cardiac ECM.

Among the major components in the cardiac ECM, collagen has been the most extensively studied, whereas elastin has received little attention. We hence intended to pursue a thorough investigation to fill the knowledge gap in 3D cardiac elastin structures and its biomechanical roles in mediating cardiac tissue behavior. In this dissertation, four research aims have been successfully carried out, and the major findings and accomplishments are summarized below accordingly.

6.1 Develop an "elastin map" of 3D microstructure of the elastin fiber network on the left ventricle surface in native porcine hearts.

Using decellularization and glycerol treatment, we were able to perform 3D LSCM imaging of the epicardial elastin fiber network in a great depth. We successfully created an overall mapping of 3D microstructure of the epicardial elastin fiber network on the left ventricle of a porcine heart, which included the base, middle, and apex regions. We demonstrated that the 3D elastin fiber network had both location-dependency and depth-dependency. We found that the overall architecture of the epicardial elastin network from the base to the apex was highly correlated with the helical heart muscle fiber orientation revealed by DT-MRI. In different anatomical locations, quantitative analyses clearly showed that the elastin fibers had different alignment and distribution (location-dependency). The comparison between two different depths (the first 15 μm thickness layer and the last 15 μm thickness layer) showed the switch of elastin fiber orientation/alignment, as well as the change of fiber density, demonstrating the depth-dependency of elastin fibers configuration. The depth-dependency of elastin fibers was also verified by the histological observations (Movat's pentachrome staining) of the epicardial elastin. Histology of Movat's pentachrome staining was applied to further investigate the morphology of endocardial elastin fibers and interstitial elastin fibers (myocardial elastin fibers), as well as cardiac elastin fibers associate with the Purkinje fibers.

We did notice that some limitations of the 3D LSCM technique on cardiac elastin study. Due to the low density of interstitial elastin fibers in the myocardium, 3D LSCM had difficulty in detecting the elastin-specific signal. Due to the fine and dense endocardial elastin network, the elastin-specific signal from the endocardium layer was very diffused and blurred, which made the 3D reconstruction of individual elastin fibers infeasible at the current condition.

In the future, we will investigate the cardiac elastin fiber network in the right ventricle of the porcine heart. We will also pursue similar studies on MI hearts to understand the alterations and abnormalities of the 3D elastin fiber network.

6.2 Reconstruct 3D network of the elastin fiber network and examine both the topology and geometry of the network.

Confocal microscopy images are often noisy, generating spurious features, and missing true fibers. We therefore developed a novel 3D confocal image-based analysis algorithm to better render/reconstruct the elastin fiber networks and extract topological fiber metrics. Four computational steps were used. (i) A new fiber segmentation method was developed to generate a mask of “fiberness” value at each pixel, which benefits accurate fiber rendering/reconstruction and further processing. (ii) We also developed a fiber skeletonization method to obtain a one-voxel-thick centerline skeleton by using homotopic thinning algorithm. This fiber skeletonization greatly helps remove spurious fiber branches. (iii) We successfully generated the topological and geometrical descriptors aiming to simplify the elastin fiber network by identifying important nodes with graph metrics. (iv) Based on the reconstructed elastin fiber network, we were also able to obtain the 3D orientation and distribution of the elastin fibers. Our pioneered fiber-based metrics has provided a more specific and more robust biometrics for 3D elastin fiber network analyses, which bring the study of cardiac elastin to a new level, and will have a broader impact to elastin network studies in other types of soft tissues.

In this Aim, we were only able to apply the novel biometrics analyses, i.e., fiber branching, 3D orientation and distribution, number of branching points, and number of cliques, to certain anatomical locations. Our future studies will apply those biometrics analyses to all anatomical locations of the left ventricle. Moreover, further potential metrics include fiber length, average fiber curvature, average scale along fiber in the network will be analyzed in order to provide a full topological and geometrical observation.

6.3 Demonstrate the existence of the regional residual stress of the epicardial elastin in the left ventricle surface via a novel surface curling angle characterization.

Built on our observation of the bi-layered LV surface strip (epicardial layer + attached heart muscle) always curls towards the epicardium side, we successfully developed a semi-quantitative approach to characterize the residual stress in the epicardial layer. The existence of residual stress, i.e., the stress that remains in the tissue after all external loads are removed, always has its physiological relevance for organ/tissue functionality. Our novel curling angle characterization not only provides an intuitive method to reveal the existence of residual stress in the epicardial layer on the intact left ventricle of the heart, but also a semi-quantitative characterization. We defined and measured the curly-enclosed angle ($\theta_{\text{curly-enclosed}}$) of the dissected native strips and the natural angle (θ_{natural}) reflecting the heart surface curvature. From those two angles, we were able to calculate the total angular change due to curling (θ_Δ), which gave us the semi-quantitative information about the degree of residual stress.

We found that the circumferential residual stress was larger in the lateral locations, i.e., (i) the circumferential residual stress in the basal lateral (B2) was larger than the circumferential stresses of the basal anterior location (B1) and basal posterior location (B3); (ii) the circumferential residual stress in the middle lateral location (M2) was larger than the circumferential stresses of the middle anterior location (M1) and middle posterior location (M3); (iii) the circumferential residual stress was large in the apex location. We also found that the longitudinal residual stresses in the anterior locations were larger than the longitudinal stresses of the lateral and posterior locations. Moreover, the longitudinal residual stress in the apex region was comparable to the longitudinal stress of the anterior locations. To compare the circumferential residual stress and longitudinal residual stress at the same anatomical locations, we found that (i) for the basal anterior location (B1) and middle anterior location (M1), the circumferential residual stresses were smaller than the longitudinal residual stresses; (ii) for the apex location, the circumferential residual stress was larger than the longitudinal residual stress.

The limitation of the curling angular measurement is its semi-quantitative nature due to the challenge of dissection. The dissection of heart surface strips using scalpel will inevitably have small variations in dimensions; for example, the sample thickness will very likely affect the degree of curling of the surface strip. Those uncertainties might be diminished to a degree by average, but this limitation still makes the method sensitive to the relatively large difference in residual stress. Moreover, this method cannot give out an accurate number of the residual stress.

Another interesting phenomenon is, among some of the surface strips, the curling often accompanies with a degree of twisting, mostly like due to the pulling of elastin contraction (elastin fiber orientation) is not aligned with the long axis of the rectangular strip. This is a phenomenon that reals the local elastin fiber orientation related to dissected dimension and is worthy further investigation.

6.4 Quantify the regional residual stress in the epicardial layer of the left ventricle.

For the first time, we were able to estimate the regional residual stress of the epicardial layer on the intact left ventricle via a four-step methodology. (i) We first quantified the regional residual strains along both the circumferential and longitudinal directions of the epicardial layer by comparing the *in situ* marker dimensions and dissected marker dimensions under the stress-free status. (ii) We obtained the regional tension-stretch/stress-stretch curves along the CD and LD for all the anatomical locations by biaxial mechanical testing. (iii) We adjusted the biaxial tension-stretch (stress-stretch) curves to the 0g load reference status of the epicardial samples by comparing the marker dimensions between the 0.5g tare load status (biaxial testing routine) and 0g load status to estimate the compensatory strains. (iii) We were finally able to estimate the residual stresses along the circumferential and longitudinal directions for each anatomical location using the adjusted biaxial stress-stretch curves and the residual strains we obtained in step (i).

The results demonstrated that there were residual stresses in the epicardial layer in almost all the anatomical locations of the left ventricle. Furthermore, the circumferential residual stress ($\sigma_{X(residual)}$) and the longitudinal residual stress ($\sigma_{Y(residual)}$) had a location-dependency, and we could give an accurate estimation of the values of $\sigma_{X(residual)}$) and $\sigma_{Y(residual)}$. For instance, (i) both the basal lateral location (B2) and middle lateral location (M2) had relatively large circumferential residual stresses (basal lateral: $\sigma_{X(residual)} = 11.18$ kPa, $\sigma_{Y(residual)} = 3.16$ kPa, middle lateral: $\sigma_{X(residual)} = 9.54$ kPa, $\sigma_{Y(residual)} = 4.46$ kPa); (ii) similar pattern was observed in the apex region ($\sigma_{X(residual)} = 11.02$ kPa, $\sigma_{Y(residual)} = 2.22$ kPa). We know that the circumferential direction of the lateral location and the apex location experiences very large curvature. The relatively large $\sigma_{X(residual)}$ of basal lateral location (B2), middle lateral (M2), and apex point might have correlation with the large curvature of heart surface at those locations. Moreover, the basal anterior location (B1) and middle anterior location (M1) had very low circumferential residual stresses ($\sigma_{X(residual)}$) and residual strains, which are likely related to their anatomical locations, i.e., a relatively flat circumferential location while the longitudinal direction under more tension.

Our quantitative approach is a very solid method to estimate the epicardial residual stress on the intact heart. The epicardial layer, with its rich elastin content, might function as a balloon wrapping around the heart. The residual stress might set up a boundary condition that assists with the contraction of the left ventricle by epicardial recoiling. Our future study includes (i) better understand how the residual stress facilitates cardiac biomechanical functions; (ii) how heart diseases could possible alter the residual stress status of the epicardial layer and hence deteriorate the efficiency of ventricle contractions.

REFERENCES

Arts, T., Veenstra, P. C., & Reneman, R. S. (1982). Epicardial deformation and left ventricular wall mechanisms during ejection in the dog. *American Journal of Physiology-Heart and Circulatory Physiology, 243*(3), H379-H390.

Arulampalam, M. S., Maskell, S., Gordon, N., & Clapp, T. (2002). A tutorial on particle filters for online nonlinear/non-Gaussian Bayesian tracking. *Signal Processing, IEEE Transactions on, 50*(2), 174-188.

Aylward, S. R., & Bullitt, E. (2002). Initialization, noise, singularities, and scale in height ridge traversal for tubular object centerline extraction. *Medical Imaging, IEEE Transactions on, 21*(2), 61-75.

Aylward, S. R., Jomier, J., Weeks, S., & Bullitt, E. (2003). Registration and analysis of vascular images. *International Journal of Computer Vision, 55*(2-3), 123-138.

Baroldi, G. (1965). Acute coronary occlusion as a cause of myocardial infarct and sudden coronary heart death. *Am J Cardiol, 16*(6), 859-880.

Baroldi, G. (1973). Coronary heart disease: significance of the morphologic lesions. *Am Heart J, 85*(1), 1-5.

Baumbach, G., Walmsley, J., & Hart, M. (1988). Composition and mechanics of cerebral arterioles in hypertensive rats. *The American journal of pathology, 133*(3), 464.

Baumbach, G. L., & Hajdu, M. A. (1993). Mechanics and composition of cerebral arterioles in renal and spontaneously hypertensive rats. *Hypertension, 21*(6 Pt 1), 816-826.

Billiar, K. L., & Sacks, M. S. (2000). Biaxial mechanical properties of the native and glutaraldehyde-treated aortic valve cusp: part II—a structural constitutive model. *Journal of biomechanical engineering, 122*(4), 327-335.

Bloksgaard, M., Leurgans, T. M., Nissen, I., Jensen, P. S., Hansen, M. L., Brewer, J. R., . . . Rasmussen, L. M. (2015). Elastin organization in pig and cardiovascular disease patients' pericardial resistance arteries. *Journal of vascular research, 52*(1), 1-11.

Bloomenthal, J. (2002). *Medial-based vertex deformation.* Paper presented at the Proceedings of the 2002 ACM SIGGRAPH/Eurographics symposium on Computer animation.

Borg, T., & Caulfield, J. (1981). *The collagen matrix of the heart.* Paper presented at the Federation proceedings.

Boskamp, T., Rinck, D., Link, F., Kummerlen, B., Stamm, G., & Mildenberger, P. (2004). New vessel analysis tool for morphometric quantification and visualization of vessels in CT and MR imaging data sets 1. *Radiographics, 24*(1), 287-297.

Brennecke, A., & Isenberg, T. (2004). *3D Shape Matching Using Skeleton Graphs.* Paper presented at the SimVis.

Cardiovascular diseases (CVDs). (2015). Retrieved from http://www.who.int/mediacentre/factsheets/fs317/en/

Carver, W., Terracio, L., & Borg, T. K. (1993). Expression and accumulation of interstitial collagen in the neonatal rat heart. *The Anatomical Record, 236*(3), 511-520.

Chadwick, R. (1982). Mechanics of the left ventricle. *Biophysical journal, 39*(3), 279.

Chapman, J. A., & Hulmes, D. J. S. (1984). Electron microscopy of the collagen fibril. In A. Ruggeri & P. M. Motto (Eds.), *Ultrastructure of the Connective Tissue Matrix* (pp. 1-33). Boston: Martinus Nijhoff.

Cheng, X. W., Obata, K., Kuzuya, M., Izawa, H., Nakamura, K., Asai, E., . . . Yokota, M. (2006). Elastolytic cathepsin induction/activation system exists in myocardium and is upregulated in hypertensive heart failure. *Hypertension, 48*(5), 979-987. doi:10.1161/01.HYP.0000242331.99369.2f

Chowdhury, T., & Reardon, W. (1999). Elastin mutation and cardiac disease. *Pediatric cardiology, 20*(2), 103-107.

Cleutjens, J. P., Blankesteijn, W. M., Daemen, M. J., & Smits, J. F. (1999). The infarcted myocardium: simply dead tissue, or a lively target for therapeutic interventions. *Cardiovasc Res, 44*(2), 232-241. doi:S0008-6363(99)00212-6 [pii]

Cleutjens, J. P., Kandala, J. C., Guarda, E., Guntaka, R. V., & Weber, K. T. (1995). Regulation of collagen degradation in the rat myocardium after infarction. *Journal of molecular and cellular cardiology, 27*(6), 1281-1292.

Clifford, P. S., Ella, S. R., Stupica, A. J., Nourian, Z., Li, M., Martinez-Lemus, L. A., . . . Pohl, U. (2011). Spatial Distribution and Mechanical Function of Elastin in Resistance Arteries A Role in Bearing Longitudinal Stress. *Arteriosclerosis, thrombosis, and vascular biology, 31*(12), 2889-2896.

Cornea, N. D., Demirci, M. F., Silver, D., Shokoufandeh, A., Dickinson, S. J., & Kantor, P. B. (2005). *3D object retrieval using many-to-many matching of curve skeletons.* Paper presented at the Shape Modeling and Applications, 2005 International Conference.

Correia, S., Lee, S. Y., Voorn, T., Tate, D. F., Paul, R. H., Zhang, S., . . . Laidlaw, D. H. (2008). Quantitative tractography metrics of white matter integrity in diffusion-tensor MRI. *Neuroimage, 42*(2), 568-581.

D'Amore, A., Stella, J. A., Wagner, W. R., & Sacks, M. S. (2010). Characterization of the complete fiber network topology of planar fibrous tissues and scaffolds. *Biomaterials, 31*(20), 5345-5354.

De Celle, T., Cleutjens, J. P., Blankesteijn, W. M., Debets, J. J., Smits, J. F., & Janssen, B. J. (2004). Long-term structural and functional consequences of cardiac ischaemia-reperfusion injury in vivo in mice. *Exp Physiol, 89*(5), 605-615.

Delingette, H., & Montagnat, J. (2001). Shape and topology constraints on parametric active contours. *Computer Vision and Image Understanding, 83*(2), 140-171.

Deten, A., Volz, H. C., Briest, W., & Zimmer, H.-G. (2002). Cardiac cytokine expression is upregulated in the acute phase after myocardial infarction. Experimental studies in rats. *Cardiovascular research, 55*(2), 329-340.

Dowell, J. D., Field, L. J., & Pasumarthi, K. B. (2003). Cell cycle regulation to repair the infarcted myocardium. *Heart Fail Rev, 8*(3), 293-303. doi:5138701 [pii]

Erhardt, L. R., Unge, G., & Boman, G. (1976). Formation of coronary arterial thrombi in relation to onset of necrosis in acute myocardial infarction in man. A clinical and autoradiographic study. *Am Heart J, 91*(5), 592-598.

Espira, L., & Czubryt, M. P. (2009). Emerging concepts in cardiac matrix biology *Canadian journal of physiology and pharmacology, 87*(12), 996-1008.

Farquharson, C., & Robins, S. P. (1989). The distribution of elastin in developing and adult rat organs using immunocytochemical techniques. *Journal of anatomy, 165*, 225.

Florin, C., Moreau-Gobard, R., & Williams, J. (2004). Automatic heart peripheral vessels segmentation based on a normal MIP ray casting technique *Medical Image Computing and Computer-Assisted Intervention–MICCAI 2004* (pp. 483-490): Springer.

Florin, C., Paragios, N., & Williams, J. (2005). Particle filters, a quasi-monte carlo solution for segmentation of coronaries *Medical Image Computing and Computer-Assisted Intervention–MICCAI 2005* (pp. 246-253): Springer.

Fomovsky, G. M., Thomopoulos, S., & Holmes, J. W. (2010). Contribution of extracellular matrix to the mechanical properties of the heart. *J Mol Cell Cardiol, 48*(3), 490-496.

Frangi, A., Niessen, W., Vincken, K., & Viergever, M. (1998). Medical image computing and computer-assisted intervention. *Berlin, Germany*, 130-137.

Frangi, A. F., Niessen, W. J., Hoogeveen, R. M., Van Walsum, T., & Viergever, M. (1999). Model-based quantitation of 3-D magnetic resonance angiographic images. *Medical Imaging, IEEE Transactions on, 18*(10), 946-956.

Fridman, Y., Pizer, S. M., Aylward, S., & Bullitt, E. (2004). Extracting branching tubular object geometry via cores. *Medical image analysis, 8*(3), 169-176.

Fritsch, D. S., Pizer, S. M., Morse, B. S., Eberly, D. H., & Liu, A. (1994). The multiscale medial axis and its applications in image registration. *Pattern recognition letters, 15*(5), 445-452.

Fung, Y. (1991). What are the residual stresses doing in our blood vessels? *Annals of biomedical engineering, 19*(3), 237-249.

Fung, Y. C. (1993). *Biomechanics: Mechanical Properties of Living Tissues* (2nd ed.). New York: Springer Verlag.

Gaby, A. R. (2010). Nutritional treatments for acute myocardial infarction. *Altern Med Rev, 15*(2), 113-123.

Granzier, H. L., & Irving, T. C. (1995). Passive tension in cardiac muscle: contribution of collagen, titin, microtubules, and intermediate filaments. *Biophysical journal, 68*(3), 1027-1044.

Grauss, R. W., Winter, E. M., van Tuyn, J., Pijnappels, D. A., Steijn, R. V., Hogers, B., . . . Atsma, D. E. (2007). Mesenchymal stem cells from ischemic heart disease patients improve left ventricular function after acute myocardial infarction. *Am J Physiol Heart Circ Physiol, 293*(4), H2438-2447.

Gupta, K. B., Ratcliffe, M. B., Fallert, M. A., Edmunds, L. H., Jr., & Bogen, D. K. (1994). Changes in passive mechanical stiffness of myocardial tissue with aneurysm formation. *Circulation, 89*(5), 2315-2326.

Henderson, B. C., Sen, U., Reynolds, C., Moshal, K. S., Ovechkin, A., Tyagi, N., . . . Tyagi, S. C. (2007). Reversal of systemic hypertension-associated cardiac remodeling in chronic pressure overload myocardium by ciglitazone. *Int J Biol Sci, 3*(6), 385-392.

Hilaga, M., Shinagawa, Y., Kohmura, T., & Kunii, T. L. (2001). *Topology matching for fully automatic similarity estimation of 3D shapes.* Paper presented at the Proceedings of the 28th annual conference on Computer graphics and interactive techniques.

Hodge, A. J., & Petruska, J. A. (1963). *Recent studies with the electron microscope on ordered aggregates of the tropocollagen molecule* (Vol. 289-300). London: Academic Press.

Hoffman, A. H., & Grigg, P. (1984). A method for measuring strains in soft tissue. *Journal of biomechanics, 17*(10), 795-800.

Holmes, J. W., Borg, T. K., & Covell, J. W. (2005). Structure and mechanics of healing myocardial infarcts. *Annu Rev Biomed Eng, 7*, 223-253.

Holmes, J. W., Borg, T. K., & Covell, J. W. (2005). Structure and mechanics of healing myocardial infarcts. *Annu. Rev. Biomed. Eng., 7*, 223-253.

Holmes, J. W., Yamashita, H., Waldman, L. K., & Covell, J. W. (1994). Scar remodeling and transmural deformation after infarction in the pig. *Circulation, 90*(1), 411-420.

Humphrey, J., Strumpf, R., & Yin, F. (1990). Biaxial mechanical behavior of excised ventricular epicardium. *American Journal of Physiology-Heart and Circulatory Physiology, 259*(1), H101-H108.

Humphrey, J., Strumpf, R., & Yin, F. (1992). A constitutive theory for biomembranes: application to epicardial mechanics. *Journal of biomechanical engineering, 114*(4), 461-466.

Irwin, M. W., Mak, S., Mann, D. L., Qu, R., Penninger, J. M., Yan, A., . . . Liu, P. (1999). Tissue expression and immunolocalization of tumor necrosis factor-α in postinfarction dysfunctional myocardium. *Circulation, 99*(11), 1492-1498.

Jöbsis, P. D., Ashikaga, H., Wen, H., Rothstein, E. C., Horvath, K. A., McVeigh, E. R., & Balaban, R. S. (2007). The visceral pericardium: macromolecular structure and contribution to passive mechanical properties of the left ventricle. *American Journal of Physiology-Heart and Circulatory Physiology, 293*(6), H3379-H3387.

Jugdutt, B. I., & Amy, R. W. (1986). Healing after myocardial infarction in the dog: changes in infarct hydroxyproline and topography. *J Am Coll Cardiol, 7*(1), 91-102.

Kang, T., Humphrey, J., & Yin, F. (1996). Comparison of biaxial mechanical properties of excised endocardium and epicardium. *American Journal of Physiology-Heart and Circulatory Physiology, 270*(6), H2169-H2176.

Kang, T., & Yin, F. (1996). The need to account for residual strains and composite nature of heart wall in mechanical analyses. *The American journal of physiology, 271*(3 Pt 2), H947-961.

Kannan, R. Y., Salacinski, H. J., Sales, K., Butler, P., & Seifalian, A. M. (2005). The roles of tissue engineering and vascularisation in the development of micro-vascular networks: a review. *Biomaterials, 26*(14), 1857-1875.

Kitagawa, G., & Gersch, W. (2012). *Smoothness priors analysis of time series* (Vol. 116): Springer Science & Business Media.

Kluge, T., & Hovig, T. (1967). The ultrastructure of human and rat pericardium. *Acta Pathologica Microbiologica Scandinavica, 71*(4), 547-563.

Koller, T. M., Gerig, G., Szekely, G., & Dettwiler, D. (1995). *Multiscale detection of curvilinear structures in 2-D and 3-D image data.* Paper presented at the Computer Vision, 1995. Proceedings., Fifth International Conference on.

Kuk, J. L., Saunders, T. J., Davidson, L. E., & Ross, R. (2009). Age-related changes in total and regional fat distribution. *Ageing research reviews, 8*(4), 339-348.

Layers of the walls of the heart. (2014). Retrieved from https://en.wikiversity.org/wiki/WikiJournal_of_Medicine/Medical_gallery_of_Blausen_Medical_2014

Lee, T.-C., Kashyap, R. L., & Chu, C.-N. (1994). Building skeleton models via 3-D medial surface axis thinning algorithms. *CVGIP: Graphical Models and Image Processing, 56*(6), 462-478.

Li, S. H., Sun, Z., Guo, L., Han, M., Wood, M. F., Ghosh, N., . . . Li, R. K. (2012). Elastin overexpression by cell‐based gene therapy preserves matrix and prevents cardiac dilation. *Journal of cellular and molecular medicine, 16*(10), 2429-2439.

Lindsey, M. L., Yoshioka, J., MacGillivray, C., Muangman, S., Gannon, J., Verghese, A., . . . Lee, R. T. (2003). Effect of a cleavage-resistant collagen mutation on left ventricular remodeling. *Circulation research, 93*(3), 238-245.

Lu, Q., Ganesan, K., Simionescu, D. T., & Vyavahare, N. R. (2004). Novel porous aortic elastin and collagen scaffolds for tissue engineering. *Biomaterials, 25*(22), 5227-5237.

Masutani, Y., Schiemann, T., & Höhne, K.-H. (1998). Vascular shape segmentation and structure extraction using a shape-based region-growing model *Medical Image Computing and Computer-Assisted Interventation—MICCAI'98* (pp. 1242-1249): Springer.

McCulloch, A. D., Smaill, B., & Hunter, P. (1989). Regional left ventricular epicardial deformation in the passive dog heart. *Circulation research, 64*(4), 721-733.

McInerney, T., & Terzopoulos, D. (1996). Deformable models in medical image analysis: a survey. *Medical image analysis, 1*(2), 91-108.

McInerney, T., & Terzopoulos, D. (2000). T-snakes: Topology adaptive snakes. *Medical image analysis, 4*(2), 73-91.

McMahon, J. T., & Ratliff, N. B. (1990). Regeneration of adult human myocardium after acute heart transplant rejection. *J Heart Transplant, 9*(5), 554-567.

Mendez, C., Mueller, W. J., & URGUIAGA, X. (1970). Propagation of impulses across the Purkinje fiber-muscle junctions in the dog heart. *Circulation research, 26*(2), 135-150.

Metz, C., Schaap, M., Van Der Giessen, A., Van Walsum, T., & Niessen, W. (2007). *Semi-automatic coronary artery centerline extraction in computed tomography angiography data.* Paper presented at the Biomedical Imaging: From Nano to Macro, 2007. ISBI 2007. 4th IEEE International Symposium on.

Mewhort, H. E., Turnbull, J. D., Satriano, A., Chow, K., Flewitt, J. A., Andrei, A.-C., . . . Fedak, P. W. (2016). Epicardial infarct repair with bioinductive extracellular matrix promotes vasculogenesis and myocardial recovery. *The Journal of Heart and Lung Transplantation, 35*(5), 661-670.

Mizuno, T., Mickle, D. A., Kiani, C. G., & Li, R.-K. (2005). Overexpression of elastin fragments in infarcted myocardium attenuates scar expansion and heart dysfunction. *American Journal of Physiology-Heart and Circulatory Physiology, 288*(6), H2819-H2827.

Mizuno, T., Yau, T. M., Weisel, R. D., Kiani, C. G., & Li, R.-K. (2005). Elastin stabilizes an infarct and preserves ventricular function. *Circulation, 112*(9 suppl), I-81.

Mujumdar, V. S., & Tyagi, S. C. (1999). Temporal regulation of extracellular matrix components in transition from compensatory hypertrophy to decompensatory heart failure. *J Hypertens, 17*(2), 261-270.

Myocardial Infarction or Heart Attack. (2013). Retrieved from https://commons.wikimedia.org/wiki/File:Blausen_0463_HeartAttack.png

Narula, J., Haider, N., Virmani, R., DiSalvo, T. G., Kolodgie, F. D., Hajjar, R. J., . . . Khaw, B. A. (1996). Apoptosis in myocytes in end-stage heart failure. *N Engl J Med, 335*(16), 1182-1189.

O'connor, W., Davis Jr, J., Geissler, R., Cottrill, C., Noonan, J., & Todd, E. (1985). Supravalvular aortic stenosis. Clinical and pathologic observations in six patients. *Archives of pathology & laboratory medicine, 109*(2), 179-185.

Omens, J. H., & Fung, Y.-C. (1990). Residual strain in rat left ventricle. *Circulation research, 66*(1), 37-45.

Pasumarthi, K. B., & Field, L. J. (2002). Cardiomyocyte cell cycle regulation. *Circ Res, 90*(10), 1044-1054.

Perchet, D., Fetita, C. I., & Preteux, F. J. (2004). *Advanced navigation tools for virtual bronchoscopy.* Paper presented at the Electronic Imaging 2004.

Perou, M. (1961). Congenital supravalvular aortic stenosis. A morphological study with attempt at classification. *Archives of pathology, 71*, 453.

Pizer, S. M., Gerig, G., Joshi, S., & Aylward, S. R. (2003). Multiscale medial shape-based analysis of image objects. *Proceedings of the IEEE, 91*(10), 1670-1679.

Pope, A. J., Sands, G. B., Smaill, B. H., & LeGrice, I. J. (2008). Three-dimensional transmural organization of perimysial collagen in the heart. *American Journal of Physiology-Heart and Circulatory Physiology, 295*(3), H1243-H1252.

Raab, W. (1963). The Nonvascular Metabolic Myocardial Vulnerability Factor in "Coronary Heart Disease". Fundamentals of Pathogenesis, Treatment, and Prevention. *Am Heart J, 66*, 685-706.

Raya, T. E., Gay, R. G., Lancaster, L., Aguirre, M., Moffett, C., & Goldman, S. (1988). Serial changes in left ventricular relaxation and chamber stiffness after large myocardial infarction in rats. *Circulation, 77*(6), 1424-1431.

Reichenbach, D. D., & Moss, N. S. (1975). Myocardial cell necrosis and sudden death in humans. *Circulation, 52*(6 Suppl), III60-62.

Rentschler, S., Vaidya, D. M., Tamaddon, H., Degenhardt, K., Sassoon, D., Morley, G. E., . . . Fishman, G. I. (2001). Visualization and functional characterization of the developing murine cardiac conduction system. *Development, 128*(10), 1785-1792.

Robin, E. D. (1977). Special report: dysoxia. Abnormal tissue oxygen utilization. *Arch Intern Med, 137*(7), 905-910.

Robinson, T. F., Cohen-Gould, L., & Factor, S. M. (1983). Skeletal framework of mammalian heart muscle. Arrangement of inter-and pericellular connective tissue structures. *Laboratory investigation; a journal of technical methods and pathology, 49*(4), 482-498.

Ronse, N. P. C., Baruthio, J., Armspach, J., & Maillot, C. (2006). Magnetic resonance angiography: From anatomical knowledge modelling to vessel segmentation. *Laboratoire des Sciences de Image, de Informatique et of détection (LSIIT), UMR, 7005*.

Sanguinetti, M. C., & Kass, R. S. (1984). Voltage-dependent block of calcium channel current in the calf cardiac Purkinje fiber by dihydropyridine calcium channel antagonists. *Circulation research, 55*(3), 336-348.

Sato, S., Ashraf, M., Millard, R. W., Fujiwara, H., & Schwartz, A. (1983). Connective tissue changes in early ischemia of porcine myocardium: an ultrastructural study. *J Mol Cell Cardiol, 15*(4), 261-275.

Schönherr, E., & Hausser, H.-J. (2000). Extracellular matrix and cytokines: a functional unit. *Journal of Immunology Research, 7*(2-4), 89-101.

Scott, J. E. (1991). Proteoglycan: collagen interactions in connective tissues. Ultrastructural, biochemical, functional and evolutionary aspects. *International Journal of Biological Macromolecules, 13*(3), 157-161.

Sharma, R., & Raghubir, R. (2007). Stem cell therapy: a hope for dying hearts. *Stem Cells Dev, 16*(4), 517-536. doi:10.1089/scd.2006.0070

Sherman, V. R., Yang, W., & Meyers, M. A. (2015). The materials science of collagen. *Journal of the mechanical behavior of biomedical materials, 52*, 22-50.

Shikata, H., Hoffman, E. A., & Sonka, M. (2004). *Automated segmentation of pulmonary vascular tree from 3D CT images.* Paper presented at the Medical Imaging 2004.

Shoulders, M. D., & Raines, R. T. (2009). Collagen structure and stability. *Annual review of biochemistry, 78*, 929.

Silver, F. H., Freeman, J. W., & Seehra, G. P. (2003). Collagen self-assembly and the development of tendon mechanical properties. *J Biomech, 36*(10), 1529-1553.

Silver, M. D., Anderson, T. W., Vand Dreumel, A. A., & Hutson, R. E. (1973). Letter: Nutritional muscular dystrophy and human myocardial infarction. *Lancet, 2*(7834), 912-913.

Smith, A., Doucet, A., de Freitas, N., & Gordon, N. (2013). *Sequential Monte Carlo methods in practice*: Springer Science & Business Media.

Strauer, B. E., & Kornowski, R. (2003). Stem cell therapy in perspective. *Circulation, 107*(7), 929-934.

Sundar, H., Silver, D., Gagvani, N., & Dickinson, S. (2003). *Skeleton based shape matching and retrieval.* Paper presented at the Shape Modeling International, 2003.

Sussman, M. A., McCulloch, A., & Borg, T. K. (2002). Dance band on the titanic biomechanical signaling in cardiac hypertrophy. *Circ Res, 91*(10), 888-898.

Sutton, M. G. S. J., & Sharpe, N. (2000). Left ventricular remodeling after myocardial infarction pathophysiology and therapy. *Circulation, 101*(25), 2981-2988.

Tek, H., Comaniciu, D., & Williams, J. P. (2001). *Vessel detection by mean shift based ray propagation.* Paper presented at the Mathematical Methods in Biomedical Image Analysis, 2001. MMBIA 2001. IEEE Workshop on.

Theocharis, A. D., Skandalis, S. S., Gialeli, C., & Karamanos, N. K. (2016). Extracellular matrix structure. *Advanced drug delivery reviews, 97*, 4-27.

Toledo, R., Orriols, X., Radeva, P., Binefa, X., Vitria, J., Canero, C., & Villanuev, J. (2000). *Eigensnakes for vessel segmentation in angiography.* Paper presented at the Pattern Recognition, 2000. Proceedings. 15th International Conference on.

Type I Collagen Molecular Structure. (2016). Retrieved from http://www.harbormedtech.com/bridge

Vassalle, M. (1970). Electrogenic suppression of automaticity in sheep and dog Purkinje fibers. *Circulation research, 27*(3), 361-377.

Venugopal, J. R., Prabhakaran, M. P., Mukherjee, S., Ravichandran, R., Dan, K., & Ramakrishna, S. (2012). Biomaterial strategies for alleviation of myocardial infarction. *Journal of the Royal Society Interface, 9*(66), 1-19. doi:10.1098/rsif.2011.0301

Vesely, I. (1997). The role of elastin in aortic valve mechanics. *Journal of biomechanics, 31*(2), 115-123.

Vrolijk, B., Reinders, F., & Post, F. H. (2003). *Feature tracking with skeleton graphs.* Paper presented at the Data Visualization.

Wan, M., Dachille, F., & Kaufman, A. (2001). *Distance-field based skeletons for virtual navigation.* Paper presented at the Proceedings of the conference on Visualization'01.

Wang, B., Borazjani, A., Tahai, M., Curry, A. L., Simionescu, D. T., Guan, J., . . . Liao, J. (2010). Fabrication of cardiac patch with decellularized porcine myocardial scaffold and bone marrow mononuclear cells. *J Biomed Mater Res A, 94*(4), 1100-1110. doi:10.1002/jbm.a.32781

Wang, B., Tedder, M. E., Perez, C. E., Wang, G., de Jongh Curry, A. L., To, F., . . . Liao, J. (2012). Structural and biomechanical characterizations of porcine myocardial extracellular matrix. *J Mater Sci Mater Med, 23*(8), 1835-1847. doi:10.1007/s10856-012-4660-0

Wang, B., Wang, G., To, F., Butler, J. R., Claude, A., McLaughlin, R. M., . . . Liao, J. (2013). Myocardial scaffold-based cardiac tissue engineering: application of coordinated mechanical and electrical stimulations. *Langmuir, 29*(35), 11109-11117. doi:10.1021/la401702w

Weber, I. T., Harrison, R. W., & Iozzo, R. V. (1996). Model structure of decorin and implications for collagen fibrillogenesis. *J Biol Chem, 271*(50), 31767-31770.

Williams, C., & Black III, L. D. (2015). The Role of Extracellular Matrix in Cardiac Development *Biomaterials for Cardiac Regeneration* (pp. 1-35): Springer.

Witkin, A. P. (1984). *Scale-space filtering: A new approach to multi-scale description.* Paper presented at the Acoustics, Speech, and Signal Processing, IEEE International Conference on ICASSP'84.

Yi, J., & Ra, J. B. (2003). A locally adaptive region growing algorithm for vascular segmentation. *International Journal of Imaging Systems and Technology, 13*(4), 208-214.

Zhang, S., Crow, J. A., Yang, X., Chen, J., Borazjani, A., Mullins, K. B., . . . Liao, J. (2010). The correlation of 3D DT-MRI fiber disruption with structural and mechanical degeneration in porcine myocardium. *Annals of biomedical engineering, 38*(10), 3084-3095.

Ziegel, E. R. (1997). Bayesian Forecasting and Dynamic Models. *Technometrics, 39*(4), 433.

Zile, M. R., & Brutsaert, D. L. (2002). New concepts in diastolic dysfunction and diastolic heart failure: Part I Diagnosis, prognosis, and measurements of diastolic function. *Circulation, 105*(11), 1387-1393.

Zipfel, W. R., Williams, R. M., Christie, R., Nikitin, A. Y., Hyman, B. T., & Webb, W. W. (2003). Live tissue intrinsic emission microscopy using multiphoton-excited native fluorescence and second harmonic generation. *Proceedings of the National Academy of Sciences, 100*(12), 7075-7080.